Electronic and structural properties at the interfaces between graphene and molecular acceptors/donors

D i s s e r t a t i o n
zur Erlangung des akademischen Grades
d o c t o r r e r u m n a t u r a l i u m
(Dr. rer. nat.)
im Fach Physik
eingereicht an der

Mathematisch-Naturwissenschaftlichen Fakultät
der Humboldt-Universität zu Berlin
von

M.Sci. Christodoulos Christodoulou

Präsident der Humboldt-Universität zu Berlin
Prof. Dr. Jan-Hendrik Olbertz

Dekan der Mathematisch-Naturwissenschaftlichen Fakultät
Prof. Dr. Elmar Kulke

Gutachter: 1. PD Dr. Benedetta Casu
               2. Prof. Dr. Luca Pasquali
               3. Prof. Dr. Norbert Koch

Tag der mündlichen Prüfung: 25.09.15

Abstract

Work function tuning at organic/electrode interfaces is of principal importance for the efficient operation of organic electronic devices, as it allows for the minimisation of charge injection barriers formed at such interfaces. In this thesis, the work function of graphene, a promising electrode for (opto)electronic devices was modified by adsorption of air-stable conjugated organic molecules (COMs) that act as strong molecular acceptors or donors. The valence and core level properties, together with the work function modification of the vacuum-deposited COMs on graphene were investigated with photoelectron spectroscopy (PES), while the orientation of COMs was studied with near edge X-ray fine structure spectroscopy (NEXAFS). The work function of graphene-on-quartz (G/Qu) is modified up to $5.7\,\mathrm{eV}$ and down to $3\,\mathrm{eV}$ as a result of charge transfer (CT) occurring right at the interface, which does not invoke covalent bond formation between the molecular monolayer and the graphene. In addition to the CT, in the case of the molecular acceptor hexaazatriphenylene-hexacarbonitrile (HATCN), the work function increase proceeded via a density-dependent re-orientation of the molecule in the monolayer regime. For all the other tested molecular acceptors (donors) deposited on graphene-on-quartz, the CT was observed to induce positive (negative) surface CT doping of the graphene layer, leading to a work function increase (decrease) and was disentangled into two contributions: (a) shift of the Vacuum level due to the formation of an interface dipole at the COM/graphene interface and (b) shift of the Fermi level of the graphene due to the surface CT doping. Additionally, the molecular acceptor hexafluoro-tetracyanonapththoquinodimethane (F_6TCNNQ) was deposited on both G/Qu and graphene-on-copper, where the CT was found to originate from graphene and copper support respectively. The findings were supported by density functional theory calculations and significantly add to a fundamental understanding of graphene/COM interfaces.

Keywords: organic/graphene interfaces, work function, photoelectron spectroscopy, molecular orientation

Zussamenfassung

Die Austrittsarbeitsanpassung an Organik/Elektrode-Grenzflächen ist von entscheidener Bedeutung für den effizienten Betrieb von Bauteilen der organischer Elektronik, da diese die Minimierung von Ladungsträger- injektionsbarrieren an solchen Grenzflächen ermöglicht. In dieser Arbeit wurde die Austrittsarbeit von Graphen, einer vielversprechenden Elektrodenmaterial für (opto)- elektronische Bauteile, durch die Adsorption von luftbeständigen konjugierten organischen Molekülen (KOMs), welche als Akzeptoren und Donatoren fungieren, modifiziert. Die Eigenschaften der Valenz- und Rumpfniveaus sowie die Austrittsarbeitsmodifikation der vakuumverdampften KOMs wurden mit Photoelektronenspektroskopie (PES) untersucht, während die Orientierung der KOMs mit Röntgen-Nahkanten-Absorptions-Spektroskopie (NEXAFS) aufgeklärt wurde. Die Austrittsarbeit von Graphene auf Quartz (G/Qu) lässt sich auf maximal 5.7 eV und minimal 3 eV anpassen, welches aus einem Ladungstransfer direkt an der Grenzfläche resultiert, der keine Ausbildung von kovalenten Bindungen zwischen der molekularen Monolage und dem Graphen beinhaltet. Zudem, für den starken molekularen Akzeptor Hexaazatriphenylen-Hexacarbonitril (HATCN) verläuft die Austrittsarbeitserhöhung über eine Orientierungsänderung der Moleküle im Monolagenbereich. Für alle anderen auf G/Qu abgeschiedenen Akzeptoren (Donatoren) wurde beobachtet, dass der Ladungstransfer eine positive (negative) Oberflächen- ladungsdotierung der Graphen-Schicht bewirkt, welches in einer Austrittsarbeitserhöhung (-erniedrigung) resultiert. Letztere ließ sich jeweils in zwei Beiträge zerlegen: (a) Verschiebung des Vakuumniveaus durch einen Grenzflächendipol an der KOM/Graphen-Grenzflche und (b) Verschiebung des Fermi-Niveaus durch Oberflächenladungstransferdotierung der Graphen-Schicht. Weiterhin wurde der molekulare Akzeptor Hexafluoro-tetracyano napththoquinodimethan (F_6TCNNQ) sowohl auf G/Qu als auch auf Graphen auf Kupfer abgeschieden, wobei sich herausstellte, dass der Ladungstransfer im ersteren Fall vom Graphen stammt, und im letzteren von der Kupferunterlage. Die Ergebnisse werden von Dichtefunktionaltheorieberechnungen gestützt und tragen erheblich zum Verständnis von Graphen/KOM-Grenzflächen bei.

Schlagworte: Organik/Graphen-Grenzfläche, Austrittsarbeit, Photoelektronenspektroskopie, Molekülorientierung

Contents

1 Introduction

A full decade has passed since the isolation of the first single layer graphene sheet [1–4]. Since then, several multidisciplinary research groups have made a lot of effort in order to study graphene with all possible experimental and theoretical methods. This comes to no surprise, since the discovery of graphene's two-dimensional atomically thick carbon atom network, arranged in a honeycomb lattice, manifests remarkable electronic, mechanical, optical and thermal properties. A small sample of the extraordinary properties of graphene include: ambipolar field effect [2], superior mechanical strength [5], high transparency [6, 7] and high thermal conductivity [8]. Graphene has already been used in a plethora of (opto)electronic devices, e.g., organic light emitting diodes (OLEDs) [9], sensors [10], batteries [11], solar cells [12], touchscreens [13]. Thus, this material opened pathways not only for studying fundamental new physics, but it also paved the way towards a new marketplace. One of the most promising uses of graphene is as transparent, highly conducting electrode. This is an essential part of (opto)electronic devices since they are used as one of the end points of the devices, that are responsible for extracting or injecting charges. Up to now, the "market standard" for (opto)electronic devices has been indium tin oxide (ITO), because of its high transparency, low sheet resistance, and favourable work function (Φ) [14, 15]. Its use over the past years, however, has been increasingly problematic for several reasons: it requires a complicated processing, it has a high surface area roughness and it is brittle, all of these limiting its incorporation into flexible devices. Furthermore, the element indium which makes up typically 90% of the ITO per weight is increasing in cost because of its low abundance.

This is the main motivation for the current work. A lot of effort has been put into finding suitable replacements for ITO as a transparent electrode. Different materials came up, such as conductive polymers, e,g, poly(3,4-ethylenedioxythipohene):poly(styrenesulfonate - PEDOT:PSS)[16] and carbon nanotubes (CNTs) [17]. These materials exhibit limitations,

such as thermal degradation in the case of PEDOT:PSS [18] and high resistance between CNTs [19] that prevented them to be competitive enough as a realistic replacement in transparent and flexible (opto)electronic devices.

Thus, the search for new kinds of materials lead to the investigation of graphene as conducting and transparent electrode. The boost in graphene research, and especially methods for producing large graphene sheets, enabled graphene to become a promising candidate for a technologically viable transparent electrode. This was promoted by chemical vapor deposition (CVD) synthesis of graphene, that has been proven to provide technologically relevant graphene sheets that are highly crystalline [13, 20] and can be easily transferred to any substrate of interest [21].

However, graphene has only limited value as a standalone material. It needs to be functionalised with other nanomaterials or molecules in order to tune its energy levels, such as the work function in order to match the energy levels of commonly used organic semiconductors (OSCs) in, e.g., organic photovoltaic cells (OPVCs) or OLEDs and thus reducing the energy barriers formed at the interfaces.

One very efficient way to tailor the work function of electrodes and consequently improve the device performance by achieving low-energy charge injection barriers is to use an interlayer of COMs with the property of accepting or donating electrons [22].

The graphene/COM systems presented in this work were mainly studied by means of ultraviolet - and X- ray photoelectron spectroscopies (UPS and XPS, respectively) for electronic characterisation and near edge X-ray absorption fine structure spectroscopy (NEXAFS) in order to gain insight into the orientation of the COM when adsorbed on graphene.

Furthermore, most of the experiments were done in combination with theoretical modelling using density functional theory (DFT) to gain insight into the relevant processes and in turn to explain the experimental findings. The theoretical work was done by the group of Dr. David Beljonne and Prof. Luca Pasquali.

This thesis is outlined as follows: Chapter 2 gives an introduction into graphene and organic solid state physics. Chapter 3 describes the principles of experimental methods used and Chapter 4 presents the materials used, the experimental setups, together with details about the data analysis performed.

Chapter 5 is the main part of this work. Here, the experimental results are presented, in parallel to a discussion concerning the theoretical results performed by our collaborators.

Sec. 5.1 discusses the preparation and characterisation of graphene-on-quartz (G/Qu) before and after annealing in ultrahigh vacuum (UHV).

Sec. 5.2 discusses the functionalisation of graphene-on-quartz by pre-covering it with the acceptor molecule hexaazatriphenylene-hexacarbonitrile (HATCN). In this study, a work function increase of G/Qu up to 1.2 eV was observed and was attributed to a charge transfer (CT) invoking the substrate and the first monolayer of the molecular acceptor. Additionally, NEXAFS was performed in order to explain the sub-linear Φ increase observed, as evidenced by the molecular density dependent re-orientation of the COM within the first monolayer. HATCN was also deposited on graphene-on-copper (G/Cu), showing similar results.

Graphene was also functionalised using the molecular acceptor hexafluoro-tetracyanonapththoquinodimethane (F_6TCNNQ) and the results are presented in Sec. 5.3. F_6TCNNQ was also deposited on both G/Qu and G/Cu in order to investigate variations arising from the different graphene support. An abrupt work function increase of 1 eV (G/Qu) and 1.3 eV (G/Cu) was observed both experimentally and theoretically. It was found that the CT occurs between graphene and COM in the case of G/Qu, whereas, in the case of G/Cu the CT invokes the deposited COM and the copper support. The work function change could be disentangled into two contributions: shift of the Fermi level (E_F) of graphene with respect to the Dirac point due to surface CT doping and interface dipole (ID) formation shifting the vacuum level (E_{vac}). Using XPS, the CT was verified by examining the N 1s emissions. NEXAFS was performed for the G/Qu pre-covered with F_6TCNNQ, showing that the molecule is flat lying regardless the molecular density in the monolayer.

Finally in Sec. 5.4, the functionalisation of G/Qu with two novel dimer molecular donors was studied. In this case, a substantial work function decrease of 1.4 eV was observed for pentamethyl-rhodocene ([RhCp*Cp]$_2$) and 1.2 eV for pentamethyl-cyclopentadienyl-trialkylbenzene-ruthenium ([RuCp*mes]$_2$). This work function decrease was explained via CT between the molecular donors and graphene, after the dimers in contact with graphene were turned into monomeric cations, donating one electron from

the metal core to graphene, thus n-doping the graphene layer.

The results are summarised in Chapter 6, while an outlook is proposed based on the experimental and theoretical knowledge obtained in this work.

This study comes in a very appropriate time in the graphene research. It offers viable ways to dope the graphene layer and tune its work function in a non-destructive and non-covalent manner so that the perturbation caused to the desired electronic properties of graphene is kept to the minimum. Furthermore, it presents a novel air stable organic molecule together with a technologically relevant substrate (CVD graphene-on-quartz), that could be used in the technological sector to scale up the process of manipulating the electronic properties of graphene using molecular functionalisation.

2 Fundamentals

In this chapter, the motivation for performing the work in this thesis is explicated by highlighting the background regarding the electronic structure, the production and the functionalisation of graphene. Furthermore, a brief description of COMs and their affinity with organic electronic devices is given together with a summary of energetics at interfaces of electrodes, work function tuning and growth modes of thin films.

2.1 Graphene

In this section, some of the electronic properties of graphene that make this material particular are outlined. In addition, a small review of the methods of graphene synthesis is provided. Finally, methods for functionalising graphene covalently and non-covalently are presented.

2.1.1 Electronic structure

The electronic band structure of a material allows for describing its physical properties, e.g., electrical resistivity and optical absorption. Furthermore, it is crucial for understanding the operation principles of related solid-state devices, such as transistors, light emitting diodes and solar cells.

The hybridisation of the two dimensional network of carbon atoms in graphene is key in its resulting electronic properties. A single carbon atom contains a total of six electrons and exhibits the electronic configuration $1s^2$, $2s^2$, $2p^2$. The electrons in the 1s orbitals are the core-level electrons that are not involved in bond formation, while the ones in the 2s and 2p orbitals are the valence electrons and are involved in bond formation. These valence electrons can hybridise (share electrons) in three ways, such that the carbon atom can have two, three or four adjacent atoms available for bond formation, with the electrons forming the hybrid orbitals sp, sp^2 and sp^3, respectively.
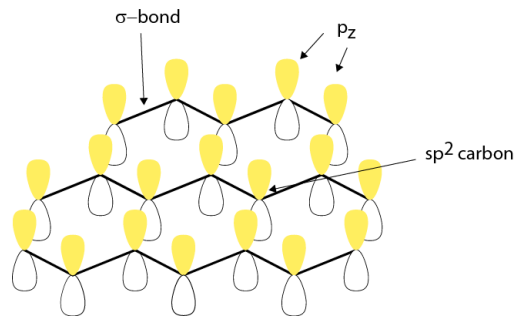
Figure 2.1: Schematic illustration showing the p_z orbitals perpendicular to the plane of graphene and the σ bonds between neighbouring sp^2 carbon atoms. Figure adapted from [23].

The carbon atoms in graphene are sp^2 hybridised, i.e., they have three in-plane neighbours that each form a σ bond, as shown in Fig. 2.1. These bonds are of covalent character and the resulting crystal structure is planar hexagonal, as shown in Fig. 2.2a. The formation of the σ bonds leaves out one 2p orbital ($2p_z$) perpendicular to the graphene plane, which does not participate in the bond formation. The adjacent $2p_z$ orbitals weakly interact to form the π band of graphene that contains the delocalised valence electrons. As it follows from theoretical calculations, the electrons in this band mimic relativistic particles, behaving as massless Dirac fermions and are responsible for the excellent conductivity of graphene [2].
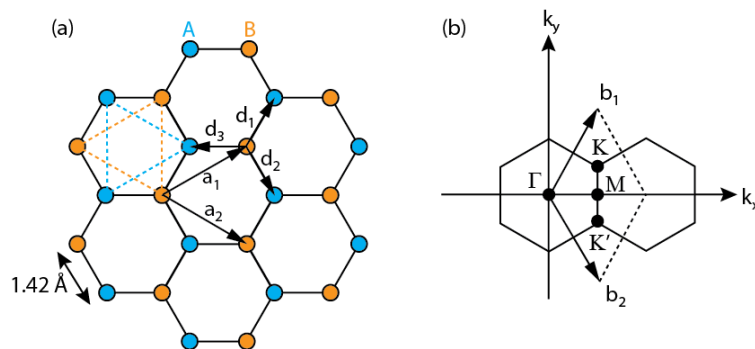
Figure 2.2: (a) The hexagonal honeycomb lattice of graphene in real space, formed by the carbon atoms in the two sublattices A and B, with the blue atom in sublattice A and orange atom in sublattice B. d_i represent the nearest neighbour carbon atoms, with the distance being 1.42 Å. The unit cell is formed by the lattice vectors a_1 and a_2. (b) Reciprocal lattice of graphene with the two reciprocal lattice vectors b_i. Γ, K, M are high symmetry points. Figure adapted from [24].

The nearest distance between carbon atoms in graphene is 1.42 Å, with the lattice vectors, as shown in Fig. 2.2a:

$$a_1 = \frac{a}{2}\left(3, \sqrt{3}\right), a_2 = \frac{a}{2}\left(3, -\sqrt{3}\right) . \tag{2.1}$$

The lattice parameter is given by $a=|a_1|=|a_2|=1.42\sqrt{3}$ Å = 2.46 Å and the lattice vectors in reciprocal space are then given by:

$$b_1 = \frac{2\pi}{3a}\left(1, \sqrt{3}\right), b_2 = \frac{2\pi}{3a}\left(1, -\sqrt{3}\right) . \tag{2.2}$$

The points K and K', or Dirac points, in Fig. 2.2b, that are located at the corners of the Brillouin zone are very important for the specific physical properties arising in graphene. They are at the positions:

$$K = \left(\frac{2\pi}{3a}, \frac{2\pi}{3\sqrt{3}a}\right), K' = \left(\frac{2\pi}{3a}, \frac{2\pi}{-3\sqrt{3}a}\right) . \tag{2.3}$$

The three nearest-neighbour vectors in real space are:

$$d_1 = \frac{a}{2}\left(1, \sqrt{3}\right), d_2 = \frac{a}{2}\left(1, -\sqrt{3}\right), d_3 = -a\left(1, 0\right) . \tag{2.4}$$

The tight binding Hamiltonian for electrons in graphene, wherein only electrons that can hop to nearest-neighbour and next-nearest-neighbour atoms are taken into account [24, 25], yields the following energy dispersion relation as a function of the wavevector k:

$$E_\pm\left(k\right) = \pm\hbar t\sqrt{3 + f\left(k\right)} - \hbar t' f\left(k\right) , \tag{2.5}$$

with:

$$f\left(k\right) = 2\cos\left(\sqrt{3}k_y a\right) + 4\cos\left(\frac{\sqrt{3}}{2}k_y a\right)\cos\left(\frac{3}{2}k_x a\right) . \tag{2.6}$$

The positive and negative signs describe the π and π^* bands that correspond to the dispersion of the bonding and anti-bonding molecular orbitals, constructed from the p_z atomic orbitals on the carbon atoms. The value t is the nearest-neighbour hopping energy (i.e., hopping between carbon atoms at different sublattices) and t' is the next-nearest hoping energy [24]. When the value of t' is 0, then electron-hole symmetry exists and the π and π^* bands become symmetric.

Close to the Dirac points, the energy dispersion is obtained by expanding eq. (2.5). Using $\mathbf{k} = \mathbf{K}+\mathbf{q}$, with $\mathbf{q}$ the momentum measured relative to the Dirac points and $|q| \ll |K|$:

$$E_\pm(\mathbf{q}) = \pm\, \hbar\, u_F |\mathbf{q}|\,, \tag{2.7}$$

when considering only the first term in the expansion.

The term u_F represents the Fermi velocity that is determined theoretically by $u_F = 3ta/2$ [24]. Taking the nearest hopping energy t as ≈ 2.8 eV, as found by calculations, then the Fermi velocity becomes $u_\mathrm{F} \approx 10^6 \mathrm{ms}^{-1}$ [25].

This result for the energy dispersion in eq. 2.7 is very different to the usual case as in e.g., inorganic semiconductors, where $E(\boldsymbol{q}) = q^2/(2m)$ with m being the electron mass. The discrepancy lies in the fact that u_F does not depend on the energy or the momentum as in the usual case where u = k/m = $\sqrt{2E/m}$ and the velocity changes significantly with energy. The energy dispersion as given in eq. (2.7) imitates the one that ultrarelativistic particles follow, which is described by the Dirac equation that is also used to describe the energy dispersion of photons [24].

The density of states close to the Dirac point per unit cell ($\rho(E)$) is given by [24]:

$$\rho(E) = \frac{2|E|}{\pi\, \hbar^2\, u_F^2}\,. \tag{2.8}$$

In Fig. 2.3a the resulting band structure of graphene is plotted in 3D for the first Brillouin zone. The occupied π and unoccupied π^* bands intersect at the K and K′ points, which are the corners of the unit cell of graphene in reciprocal space and the energy dispersion close to these points is linear, as shown in the zoom close to the K point, in Fig. 2.3b.

In summary, the linear energy dispersion of π and π^* bands near the Dirac points make the electrons in graphene behave as ultrarelativistic particles travelling with u_F through the graphene sheet and the transport in graphene is mainly by hopping of electrons from one sublattice to the other [26]. The vanishing density of states near the K points leads to mobility of charge carriers surpassing the mobilities observed in silicon [1, 2] and graphene exhibits ballistic charge carrier transport with a high mean free path [2, 27].
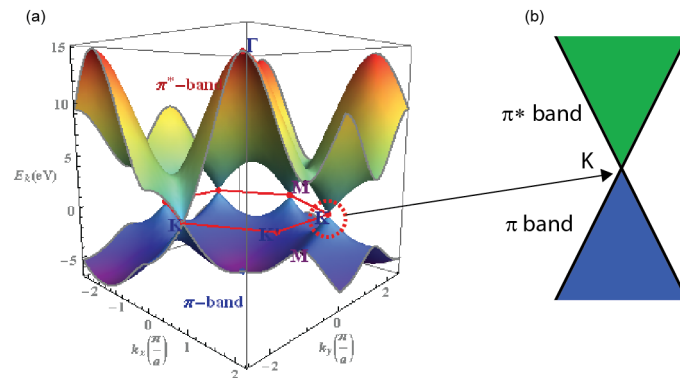
Figure 2.3: (a) The graphene 3D Brillouin zone showing the π and π^* bands. The plot was generated using the software MATHEMATICA. (b) Zoom in the K-points, showing the linear intersection of π and $\pi*$ bands.

2.1.2 Methods of graphene production

Since the isolation of the first graphene sheet using the continuous cleavage of graphite using scotch tape, a diversity of methods for producing graphene were developed. The method for producing graphene with the best structural and electronical properties is the mechanical cleavage of highly oriented pyrolitic graphite (HOPG) as it produces graphene flakes with high structural integrity [1]. This graphene is commonly used for fundamental studies, as it has a very low percentage of structural defects. However, the problem of uncontrollable flake size and thickness makes the process of producing such graphene flakes a practically random process. Furthermore, the flake sizes are of the order of micro- to millimetres, inhibiting the study of these samples with conventional photoelectron spectroscopy, for which samples of the order of centimetres are required.

A variety of methods have been developed during the past decade to tackle the problem of scalability and produce large graphene sheets [4] in order to render graphene commercially and technologically relevant. Some of these methods are: (a) liquid-phase exfoliation from graphite [28–30], (b) synthesis on silicon carbide (SiC) [31, 32] and (c) CVD synthesis of graphene [13, 21].

Liquid exfoliation of graphite is a method that has been developed for making the graphene production controllable and scale up the area of graphene layers on several substrates [28, 29, 33–35]. However, this method has been shown to introduce disorder in the graphene network

[36, 37]. Other methods, such as annealing of SiC(0001) at elevated temperatures as to produce the graphene network on top of the SiC wafer [32, 38] were intensively studied, but this method is relatively expensive due to the high cost of the SiC wafer and the high temperatures needed for the graphene production.

The graphene sheets used in this work are produced by chemical vapor deposition (CVD) on copper foil substrate [20]. This method is readily accessible and can provide high quality graphenes, also on a variety of transition metal substrates, such as nickel (Ni) [39], palladium (Pd) [40], ruthenium (Ru) [41], iridium (Ir)[42]. CVD production of graphene on copper has been proven to provide technologically relevant large areas of polycrystalline graphene sheets (up to 30 inches) with good quality [13, 20]. The process of production of graphene on copper foil is illustrated in Fig. 2.4. The procedure starts with nucleation of the carbon network on the Cu, resulting into polycrystalline graphene. Catalysis by metals such as copper is facilitated due to the ability of such metals to drive a reaction of low energy pathways by an easy change of oxidation state or via the formation of intermediate species [43]. In contrast to other transition metals, Cu has the 3d shell filled, leading to the lowest affinity to form carbide phases with carbon and very low carbon solubility compared to, e.g., Co and Ni [44]. Consequently, the Cu4s states in copper can only weakly interact via charge transfer with the sp^2 hybridised carbon atoms in graphene [45], making it very suitable as a catalyst for the formation of graphitic carbon.

The transfer of the graphene sheet from Cu to other substrates of interest usually leads to some defects in the graphene network, however, without hindering the potential of such graphene to be used in certain organic electronic devices, e.g., OPVCs, OLEDs or touchscreens. The transfer is facilitated with the use of polymer supports that are spin-coated on top of the graphene sheet [21]. Polymethyl-acrylate (PMMA) has been experimentally observed to produce the lower number of cracks and defects when used as a support, thus it is the most commonly used polymer for performing the transfer of the graphene sheets to various substrates of choice.
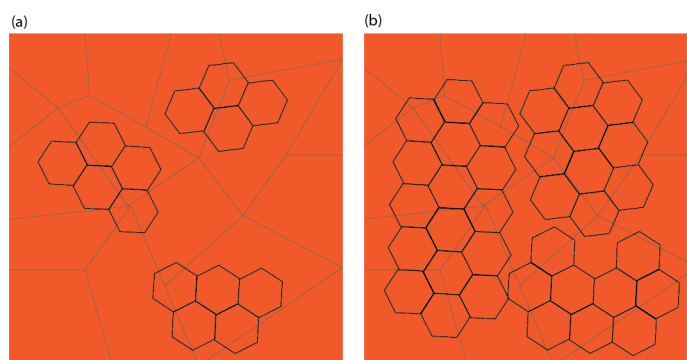
Figure 2.4: Schematic illustration of the graphene growth on copper using chemical vapour deposition (CVD). (a) Nucleation of graphene islands upon exposure to CH_4/H_2 atmosphere at 1000 °C and (b) the increase of the graphene islands with different lattice orientations leading to the polycrystalline graphene sheet. The lines represent domains on the polycrystalline copper foil.

2.1.3   Molecular functionalisation of graphene

This section outlines approaches that have been already used to covalently or non-covalently functionalise graphene. The choice between these two ways of functionalising graphene can strongly depend on the desired application.

Covalent functionalisation/chemisorption

Covalent functionalisation can be used for e.g., improving the solubility of graphene, opening of a band gap and conductivity- or work function-tuning of the graphene sheet [46, 47].

Graphene is chemically inert when compared to other species such as metals and it has been shown to protect metal surfaces from oxidation when used as a coating layer [48]. However, since the sp^2-hybridised carbon atoms in graphene are chemically unsaturated, under specific chemical treatments, they can covalently bond to other species.

Hydrogenation of graphene can lead to the attachment of hydrogen atoms along the carbon network, forming the so called graphane. This graphene-derived material exhibits a band gap, making it semiconducting [47, 49]. Fluorination is a way to attach fluorine atoms onto the carbon atoms of graphene, turning it into fluorographene. It has been proven to be a very effective way to manipulate the electronic properties, by open-

ing a band gap of 3 eV, and thus, turning the graphene from conductive to insulating. Moreover, this process leaves the mechanical strength of the graphene intact [50, 51]. Sulfonation is a method to attach -SO_3 groups [52] and ammonia or nitrogen treatment can be used to create amino (NH_2) groups [53] along the carbon network. Fig. 2.5 shows the covalent attachment of various other functional groups into the graphene network.
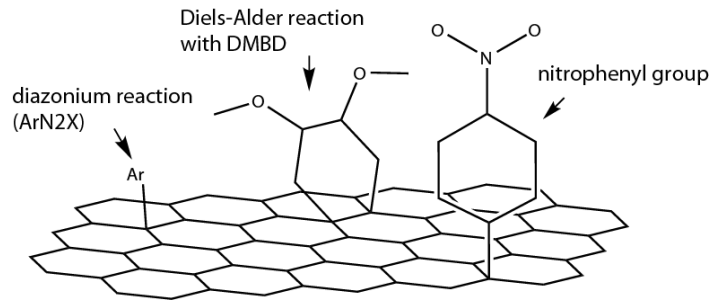

Figure 2.5: Schematic illustration of graphene covalently functionalised with different ligands. Figure adapted from [46].

Furthermore, a derivative of graphene, namely graphene oxide (GO) (Fig. 2.6) and reduced graphene oxide (rGO) include in their structures various oxygenated species such as carbonyl, epoxy and hydroxyl groups that are created during the oxidation of graphite. These groups facilitate molecular functionalisation and can be used to attach long chains to the GO, making it soluble in commonly used solvents such as tetrahydrofuran (THF), carbon-tetrachloride (CCl_4), etc [54]. Many such methods have been realised in the last decade to transform the hydrophobic nature of graphene or graphene oxide into hydrophilic by attaching various hydrophilic groups onto the basal plane of graphene.
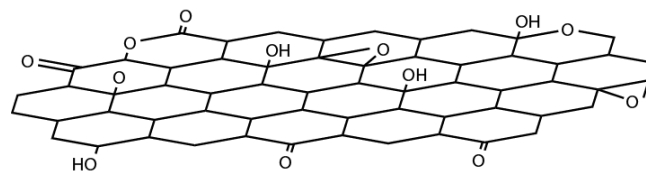

Figure 2.6: Schematic illustration of graphene oxide showing the various oxygenated species in the carbon network. Figure adapted from [46].

Summarizing, covalent functionalisation can be exploited to tailor the electronic and chemical properties of graphene. This comes entangled

with the disadvantage that the intrinsic electronic structure and thus, the physical properties of graphene get disrupted since covalent functionalisation causes a high perturbation to the electronic structure by converting the sp^2-hybridised carbon atoms to sp^3-hybridised ones. A further and major disadvantage is that it significantly decreases the charge carrier mobility in graphene [55], rendering this method inappropriate for this work, as the aim is the molecular functionalisation of graphene to produce highly conductive transparent electrodes.

Non-covalent functionalisation/physisorption

As an alternative to covalent functionalization, a very versatile method for functionalising graphene without disrupting the sp^2 network of carbon atoms [46] can be facilitated by using COMs that are electronically coupled with graphene via their aromatic network. Since the synthesis of such COMs gained tremendous attention in the past decades, nowadays, organic molecules can by synthesized according to the functionalisation one needs to achieve.

Applications of graphene functionalisation using COMs include:

1. Non-destructive surface doping using molecular adsorbates with either high electron affinity (EA) or low ionization energy (IE) that results in the effective tuning of the charge carrier type [56]. Such functionalisation can be utilized to produce a suitable replacement for the commonly used indium tin oxide (ITO) as a transparent, flexible and highly conductive electrode in organic (opto)electronic devices. In this way, one can engineer the energy levels of graphene as to tune the energy level alignment (ELA) at the hybrid interface between graphene and organic semiconductors. This surface doping can further increase the conductivity of the electrode without a major effect in the transparency of graphene, as to produce highly conductive transparent graphene/molecular electrodes.

2. Band-gap opening in graphene using the Bernal stacked bilayer graphene to increase the ON/OFF ratio for field effect transistor (FET) applications [57].

3. Functionalisation of graphene to produce molecular sensors [58, 59].

Conjugated organic materials can be used in order to increase the sensitivity and the selectivity of the graphene-based sensor using specifically designed molecules with double functionality: One end acts as a linker between the molecule and the graphene and the other can be a functional group suitably chosen to selectively target chemical or biological species.
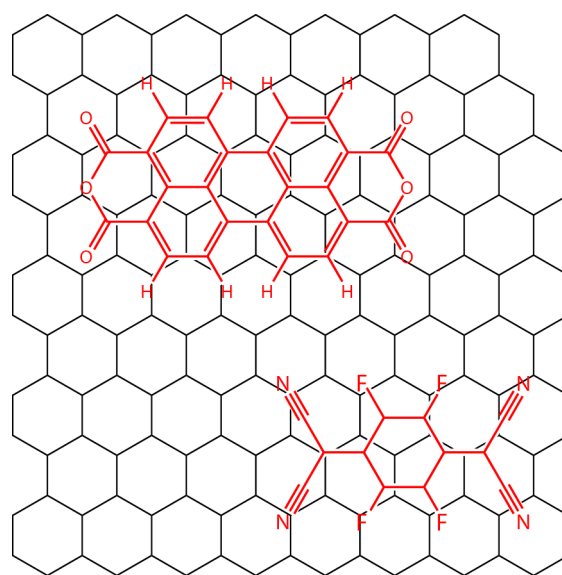
Figure 2.7: Schematic illustration of non-covalent functionalisation of graphene using conjugated organic molecules (COMs).

The aim of this work is the design of hybrid organic/graphene transparent and conductive electrodes. Therefore, mainly non-covalent functionalisation of graphene by organic molecules adsorbed on the surface as shown in Fig. 2.7 is considered, as to tune the energy levels in order to match the energy levels of commonly used organic semiconductors as transport materials in OLEDs, OPVCs etc.

2.2 Conjugated organic molecules

Organic molecules with predominantly alternating single and multiple bonds are said to be conjugated. As a result of this conjugation, their p_z orbitals form a delocalised electron network by forming π bonds. This con-

jugation in general leads to reduction in the overall energy of the system and increase in their stability.

COMs form closed shell systems, that lead to rather weak intermolecular interactions. Van der Waals forces are the principal forces governing intermolecular interactions in organic molecules. This additionally leads to low density of free charge carriers, being delocalised over the molecular structure [60], with their mean free path of the order of the intermolecular distances, i.e., the charge carrier mobility is typically low compared to metals or inorganic semiconductors.

Benzene is an example of the simplest π conjugated system, consisting of a single aromatic ring. Fig. 2.8a schematically shows the p_z orbitals perpendicular to the plane of benzene, while Fig. 2.8b illustrates the extended π network formed over the benzene structure as a result of delocalisation of the electrons in these orbitals due to the conjugation.
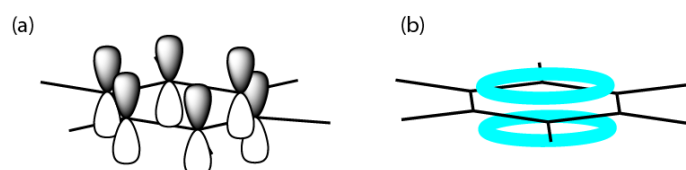

Figure 2.8: Benzene molecule showing a) the p_z orbitals and b) the extended π electron system across the aromatic ring.

The resulting molecular orbitals formed by COMs are occupied by electrons up to the highest occupied molecular orbital (HOMO) which is separated by an energy gap $E_{G,gas}$ from the lowest unoccupied molecular orbital (LUMO). The HOMO and LUMO orbitals, also called frontier energy levels of the COM, are of particular interest, since they are mainly involved in interactions. The energy level diagram in Fig. 2.9 shows the vertical ionisation energy (IE_{gas}) and electron affinity (EA_{gas}) of a molecule in the gas phase. IE_{gas} corresponds to the energy required to be given to an electron to be removed from the HOMO of the neutral molecule in gas phase and be brought to E_{vac}. EA_{gas} is the energy that is gained when an electron is brought from E_{vac} into the LUMO of the system. The E_{vac}, is the reference energy level, which is defined as the energy level that an electron can

escape from the atom [61].

In the presence of free charge carriers transporting through an OSC in a molecular solid, their surrounding ions move from their equilibrium positions to effectively screen the charge of the moving free charge carriers. Therefore, the electron and phonon cloud surrounding them gets polarised, leading to the formation of the so-called polaron energy levels, that are depicted simplistically in Fig. 2.9b. The free charge carrier together with the polarisation cloud is called a polaron. Polarisation effects have to be taken into consideration for the description of transport levels, that are the important energy levels when describing charge injection at an interface. In the case of a condensed molecular solid, the IE and EA are altered by the positive or negative polarisation energy.

The positive polarisation energy, E(P+), is given by [62]:

$$E(P+) = IE_{gas} - IE_{con} \,, \tag{2.9}$$

and the negative polarisation energy, E(P-), is given by:

$$E(P-) = EA_{con} - EA_{gas} \,, \tag{2.10}$$

with IE_{con} and EA_{con} being the ionization energy and electron affinity of the molecular solid.
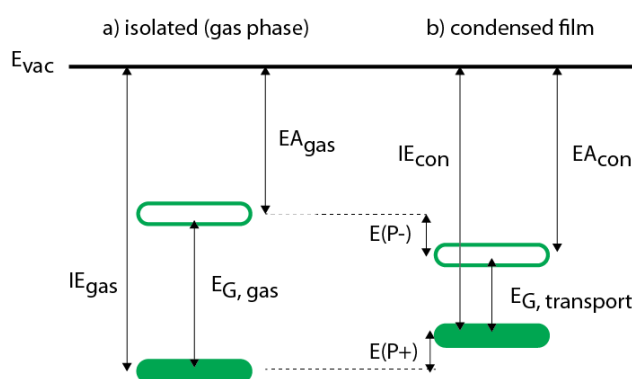
Figure 2.9: Schematic illustration showing the ionisation and affinity levels of a) an isolated singly ionised molecule in the gas phase. The ionisation energy (IE_{gas}), electron affinity (EA_{gas}) and the energy gap ($E_{G,gas}$) are shown. b) When the molecule is ionized in a condensed film, the energy levels are altered to IE_{con}, IE_{con} and the energy gap represents the transport gap, $E_{G,transport}$.

Strong electron acceptors or donors, are COMs of particular interest.

Their synthesis involves the chemical attachment of specific functional groups in order to induce strong electron affinity or low ionization energy. These COMs often undergo a (partial) charge transfer once they come into contact with electrodes, readily forming interface dipoles by causing a charge redistribution at the interface, resulting to the increase or decrease of the work function of the system [63–67]. Such COMs have been used also to cause binary organic-organic charge-transfer complexes and act as dopants [68, 69].

2.3 Organic electronics

Organic semiconductors have attracted enormous research attention due to their great potential in realising the field of organic electronics. The OSCs, that are commonly conjugated organic molecules, are the active materials in these devices. Some of their advantages over their inorganic counterparts include their light weight, mechanical flexibility, chemical diversity and easy and cheap processing. In Fig. 2.10 two already realised and marketable organic devices are shown, namely: (a) OPVC and (b) OLED.

The operation principle of the OPVC in Fig. 2.10a is to use a molecular electron acceptor and a molecular electron donor to form a planar heterojunction. When light with energy $h\nu$ enters the device, the organic layer will absorb the light, causing electrons to be excited into the LUMO and holes to stay behind in the HOMO, forming excitons, as indicated in Fig. 2.10a. The organic materials are chosen in such a way to have the correct IE and EA for generating a potential drop at the interface, that will in turn separate the electron/hole pair. Subsequently, the generated holes will be transported through the HOMO of the acceptor into the anode, whereas the generated electrons will be transported through the LUMO of the donor into the cathode and will get ejected. Apparently, a precise control of the ELA at the interfaces is crucial for the efficient operation of such a solar cell.

For the OLED in Fig. 2.10b, an electroluminescent (EL) organic material is sandwiched between an electron transport material (ETM) and a hole transport material (HTM). When holes and electrons are injected into the device from the anode and cathode respectively, the former travel through
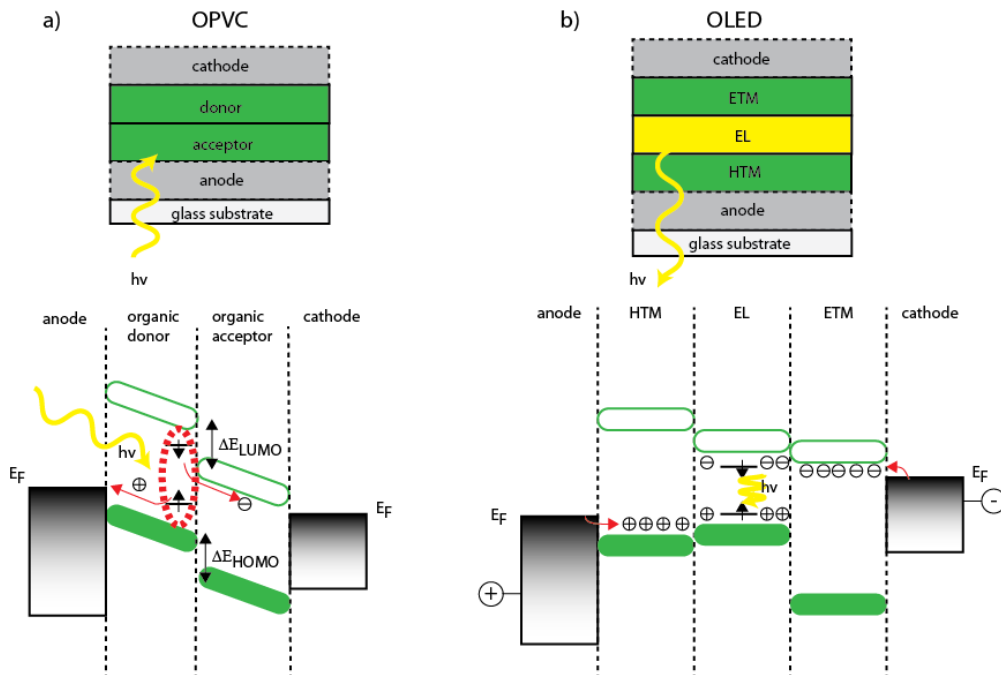
Figure 2.10: Schematic illustration showing (a) organic photovoltaic device (OPVC) and (b) organic light emitting diode (OLED) devices with their corresponding energy levels.

the HTM into the EL material, while the latter through the ETM into the EL material. Inside the EL material, holes and electrons will recombine emitting light in the process. As in the case with solar cells, the control of the ELA at the interfaces between all the materials very crucial to the operation of OLED devices.

2.4 Energetics at interfaces of electrodes

In this section the ELA taking place at interfaces between electrodes and COMs will be described and the concept of surface charge transfer doping will be introduced.

Vacuum level alignment vs vacuum level shift

Vacuum level alignment, also known as Schottky-Mott limit [70], is one of the first models used to calculate the ELA across electrode/OSC interfaces (see Fig. 2.11a,b). In this description, upon contact of an electrode with

an OSC, the energy levels of the organic material (IE and EA) determined separately (in gas phase measurements) were used to calculate the ELA occurring at the interface. In this case, the determining factor for the alignment of the energy levels after contact is the work function of the electrode. This implies that the determination of the hole/electron injection barriers (HIB/EIB), which are typically defined as the energy difference between the Fermi level (E_F) of the electrode material and the HOMO- or LUMO-charge transport threshold of the adsorbed COM respectively, are given by the simple equations as follows:

$$HIB = IE - \Phi \,, \tag{2.11}$$

and

$$EIB = \Phi - EA \,. \tag{2.12}$$

However, E_{vac} alignment, in many cases gives erroneous values even by more than $1\,\mathrm{eV}$ [61, 71], since it does not take into account physical or chemical interactions that take place at the interface.

One of the first understood deviations from the E_{vac} alignment rule was assessed theoretically for closed-shell noble atoms [72], such as xenon (Xe) adsorbed on metal surfaces. Since then, various studies have shown the deviation from the commonly assumed E_{vac} alignment in many other cases [61, 73, 74].

For example, when molecules only physisorb on atomically clean Au, the work function of the system was different than the work function of the individual gold electrode [75]. A qualitative picture of the interface energetics of the electrode/metal surface before contact with a COM is shown in Fig. 2.11c. In this illustration, the IE and EA of the COM are assumed for simplicity to remain constant before and after adsorption on the metal, with the parameter μ_b being the bulk chemical potential. SD is the surface dipole due to a large density of electron cloud spilling outside the surface of the metal and into vacuum. When COMs are deposited out of the surface of the metal, the "spilling out" electron cloud of the metal is pushed back into the bulk, altering the surface dipole and thus the overall work function of the metal. Thus, the work function of the metal/COM system differs from the work function of the individual metal
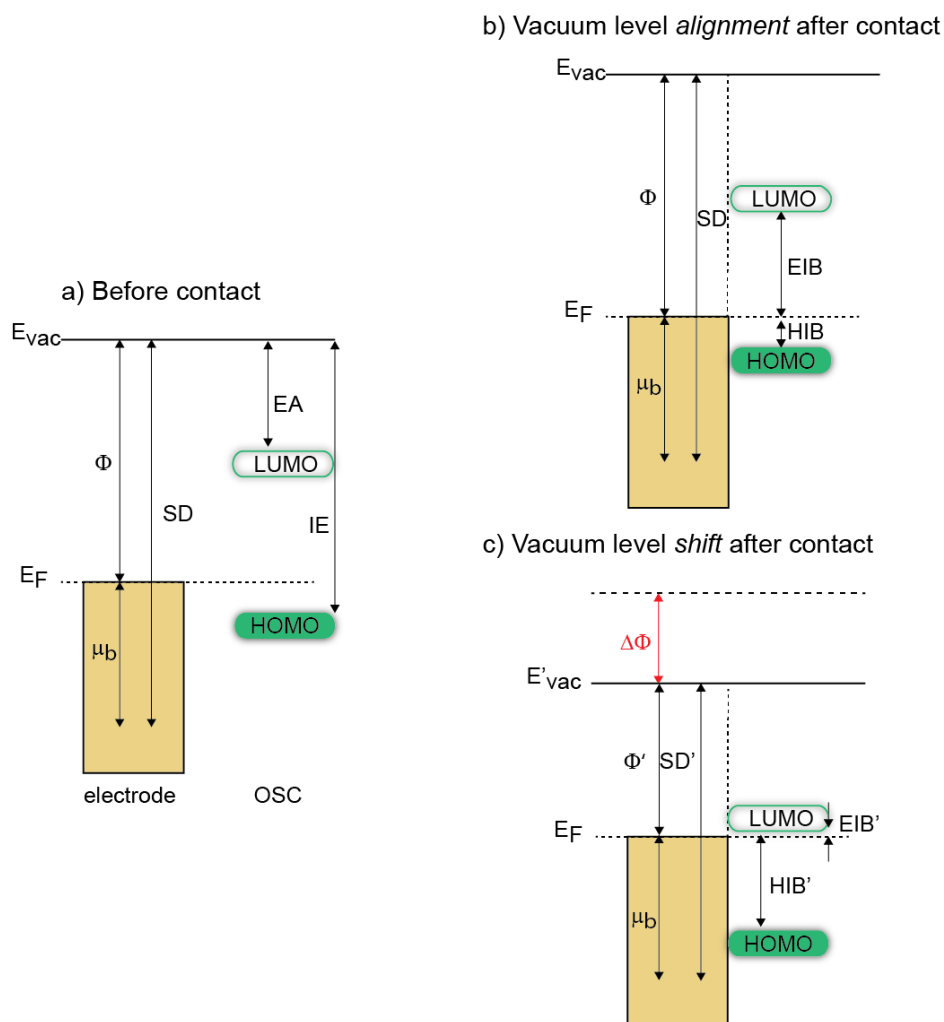
Figure 2.11: Schematic energy level diagram of an organic semiconductor (OSC) before (a) and after (b,c) adsorption on an electrode. In (b) the energy levels between the electrode and the organic layer are drawn considering that vacuum-level alignment takes place while in (c) the energy levels drawn in such a way that the vacuum level shifts after contact, due to the alteration of the surface dipole (SD) that leads to a work function shift ($\Delta\Phi$). The corresponding hole injection barriers (HIB) and electron injection barriers (EIB) are depicted, together with the ionization energy (IE) and electron affinity (EA) of the organic material.

alone, giving different HIB and EIB values than estimated by assuming E_{vac} alignment. This phenomenon of Pauli repulsion is termed "push-back" effect or "cushion" effect [61, 76].

The "push-back" effect, that causes the formation of interface dipoles (ID) and results in different energy level alignment than what is described in eq. 2.13 and eq. 2.14, results in the following equations for HIB and EIB:

$$HIB = IE - \Phi + ID \,, \tag{2.13}$$

$$EIB = \Phi - EA + ID \,. \tag{2.14}$$

Fermi level pinning

Fermi level pinning is the phenomenon where for a range of electrode work functions, the final work function reached after deposition of a molecular acceptor or donor is independent of the work function of the pristine electrode. Most of the organic (opto)electronic devices are fabricated in atmospheres such as high vacuum, controlled gas or ambient in order to reduce the manufacturing costs. Thus, materials used for the devices include a certain degree of surface contamination which turns their surfaces chemically inert, rendering their electronic coupling with COMs weak. Studies using such kind of chemically inert substrates with different work function to create interfaces with COMs [64, 77, 78] have shown that the energy level alignment at the interfaces follow, in general, the rule shown in Fig. 2.12. Since graphene is also a rather chemically inert material, it follows naturally that this rule will apply for graphene/COMs interfaces.

The dependence of HIB and EIB on Φ is characterised by the S-parameter [80], with S given by the following equation:

$$S = \frac{dE_F^{gap}}{d\Phi} \,, \tag{2.15}$$

giving the shift of the Fermi level into the energy gap of the OSC (E_F^{gap}), as Φ varies [79, 80].

In the range where $S \sim 1$, the HIB and EIB follow the decrease/increase of the work function Φ, i.e., E_{vac} alignment can be used to predict the en-
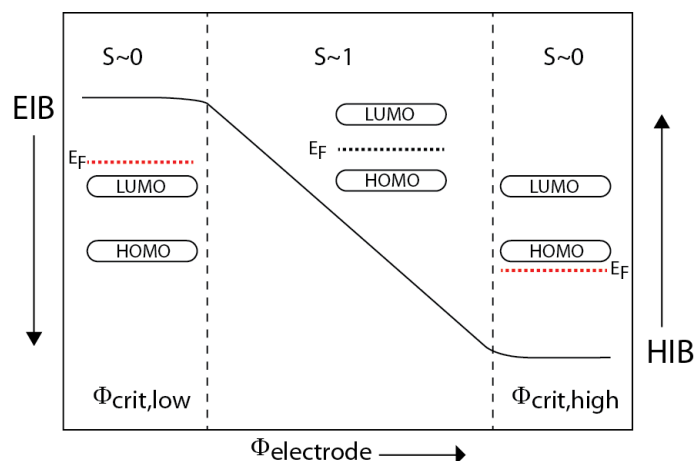
Figure 2.12: Schematic illustration showing the dependence of electron and hole injection barriers (EIB and HIB, respectively) of organic semiconductors on the work function of electrodes that are chemically inert. The inlets show the position of the Fermi level E_F with respect to the HOMO-LUMO gap of the organic semiconductor. $\Phi_{crit,low}$ indicates sufficiently low work function to induce electrons to flow from E_F into the LUMO of the organic semiconductor, resulting to pinning of the LUMO around E_F. $\Phi_{crit,high}$ corresponds to sufficiently high work function, to induce electrons to flow from the HOMO to the E_F, resulting in the pinning of the HOMO around E_F. Adapted from [79].

ergy positions of HIB and EIB. In this range, the E_F of the electrode falls within the HOMO-LUMO gap of the OSC, as shown schematically in the inlet in Fig. 2.12.

At S $\sim$ 0, Fermi level pinning controls the ELA. At these positions, the HIB and EIB do not change with alteration of the work function of the electrode. This phenomenon occurs, for electrodes with critically high ($\Phi_{crit,high}$) or critically low ($\Phi_{crit,high}$) work function, resulting in the E_F to fall into the unoccupied or occupied states of the organic semiconductor, respectively, if E_{vac} alignment were assumed, as shown in the inlets in Fig. 2.12, for the regions where S $\sim$ 0. When this occurs, the system is in the so called Fermi-level-pinned regime. This would bring the system out of thermodynamic equilibrium and interfacial charge transfer between substrate and organic semiconductor spontaneously takes place in order to guarantee thermodynamic equilibrium.

The pinning of E_F has been observed by ultraviolet photoemission (UPS) and inverse photoemission (IPES) [81, 82] to occur at energies large compared to the frontier energy levels of the organic semiconductors. This

results to minimised, but non-zero HIB and EIB values, different than what is expected if the E_F would be allowed to fall into the HOMO/LUMO of the neutral molecule.

The reason for Fermi level pinning occurring a few meV away from the frontier energy levels (HOMO or LUMO) of the OSC is not yet clearly resolved. One of the explanations is the integer charge transfer model (ICT) [83, 84]. Under the assumption that the surfaces are chemically inert, only integer charge could be transferred between substrate and COM (as partial charge transfer requires hybridisation and, thus, chemisorption). Consequently, cations (or positive polarons) form as a result of the migration of an electron from the HOMO to the substrate whereas, anions (or negative polarons) form when electrons enter the LUMO from the substrate.

Theoretical modelling has shown that the energy levels of the charged species follow the rule depicted in Fig. 2.13, i.e. a renormalisation of the energy levels occurs that reduces the HOMO/LUMO gap of the charged species with respect to the neutral species. Thus, the energy levels that these positive or negative polarons are occupying, will be the energy levels where Fermi level pinning will occur. Another possible explanation involves the presence of defect- or impurity- states that are present in the gap of the OSC. These states broaden the density of states (DOS) of the OSC and this causes a tailing of the distribution extending close to the E_F. Thus, the Fermi level pinning could occur at these electronic states [85].
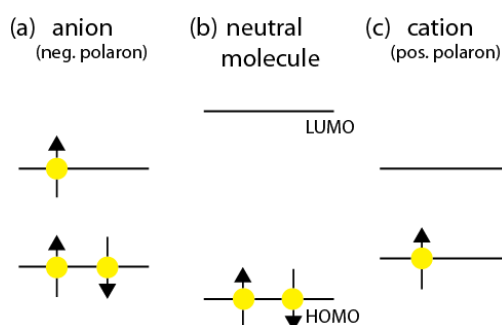

Figure 2.13: Scheme showing the energy levels of the ground state of (a) a negatively charged molecule (anion or negative polaron), (b) a neutral molecule, and (c) positively charged molecule (cation or positive polaron). Adapted from [79].

2.5   Tuning the work function of graphene

Interface dipoles

A lot of methods have been applied to tune the work function of electrodes. Examples of such kind of methods include:

1. Creating interfaces with COMs having an intrinsic dipole moment [86, 87].

2. Use of strong molecular acceptors or donors in order to induce charge transfer at the interface and thus creating an interface dipole [63–65, 88, 89].

3. Use of self assembled monolayers (SAMs) with intrinsic dipole moments attached on the surface of the electrode [90, 91].

The interface dipoles discussed above create a shift in E_{vac}, that can be calculated using Helmholtz's equation:

$$\Delta\Phi = \Delta E_{vac} = \frac{q\,n\,\mu}{\epsilon\,\epsilon_0}\,, \tag{2.16}$$

with $\Delta\Phi$ being the work function change, ΔE_{vac} the shift in vacuum level, q the elementary charge, n the dipole surface density, μ the dipole moment perpendicular to the surface, ϵ the dielectric permittivity of the organic material and ϵ_0 the vacuum permittivity. The assumptions taken for this equation to be valid is that there is no dipole-dipole interaction and polarisability of the COMs. The depolarisation effect is usually of the order of 100 meV, allowing for the Helmholtz equation to be used as a good approximation. A better model that does take into account the polarisability of the molecules is the Topping model [92], that includes the interaction between neighbouring dipoles. Instead of using this model though, an effective coverage-dependent dielectric constant can be used [93] together with Helmholzt's equation.

By controlling the magnitude of the dipole moment μ, together with the dipole areal density, one can tune the work function according to eq. (2.16).

Despite the fact that all the methods can achieve the adjustment of the work function, in the current work, the use of molecular acceptors
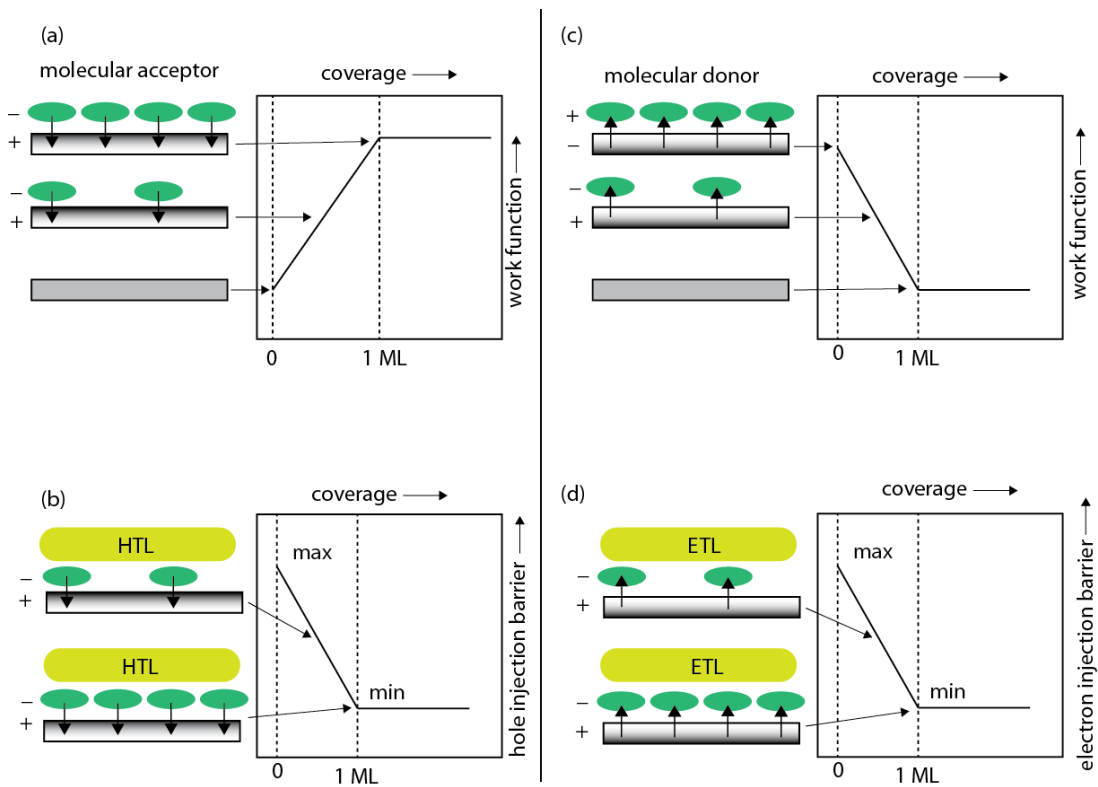
Figure 2.14: Schematic illustration showing the work function adjustment by the use of interface dipoles to a) increase and c) decrease the work function. b) and d) show the corresponding decrease of the hole injection barrier (HIB) and electron injection barrier (EIB) between the molecular electrode and the corresponding hole or electron transport material (HTL or ETL). Adapted from [79].

or donors is preferred. The reasons for selecting this route instead of the other methods is the fact that first, molecules with intrinsic dipoles are harder to control and can result in random antiferroelectric assemblies on the surface and secondly, SAMs have to be anchored on the surface by the formation of chemical bonds [94], which would result in the disruption of the electronic network of graphene. In contrast, the use of strong molecular acceptors/donors provides an effective way for controlling the direction of the dipole moment. Electron acceptors will result in a dipole moment having the vertical component facing towards the surface plane, whereas electron donors will result in a dipole moment facing away from the surface plane. The addition of such dipoles by increasing the material on the surface usually yields a continuous increase or decrease of the work function, until the first monolayer is completed, as shown in Fig. 2.14.

Surface charge transfer doping

Doping of inorganic semiconductors refers to the manipulation of their charge carrier density and conductivity by introduction of impurities in their crystal structure and is a significant technological tool in the field of (opto)electronic devices based on semiconductors [95].

Conventional doping is achieved by bombardment of the semiconductor with energetic ions that are incorporated into the lattice of the host semiconductor by ion implantation. According to the type of ion, the introduction of negative charge carriers can occur when the ion donates electrons into the conduction band of the semicondutor (n-type doping) or positive charge carriers when the ion accepts electrons from the valence band, leaving behind positive holes (p-type doping) [95].

In the search for novel and more gentle doping techniques that could be applied in nanoelectronics, the doping at the surface/near-surface region by using organic molecules that can act as electron acceptors or electron donors has been developed [56, 96, 97]. With this method, the exchange of electrons between the semiconductor and the surface dopant leads to an effective surface doping. The mechanism that drives the doping is the Fermi level pinning phenomenon. As described above, upon the formation of a solid/solid interface, if the E_F of the semiconductor lies above the LUMO or below the HOMO, the system comes out of thermo-
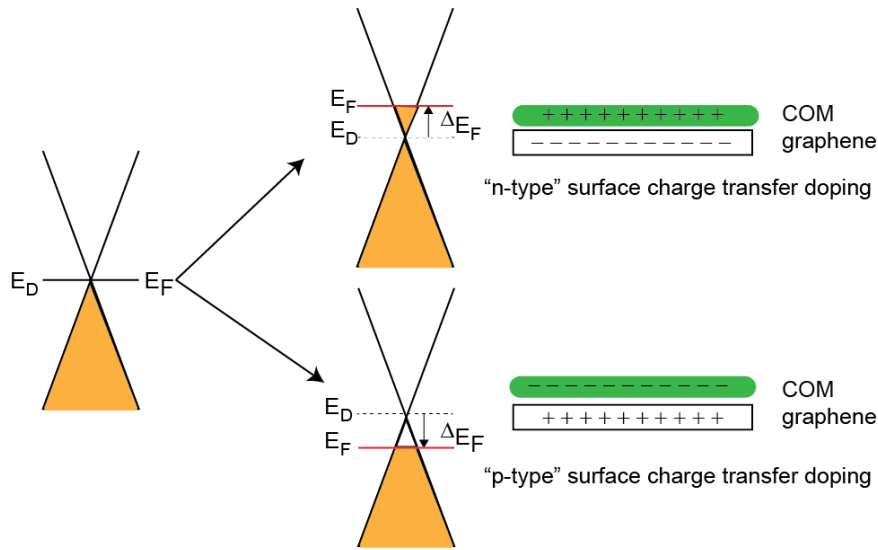
Figure 2.15: Schematic illustration showing how the Fermi level, E_F of graphene can be altered upon surface charge transfer doping, resulting in an electron enriched or electron poor graphene sheet. E_D is the energy of the Dirac point. Adapted from [47].

dynamic equilibrium, thus, charge transfer spontaneously occurs in order to bring the system back into equilibrium and Fermi level pinning occurs, as described in the previous section.

Consequently, the surface region or near-surface region would be doped by charge carriers [98]. The surface CT doping model was first introduced to explain the high surface conductivity that was found in diamond, a high band gap insulator [56, 96, 97, 99] and it was only recently invoked as a way to manipulate the conductivity of nanomaterials. This technique was further exploited in order to dope graphene epitaxially grown on SiC(0001) [100] using the strong molecular acceptor F_4TCNQ. For the case of graphene, Fig. 2.15 shows schematically the process. A COM that acts as a n-dopant shifts the E_F of graphene upwards, thus enriches the graphene sheet with electrons, whereas a COM that acts as a p-dopant shifts the E_F downwards, thus depletes electrons from the graphene sheet.

The following equation (2.17) is derived from the Dirac energy dispersion near the K-points (eq. (2.7)) and it can be used as an approximation to the doping of the graphene by introducing charge carriers due to the

adsorbed molecule [101]:

$$\Delta E_F = n^2\,\pi^2\,\hbar\,u_F\,, \tag{2.17}$$

with n being the density of charge carriers, u_F the Fermi velocity and ΔE_F the shift of the Fermi level E_F with respect to the Dirac point (located at the energy E_D).

Hence, in the case of graphene, the resulting work function change can be separated into two contributions: (a) shift of the vacuum level (ΔE_{vac}) due to formation of interface dipoles and (b) shift of the Fermi level due surface CT doping that induces a shift in the E_F with respect to the E_D (ΔE_F). Thus the work function change ($\Delta\Phi$) of graphene follows the equation:

$$\Delta\Phi = \Delta E_F + \Delta E_{vac}\,. \tag{2.18}$$

As a conclusion, the precoverage of the graphene electrode with a molecular acceptor or donor that finely tailors the surface potential, will result in reduced charge injection barriers (HIB or EIB) for the further deposited hole or electron transport layer, resulting to a better performance for the final organic electronics device.

2.6   Growth modes of thin films

Subliming organic molecules in vacuum is very crucial as only in this way, i.e. in the absence of a solvent, one can get direct access to the intrinsic interface properties. Furthermore, UHV is required as it provides clean and well-defined substrates for the subsequent deposition of the molecule. Under atmospheric pressure, surfaces are rapidly covered with adsorba such as water and other undefined organic species, making it impossible to access a clean surface. Therefore, each thin film used in this work was prepared by molecular beam deposition under UHV conditions.

The growth mode is a very important property of the organic material grown on the substrate since its structural properties affect strongly the electronic structure and the understanding of the energy level alignment at the interface formed[102, 103]. As molecules are resistively heated from a crucible, which is the usual deposition procedure in vacuum, they gain

enough kinetic energy to leave the crucible and travel onto the surface that is placed in the direction of the molecular beam created by the sublimation procedure. After coming into contact with the substrate, there is a certain probability to stay on it, depending on the sticking coefficient on the specific substrate.
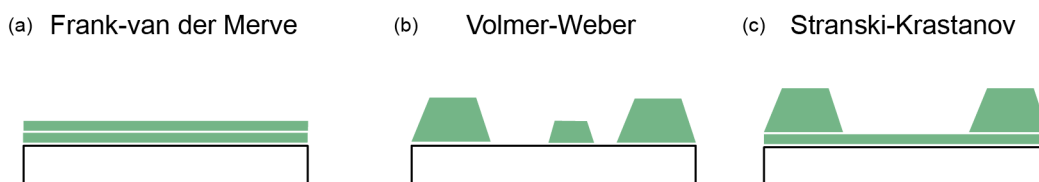

Figure 2.16: The three growth modes of thin films. (a) Frank-van der Merve, in which the film grows layer by layer, (b) Volmer-Weber, in which the adsorbates form islands on the substrate and (c) Stranski-Krastanov, in which the adsorbate initially forms a monolayer on the substrate and then forms islands on top of the first monolayer.

After the molecules are bound on the surface, a number of dynamic processes occur: a) inter-, intra- layer diffusion, b) nucleation, c) dissociation, 4) adsorption at special sites having higher surface energy, such as step-edges and defects [104].

The thin film growth proceeds in three steps: a) when the organic molecules reach the substrate they get physisorbed on the surface by losing their perpendicular-to-substrate velocity, b) as the adsorbed species are not in equilibrium, they explore different energetic states on the surface by moving on the surface as two-dimensional gas, until they find other adsorbed atoms, defects or species and start to cluster, c) clusters grow until they reach a thermodynamically stable radius. Then nucleation starts, resulting in one of the three different growth modes that come up dependent on the interplay between different components of the surface area of the clusters formed (Fig. 2.16):

- Frank -van der Merwe growth: This growth mode results if the adsorbate-surface interaction is stronger than the adsorbate-adsorbate interaction.This type of growth describes typical layer-by-layer growth (see Fig. 2.16a). The molecules start forming complete layers and the second layer starts forming only after the first one is completed.

- Volmer-Weber growth growth: The adsorbate-adsorbate interaction is stronger than adsorbate-substrate interaction. The molecules tend to aggregate as a result of this interaction in molecular assemblies, commonly named islands (see Fig. 2.16b). Consequently, the molecules tend not to completely cover the surface.

- Stranski-Krastanov: This is a combination of the previous two growth modes. The adsorbate-surface and adsorbate-adsorbate interaction is of the same order. Initially, a two-dimensional layer forms and then a three dimensional island formation proceeds (see Fig. 2.16b), when the interaction with the underlying substrate becomes weaker.

The growth of common organic molecules on surfaces have been thoroughly investigated [105, 106] but as novel and more complex molecules are synthesized in the growing field of organic electronics, in the same rapid speed the rules that describe the growth get more complex.

3 Experimental methods

In this work, two experimental techniques were mainly used: a) photo-electron spectroscopy (PES), for probing the valence and core electronic structure and b) NEXAFS, for obtaining information on the molecular orientation of a COM adsorbed on graphene.

The main source of light used was synchrotron radiation, hence a description of the synchrotron radiation and synchrotron facilities is provided, followed by a description of main principles of the PES and NEXAFS techniques.

3.1 Synchrotron radiation as light source for electron spectroscopy

The generation of electromagnetic (EM) radiation by electric charges under the influence of a radial force led to the development of synchrotron facilities, aiming to artificially keep charges, usually electrons, under the experience of a force to follow a curved path. The EM radiation produced has high degree of monochromaticity, brilliance and polarisability.

A synchrotron radiation facility mainly consists of an electron gun, a linear accelerator (linac), a storage ring and usually a booster ring, as shown schematically in Fig. 3.1.

Electrons are initially emitted from the electron gun and enter the linac, where they are accelerated up to ultra-relativistic speeds. They then enter the booster ring, which is a circular ring where the electrons gain more energy, and using magnets the beam of particles is being bent and focused. The magnetic field is increased synchronously with the particle energy in order to keep the charged particles on a circular path with constant radius. At a certain point, the charged particles effectively reach the desired relativistic energy and they are injected into the storage ring. The electrons are then set to an orbit in the storage ring, where they keep undergoing a radial acceleration.
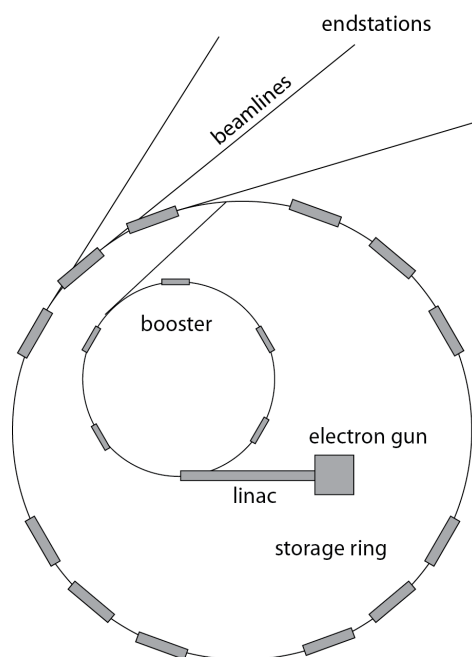
Figure 3.1: Typical setup of a synchrotron facility storage ring (outer circle) with the booster, that accelerates the free electrons, that are generated by the electron gun and are accelerated in the linear accelerator (linac). At several points along the storage ring, are situated openings for the photons that are guided through beamlines to the endstations, where the experiments take place.

The EM radiation is finally generated at the positions of bending magnets that keep the electrons on a closed circular path and in undulators/wigglers that are placed into the linear sections. At these positions, the electrons undergo an additional acceleration causing them to emit polarised EM radiation in a wide range of the EM spectrum. The radiation is transmitted into experimental chambers (endstations) through beamlines. In the path of such beamlines, a monochromator selects a single wavelength of the incoming radiation, thus producing a highly monochromatised beam of light and experiments can be performed with a tunable monochromatic X-ray source with a high degree of polarisation. These features of the beam are exploited in both PES and XAS [107].

3.2   Photoemission spectroscopy

For several decades, PES has been a very important spectroscopic tool for the study of electronic and chemical properties of materials. Its name

originated from the fact that it is based on (external) photoelectric effect
[108, 109]. The working principle of this technique is the excitation of elec-
trons by incident light, causing the photo-ionisation of the probed system.
The incident light with energy $h\nu$ that can be either highly monochromatic,
i.e., having only a single energy of $h\nu$, or non-monochromatised, which is
commonly used for laboratory X-ray and ultraviolet light sources, such
as magnesium (Mg) or aluminum (Al) anodes and helium (He) discharge
lamps. According to the excitation energy, $h\nu$, PES is divided into two cat-
egories: (a) UPS, for incident EM radiation in the energy range $h\nu = 10$ eV
- 100 eV and (b) XPS for excitation energy $h\nu > 100$ eV.

Surface sensitivity of PES

A characteristic property of the PES technique is its surface sensitivity. The
information depth that can be reached is rather small, of the order of sev-
eral Armstrongs (Å) and is determined by the electron mean free path.
This parameter is mainly determined by electron-electron collisions in the
energy range of the experimental studies, although electron-phonon inter-
actions play an important role at lower energies [110]. Fig. 3.2 shows the
"universal" curve for the electron escape depth, that describes the electron
mean free path, or information depth as a function of the photoelectron ki-
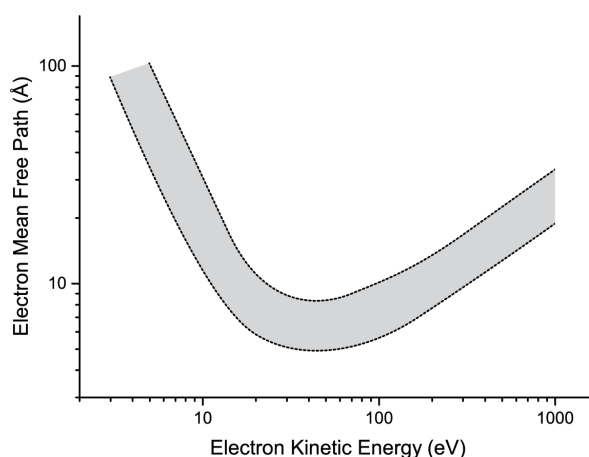netic energy.

Figure 3.2: The universal curve, illustrating the electron mean free path.
Adapted from [110].

For the energies used in this work, the information depth is several

Armstrongs, i.e., of the order of one (UPS) to a few (XPS) molecular layers [110, 111].

Transmission of electron from sample to analyser

Fig. 3.3 shows schematically the photoemission process. The sample gets irradiated by light with energy $h\nu$, exciting electrons by the photoelecric effect. The generated photoelectrons have to overcome the work function of the sample (Φ_s), before they are liberated. Thus, their kinetic energy (E_{kin}) is reduced by an amount equal to Φ_s. A typical photoelectron spectrometer, or electron analyser consists of an electrostatic hemispherical analyser and an electrostatic lens system. The electrons originating from the illuminated sample are focused into the analyser by the electrostatic lens system and are retarded so that they match the pass energy of the analyser. Subsequently, they follow a circular path due to the electrostatic potential in the hemispherical part of the analyser and they get detected.
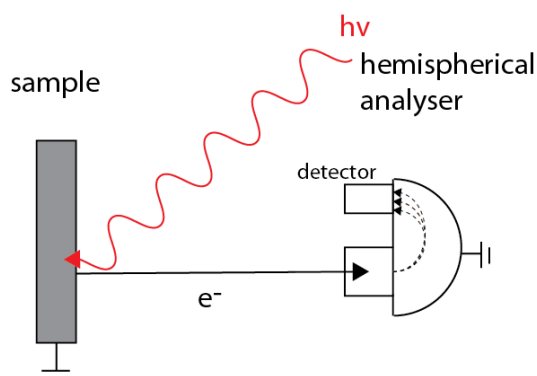
Figure 3.3: Schematic illustration showing the ejected photoelectrons from the sample after EM radiation of energy $h\nu$ is incident on it and the subsequent travel to the analyser where they are collected. The dotted lines represent circular paths of the electrons in the hemispherical analyser.

Energy distribution curve

The electron analyser measures the kinetic energy of the photoelectrons, generating an energy distribution curve, as illustrated in Fig. 3.4.

The electrons having the highest E_{kin} are the ones that are located closest to E_F. In the case of a metal, the highest energy electrons come directly

from the Fermi level since this is the highest energy level that electrons occupy. For organic materials, the electrons with the higher E_{kin} emerge from the HOMO. The E_F is the reference energy level of choice in PES of solid state materials, since the electron analyser and the sample are electrically connected, and E_F is aligned between analyser and sample.

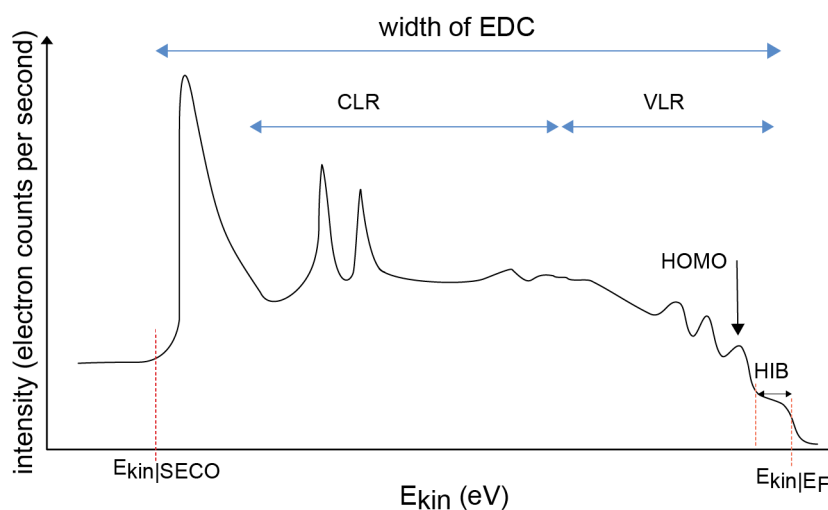Figure 3.4: Schematic of the energy distribution curve (EDC), which is typical spectrum obtained in a photoemission spectroscopy (PES) experiment. Important regions in the EDC is the core level region (CLR), the valence level region (VLR) and the secondary electron cut-off (SECO). From EDC, various values can be extracted, e.g., the highest occupied molecular orbital (HOMO) of a molecular thin film and the kinetic energy of the SECO onset ($E_{kin|SECO}$). $E_{kin|F}$ is the kinetic energy of the Fermi level.

At lower E_{kin} (or higher binding energy (BE), respectively) in the spectrum, the valence level region (VLR) is located. These features correspond the valence electronic states of the system, which, to a first approximation are equivalent to the density of occupied states (if selection rules and cross-sections are neglected). They are broad features, due to the fact that the photogenerated holes are coupled to the phonon vibrations resulting in a broadened linewidth [112]. At even lower E_{kin}, the core level region (CLR) is located. These features are localised core states and are generally narrower, with their intrinsic linewidth arising due to the non-zero lifetime of the photo-generated core-hole. At kinetic energies close to 0 eV, the sharp feature observed is termed secondary electron cut off (SECO). The corresponding electrons are inelastically scattered within the sample

and have lost the information about their initial state. This energy position of the SECO corresponds to the local E_{vac}, just outside the sample.

In addition to the intrinsic broadening of the features mentioned above, temperature and experimental broadening come also into play. The analyser entrance slit width, pass energy and the radius of the hemispherical analyser are the main experimental factors that create additional broadening to the spectra.
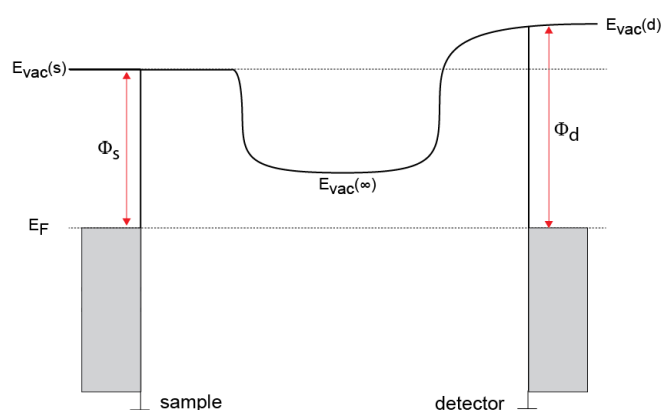
Figure 3.5: Schematic diagram of the vacuum levels (E_{vac}) between the electrically connected sample and electron analyser in a photoemission experiment. Φ_s and Φ_d are the work functions of the sample and detector respectively.

As shown in Fig. 3.5, in an actual photoemission experiment, the work function of the electron analyser (Φ_d), has to be considered when calculating the sample's energy levels. When $\Phi_d > \Phi_s$, the photoelectrons need to overcome an energy barrier equal to $\Phi_d - \Phi_s$ to be able to reach the electron analyser. In order to avoid the situation of losing information from photoelectrons that do not have enough E_{kin} to reach the analyser, the sample is held at a constant negative potential (V_{bias}) with respect to the electron analyser when measuring the SECO, in order to give the photoelectrons sufficient kinetic energy to overcome the work function of the analyser.

Ultraviolet photoelectron spectroscopy

UPS is used to measure energy levels such as Φ_s, HIB or IE of the organic material, e.g., at organic/electrode interfaces or bulk organic materials. Valuable information about the substrate-adsorbate interaction can be obtained, e.g., chemical interaction or charge transfer at the interface.

Φ_s can be obtained using the following relationship:

$$\Phi_s = hv - (E_{kin|E_F} - E_{kin|SECO}) - eV_{bias}\,. \tag{3.1}$$

The hole injection barrier (HIB) is obtained using:

$$HIB = E_{kin|E_F} - E_{kin|HOMO_{onset}}\,. \tag{3.2}$$

Finally, the IE of the organic material can be extracted using:

$$IE = HIB + \Phi_s\,. \tag{3.3}$$

X-ray photoelectron spectroscopy

X-ray photoelectron spectroscopy (XPS) is used to investigate core levels, providing both elemental and chemical state information.

In the CLR, the E_{kin} of the emitted photoelectrons are characteristic of the element they originate from, providing the possibility of elemental investigation. By taking into account the respective atomic cross-sections for photoemission and making use of the intensity ratio of the peaks, the stoichiometry of the sample can be calculated.
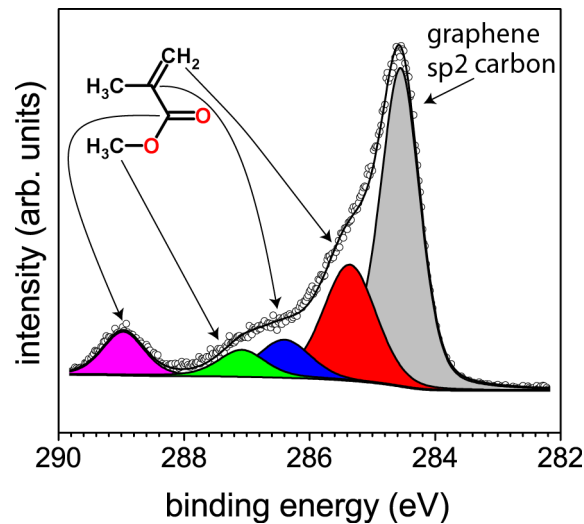

Figure 3.6: C 1s core level of polymethyl-acrylate (PMMA), spin-coated on graphene. The figure shows that the different chemical species can be identified using the energy positions of the peaks obtained by X-ray photoelectron spectroscopy (XPS), after deconvolution of the spectra.

The exact BE position of the peaks are altered by the local bonding or chemical environment and, therefore, provide the determination of the chemical state, as shown in Fig. 3.6. This can be used to investigate chemical reactions or to investigate charge-transfer interactions of the molecule with the surface, as all these can lead to energy shifts. Furthermore, XPS can be used to probe of contamination on substrates, impurities in adsorbed molecules and even to check the molecular integrity after the sublimation process.

Additionally, information about the growth mode can be obtained, by observing at what coverage the substrate features get significantly attenuated. When for e.g., the growth follows the Volmer-Weber mode (see Fig. 2.16b, rapid damping of the substrate features will be observed, whereas in the case of Frank-van der Merve (see Fig. 2.16a) or Stranski-Krastanov (see Fig. 2.16c) modes the substrate features get quenched only at very high coverages.

Theory of the photoemission process

The excitation of a photoelectron is a complex process [110, 113], with the sample always representing a many body system that is involved as a whole in the photoemission process. A very short but concise account is given in the contribution by e.g., Borstel et al. [114] and a very comprehensive description is given in the textbook of Hüffner [110].

A lot of models have been proposed to describe the photoemission process, with the simplest one being the three-step model proposed by Berglund and Spicer [115], that gives a phenomenological account of the process by splitting it into three steps: 1) excitation of an electron in the material by the incident EM radiation, 2) propagation of the electron within the material to the surface and 3) escape of the electron from the surface into the vacuum. These three steps are treated separately and in this framework, self-energy corrections, giving rise to energetic shifts and damping processes are neglected [113].

By splitting the photoemission process in three steps, the total external

emission current I^{ext} is written as follows [115, 116]:

$$I^{ext}(E'_{kin}, h\nu, \boldsymbol{k}) = I^{int}(E_{kin}, h\nu, (k)) \cdot T(E_{kin}) \cdot X(E_{kin}, \boldsymbol{k}) \,, \qquad (3.4)$$

with E_{kin} denoting the kinetic energy of the electron, $h\nu$ the photon energy, $I^{int}(E_{kin}, h\nu, \boldsymbol{k})$ the internal photoelectron current desnity, $T(E_{kin}, \boldsymbol{k})$ the transport function and $X(E_{kin}, \boldsymbol{k})$ the escape function.

In the first step, Fermi's golden rule as a result of 1st order perturbation theory is used to give the probability of transition w per unit time (transition rate) for an electron initially in the state Ψ_i to a final state Ψ_f. H′ is the perturbation causing this excitation (incident EM radiation). The transition probability per unit time, w, given that the perturbation H′ is small, is given by:

$$w = \frac{2\pi}{\hbar} \left|\langle \Psi_f | H' | \Psi_i \rangle\right|^2 \delta\left(E_f - E_i - h\nu\right) \,, \qquad (3.5)$$

with E_i and E_f are the energies of the initial and final states, $h\nu$ the incident photon energy.

$\left|\langle \Psi_f | H' | \Psi_i \rangle\right| = M_{if}$ are the transition matrix elements.

The perturbation caused by the incident radiation is:

$$H' = \frac{e}{2m_e\,c} \left(\mathbf{A} \cdot \mathbf{p} + \mathbf{p} \cdot \mathbf{A}\right) - e\Phi_{light} + \frac{e^2}{2m_e c^2}\mathbf{A} \cdot \mathbf{A} \,. \qquad (3.6)$$

$\mathbf{A}$ and Φ_{light} are the vector- and scalar- potentials of the incident EM field, e and m_e are the electron charge and mass, c is the velocity of light and $\boldsymbol{p}$ is the momentum operator.

Thereafter, a certain number of approximations are applied to the perturbation in order to reduce the problem. The last term that contains $\mathbf{A.A}$ describes the interaction between the photon field and does not contribute to one-photon processes and it is neglected. Furthermore, the intensity of the photon flux is relatively low to give a large value to this term in common photoemission experiments.

We assume that the wavelength $\lambda = \dfrac{2\pi}{q} \gg$ typical atomic distances. This allows us to use the electric dipole approximation, where the vector

potential can be expressed as:

$$\boldsymbol{A} = \boldsymbol{A_0} \, exp(\frac{iq}{r}) \approx \boldsymbol{A_0} \,. \tag{3.7}$$

Finally, by applying a Coulomb gauge, where $\nabla.\boldsymbol{A} = 0.$ this removes the Coulomb potential Φ from the equation.

The resulting perturbation is then:

$$H' = \frac{e}{m\,c}\boldsymbol{A_0} \cdot \boldsymbol{p} \,. \tag{3.8}$$

Hence the resulting transition probability w, becomes:

$$w = \frac{2\pi}{\hbar}\frac{e}{m_e c}\,|\langle \Psi_f \,|\boldsymbol{A_0} \cdot \boldsymbol{p}|\, \Psi_i\rangle|^2 \,\delta\left(E_f - E_i - h\nu\right) \,, \tag{3.9}$$

with the transition dipole moment, $M_{if} = |\langle \Psi_f \,|\boldsymbol{A_0}.\boldsymbol{p}|\, \Psi_i\rangle|^2$. After summing over all the initial and final states the internal photoelectron current density is [116]:

$$I^{int}(E_{kin}, h\nu, \boldsymbol{k}) \propto \sum_{i,f} M_{i,f}\delta\left(E_f(\boldsymbol{k}) - E_i(\boldsymbol{k}) - h\nu\right)\delta(E_{kin} - E_f(\boldsymbol{k})) \,. \tag{3.10}$$

The term $\delta(E_f(\boldsymbol{k}) - E_i(\boldsymbol{k}) - h\nu)$ in the expression indicates that the photoelectron current density is proportional to the density of occupied states in the material. This means that, indeed, the EDC in the PES experiment gives an approximation to the density of the occupied states of the material. Furthermore, the transition dipole moment M_{if} gives the probability of a certain transition to happen. This is given by the dot product between the vector potential of the incident light $\boldsymbol{A_0}$ and the momentum of the electron $\boldsymbol{p}$, giving the selection rules in the photoemission process.

The 2nd step of the photoemission process involves the propagation of the excited electron to the surface. A number of these electrons will be scattered inelastically during their travel to the surface, thus losing their information about their initial state and be a part of the secondary electron background in the spectrum. The number of electrons that are not being scattered inelastically during the propagation inside the material, are determined by the mean free electron path (see Fig. 3.2). The transport

function is proportional to the function describing the mean free electron path.

Finally, in the 3rd step of the photoemission process, the electron escapes from the surface of the solid after being scattered by a surface potential [116] and is transmitted into the vacuum, where it further travels to the electron analyser, where it is collected and measured. During this process, the parallel component of k is conserved, while the normal component of k is not. The parallel component of the photoelectron that escaped the material is given by [98]:

$$\boldsymbol{k}_{\parallel}^{ext} = \sqrt{\frac{2m}{\hbar^2} E_{kin} sin(\alpha)}\,, \tag{3.11}$$

with α the emission angle of the photoelectron as it escapes the solid, with respect to the surface normal. This equation makes the measurement dependent on the experimental parameter α.

Many body effects

After excitation of the system by incident light, the generated photoelectron travels out of the sample, leaving behind a photohole that disturbs the electronic structure of the surrounding system. The excited photoelectron feels the Coulombic attraction of the photohole during its travel out of the sample. Depending on the nature of the substrate, the effect of screening of the photohole from the surrounding electrons can significantly vary.
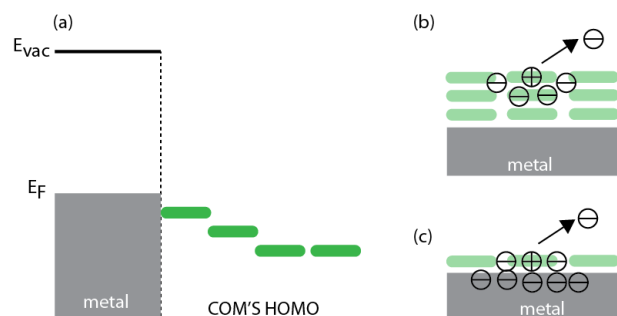

Figure 3.7: (a) Energy level diagram of the highest occupied molecular orbital (HOMO) of a conjugated organic material (COM) adsorbed on a metal at increasing distance from the COM/metal interface (b) Screening effect by the surrounding of the photohole when the thickness is in the multilayer regime and (c) monolayer regime.

Fig. 3.7a shows the energy level diagram of the HOMO of a COM adsorbed on a metal substrate, with increasing distance of the COM from the substrate. Fig. 3.7b shows the efficiency of the screening of the photohole by the surrounding organic material in the multilayer regime, and Fig. 3.7c the screening by the metal substrate in the monolayer regime. In the monolayer regime, the electrons in the metal can screen the photohole more efficiently than in the multilayer case. Thus, the ejected photoelectron feels less Coulombic attraction by the photohole and thus it shows up in the EDC at a lower BE. In the multilayer, the screening effect is weaker and the photoelectron feels more Coulombic attraction by the photohole, thus it appears to have higher BE in the EDC.

Fig. 3.8 shows two additional characteristic electronic processes that invoke many-body effects and lead to extra peaks in the photoemission spectrum. These features are more commonly observed in XPS than UPS. The most commonly observed peaks are termed shake-up and shake-off lines [110, 117] and they are the result of two-electron processes where a valence electron is excited during the extraction of a core level electron. If the valence electron is excited into a higher bound energy level (E_{bound}), a shake-up feature is created, while if the valence electron is emitted out of the solid, a shake-off feature is induced. The energy difference of the shake-ups from the main core-level peak is related to the HOMO-LUMO energy difference.
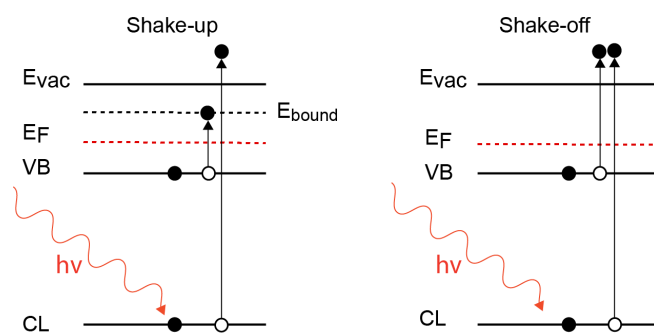

Figure 3.8: Schematic illustration showing two important many-body processes. Shake-up and shake-off features correspond to the excitation of a valence electron into a bound state, E_{bound} and the excitation of the valence electron out of the solid, respectively.

3.3 Near edge X-ray absorption spectroscopy

X-ray absorption spectroscopy probes the excitation of core level electrons into unoccupied or half-filled states, generating the X-ray absorption spectrum that is usually separated into two parts: (a) near-edge X-ray absorption fine structure (NEXAFS), for the absorption fine structures up to $\sim$30 eV above the absorption edge and (b) extended X-ray absorption fine structure (EXAFS), that extends up to 1000 eV above the absorption edge. In this work, we used NEXAFS to probe resonant excitations from 1s core level states (N 1s) to unoccupied states, in order to extract information about the orientation of the molecular monolayer.
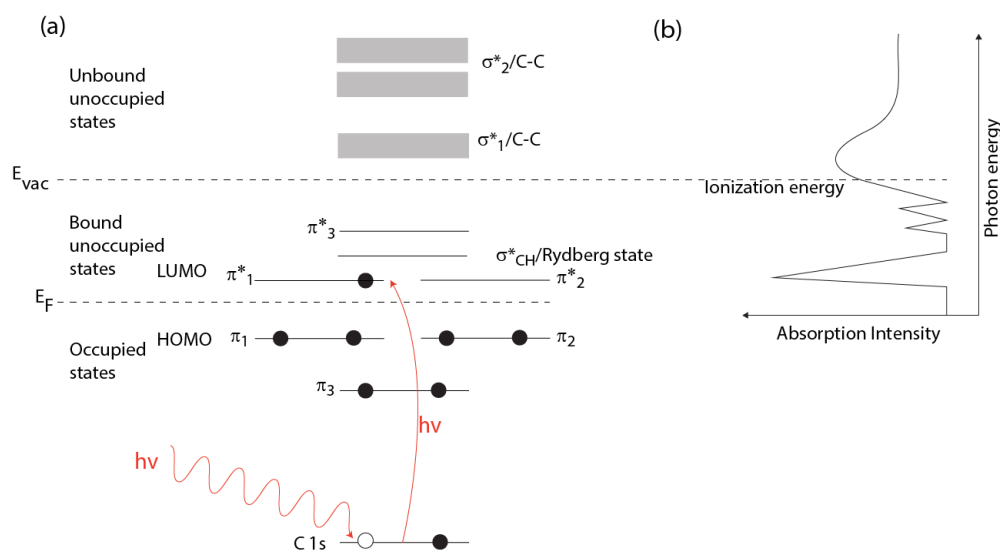
Figure 3.9: Schematic illustration depicting (a) the X-ray absorption process for a simple molecular system, benzene, together with the energy states of the system in the gas phase and (b) the typical NEXAFS spectrum at the C K-edge. LUMO is the lowest unoccupied molecular orbital, HOMO is the highest occupied molecular orbital, E_F is the Fermi level, E_{vac} is the vacuum level. The figures are adapted from [118].

The absorbed X-rays excite core electrons, inducing their transition into unoccupied states. Fig. 3.9a illustrates the absorption of a photon by a core level and the subsequent excitation into an unoccupied state of the model molecule benzene, generating its NEXAFS, as drawn schematically in Fig. 3.9b. Near the absorption edges, a series of fine structures appear. For the case of organic molecules, these fine structures are dominated by

resonances predominantly arising from transitions into unoccupied π^* or Rydberg states, as illustrated for benzene in Fig. 3.9.

The dipole selection rules apply for the NEXAFS transitions:

$$\Delta l = \pm 1, \Delta j = \pm 1, \Delta s = 0 \,, \tag{3.12}$$

with l the angular momentum quantum number, j the total momentum quantum number and s equal to the spin quantum number.

These dipole selection rules give rise to the absorption edges in the NEXAFS spectrum, that are classified according to the origin of the excited electron. For K-edge excitations, that concerns the current work, the dipole selection rule $\Delta l = 1$ allows transitions into final states having an atomic p orbital component.

The X-ray absorption cross-section describes the probability for absorption of a photon by an atom. When the photon energy, $h\nu$, matches the energy required for a transition, the X-ray absorption spectrum shows maxima and the intensity decreases monotonically after the core-edge.

The absorption cross section (σ_x) is defined as the number of electrons excited per unit time divided by the number of incident photons per unit time per unit area [119]. Within the dipole approximation:

$$\sigma_x = \frac{4\pi^2\hbar^2}{m^2} \cdot \frac{e^2}{\hbar c} \cdot \frac{1}{h\nu} \cdot \left\langle \Psi_f \left| \boldsymbol{E} \cdot \boldsymbol{\mu} \right| \Psi_i \right\rangle^2 \rho_f\left(E\right) \,, \tag{3.13}$$

with σ_x the absorption cross-section (usually given in cm^2 or barn), $\hbar$ the reduced Planck constant, c the speed of light, e the electron charge, m the electron mass, $h\nu$ the photon energy, $\boldsymbol{E}$ the electric field vector, $\boldsymbol{\mu}$ the electric dipole operator, Ψ_f the wavefunction of the final state, Ψ_i the wavefunction of the inital state and $\rho_f(E)$ the density of final states.

Elemental information using NEXAFS

NEXAFS is element specific, since the absorption edges of elements have characteristic energies. Furthermore, it is sensitive to the bonding environment within different functional groups. Therefore, it can be used to determine chemical compositions of complex species (e.g. polymers) with great accuracy (Fig. 3.10a).

Orientation analysis with NEXAFS

MOs are highly directional, as shown in Fig. 3.10b with the orbital vector of the final state orbital, $\boldsymbol{O}$, describing a specific orbital direction within a molecule. Thus, by varying the electric field direction, $\boldsymbol{E}$, with respect to the final state orbital vector, $\boldsymbol{O}$, information about the orientation of the COM on a surface can be extracted. The angular dependence of the matrix element, using eq. (3.3), is given by:

$$\left| \langle \Psi_f \left| \boldsymbol{E} \cdot \boldsymbol{\mu} \right| \Psi_i \rangle \right|^2 . \tag{3.14}$$

In the case of a linearly polarised light, it results to:

$$\left| \boldsymbol{E} \right|^2 \left| \langle \Psi_f \left| \boldsymbol{\mu} \right| \Psi_i \rangle \right|^2 , \tag{3.15}$$

and for a transition from a 1s orbital, $\left| \langle \Psi_f \left| \boldsymbol{\mu} \right| \Psi_i \rangle \right|^2$ points along $\boldsymbol{O}$. The transition probability is then given by:

$$w \propto \left| \boldsymbol{E} \right|^2 \left| \langle \Psi_f \left| \boldsymbol{\mu} \right| \Psi_i \rangle \right|^2 \propto \left| \boldsymbol{E} \right|^2 \boldsymbol{O} \right|^2 \propto cos^2 \delta , \tag{3.16}$$

with δ the angle between $\boldsymbol{E}$ and $\boldsymbol{O}$. Using simulations to identify transitions, the direction of $\boldsymbol{O}$ can be found, and consequently the angle between this vector and $\boldsymbol{E}$ can be calculated, hence the orientation of the molecule on the substrate can be evaluated.
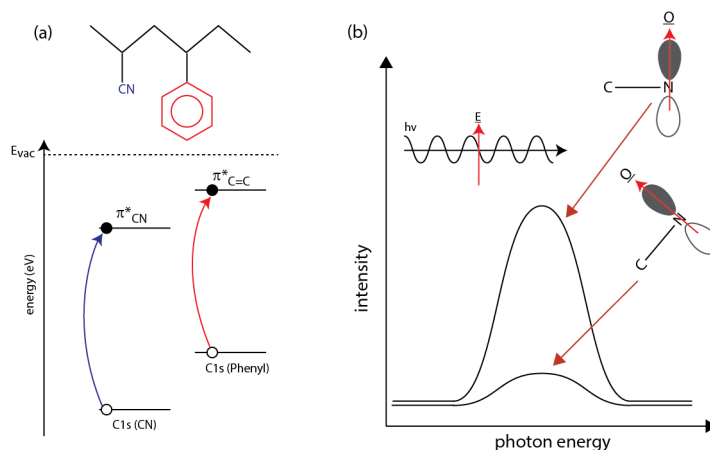

Figure 3.10: (a) NEXAFS transitions from the carbon 1s core level (C 1s) into unoccupied states of two different functional groups, allowing for the elemental determination, (b) Different absorption intensity depending on the direction between the orbital vector $\boldsymbol{O}$ and the electric field vector $\boldsymbol{E}$.

4 Materials and experimental details

In this section, at first the investigated organic materials and the used substrates are presented. Then, the experimental setups with which UPS, XPS and NEXAFS measurements were performed will be introduced and relevant experimental details will be discussed.

4.1 Materials

The investigated COMs and employed substrates will be shown in this section, together with the respective motivation for choosing them.

4.1.1 Molecular acceptor and donors

The main aim of this thesis was the work function tuning of single layer graphene by using technologically relevant molecular acceptors and donors. Their technological relevance is defined by their air stability and low volatility. Four different COMs were studied, two electron donors and two electron acceptors. Fig. 4.1 presents an overview of the chemical structures together with the full names, abbreviations and suppliers of all the organic molecules used in this work.

The first organic molecule studied is hexaazatriphenylene-hexacarbonitrile (HATCN), synthesized and provided by Max Planck Institute for Polymer Science, Mainz, Germany. This COM is already known to cause a density dependent re-orientation when deposited on Au(111) and Ag(111) [88, 120] and is shown to induce a charge transfer when deposited on metals, metal oxides and organic molecules and thereby increase their work function by more than $1\,\mathrm{eV}$ [64, 88, 89, 121].

Hexafluoro-tetracyanonapththoquinodimethane (F_6TCNNQ), synthesized and provided by NOVALED, Dresden, Germany is a strong molecular acceptor with higher molecular weight (sublimation temperature 130°) than the commonly used strong electron acceptor F_4TCNQ (sublimation

temperature 90°) [63, 122, 123]. F_6TCNNQ has been already used success-fully as p-dopant for organic molecules, such as pentacene [124, 125].

The two donor molecules, i.e., the dimer of pentamethylrhodocene ([RhCp*Cp]$_2$) and the dimer of pentamethyl-cyclopentadienyl-trialkylbenzene-ruthenium ([RuCp*mes]$_2$) were synthesized and provided by Georgiatech, Atlanta, USA [126–129]. These two donors are relatively novel dimeric organometallics with very low IE, that have been used in solution to ef-fectively n-dope graphene and were additionally used to n-dope organic semiconductors [129, 130].

The organic molecules were sublimed using resistively heated quartz crucibles at sublimation rates of about 0.2 nm/min. The film mass-thickness was monitored using a quartz crystal microbalance (QCM). The mass density used for all the molecules was 1.35 g/cm^3, except for HATCN, for which 1.6 g/cm^3 was used [131]. During molecular sublima-tion the pressure was kept below $1 \cdot 10^{-8}$ mbar. All preparation steps and measurements were performed with the substrate at room temperature and in UHV.

4.1.2   Substrates

Most experiments have been performed on monolayer graphene on two different supports. The technologically relevant substrate is G/Qu and experiments were also performed on G/Cu. Additionally, experiments have been performed on highly oriented pyrolytic graphite (HOPG).

HOPG (ZYB grade) was cleaved in ambient atmosphere before being loaded into the preparation chamber. It was then annealed at 500 ° for 12 hours. G/Qu was annealed for different time periods, from 6 h to 24 h at 600°C, in order to check the effect of annealing time to the resulting purity of the substrate. The annealing procedure for obtaining clean graphene-on-quartz substrates will be discussed in more detail in section 5.1.
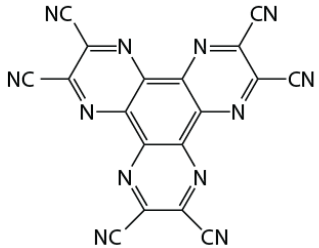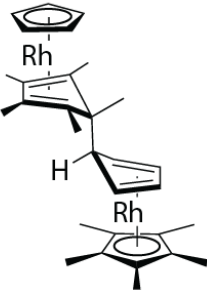
Figure 4.1: Chemical structures, abbreviations, full chemical names and suppliers of the investigated molecules.
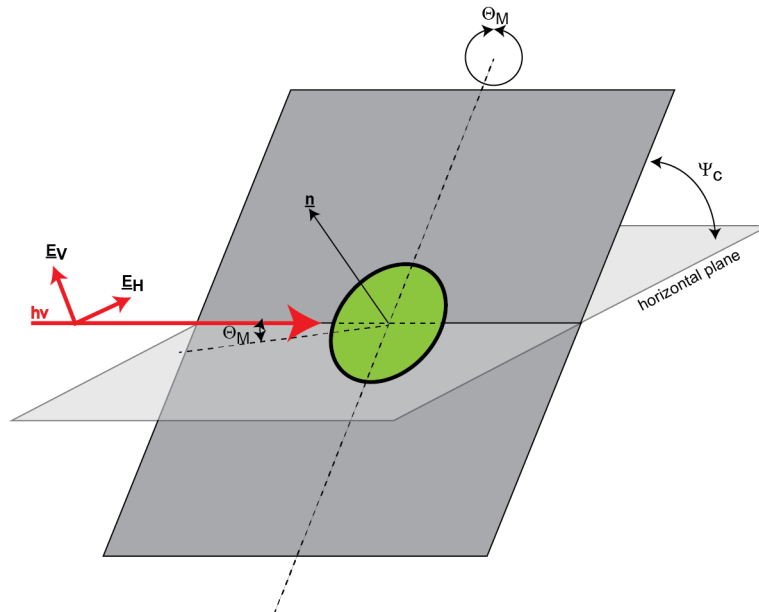
Figure 4.2: The experimental NEXAFS geometry at the BEAR beamline. The electric field vector of the elliptically polarised X-rays has a horizontal (major) component E_H and a vertical component E_V. Θ_M is the incidence angle of the light with respect to the surface plane and Ψ_C is the rotational angle of the experimental chamber which is the same as the rotational angle of the sample around the beam axis. $\mathbf{n}$ is the surface normal.

4.2 Experimental

4.2.1 Endstation BEAR

NEXAFS measurements were performed at the BEAR endstation at the ELETTRA synchrotron facility in Trieste, Italy. This endstation is located at a bending magnet which provides radiation in the energy range between 3 - 1600 eV, with a final spot size of 30μm $\cdot$ 100μm. The endstation features a rotatable analysis chamber, optimized for X-ray absorption measurements [132, 133].

NEXAFS spectra were collected in total electron yield mode (drain current mode) at the N K-edge. The incident light was elliptically polarised with the major component in the horizontal plane (E_H); the incidence angle of the light with respect to the sample surface plane (Θ_M) was kept fixed at $10°$. The chamber was then rotated around the beam axis (Ψ_C), producing an effective rotation of the electric field vector with respect to the surface plane, hence the relative polarization of the light with respect

to the sample surface plane was changed. Using this setup, the excitation volume was kept constant [134]. The process is shown schematically in Fig. 4.2.

4.2.2   Endstation SURICAT

The major part of the PES data presented in this work were recorded at the third generation synchrotron light source facility BESSY II, Berlin, Germany at the endstation for Surface Investigation and Catalysis (SurI-Cat). The beamline SurICat is equipped with a plane grating monochromator operated with collimated light, in an energy range from 20 eV - 2000 eV. An aluminium filter was used for all experiments involving organic molecules, in order to decrease the photon flux impinging on the organic material. This is crucial in order to avoid degradation of the organic material due to irradiation. The spot size of the beam is $\sim 50 \ \mu m^2$ and the light was horizontally polarised. The electron analyser used was a hemispherical analyser (Scienta SES 100).

The UHV system at this endstation consists of a preparation chamber at base pressure $1 \cdot 10^{-9}$ mbar interconnected with an analysis chamber at base pressure $1 \cdot 10^{-10}$ mbar, as shown in Fig. 4.3. In the preparation chamber (Igel), a QCM is used for the measurement of the nominal mass thickness deposited on the substrate. The organic molecules are loaded in multiple organic evaporators mounted on the chamber. The Racoon chamber was used to anneal the graphene samples.

The electron analyser in the analysis chamber is located at an angle of 60° between the incident photon beam and the centre of the analysis chamber. The angle between the analyser and the sample surface normal could be adjusted by rotating the manipulator. This angle is reported as take-off or emission angle (α) between the sample surface normal and the analyser. Most of the spectra were collected at 0° take-off angle (i.e., normal emission geometry).

The spectra were collected in transmission mode and were angle-integrated over the acceptance angle of the analyser which was 10°. The SECO spectra were collected with the sample biased at $V_{bias} = -10$ V with respect to the electron analyser as to clear the analyser work function and allow for all the low kinetic energy inelastically scattered electrons to be
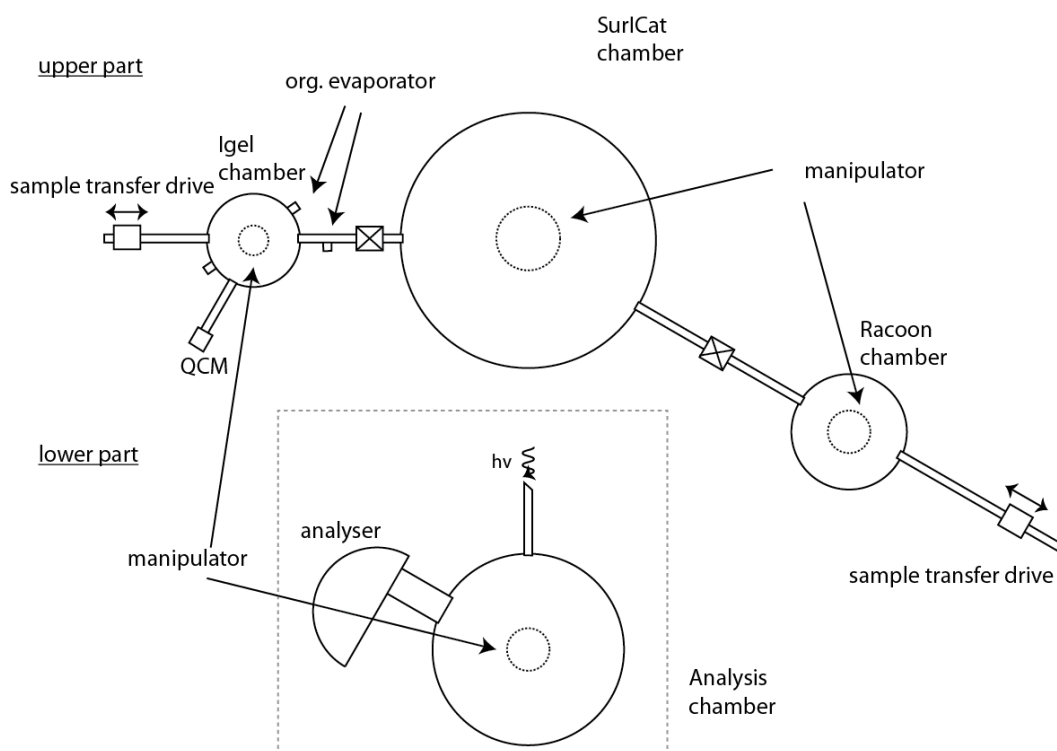
Figure 4.3: Schematic drawing of the experimental endstation SurICat at the synchrotron facility BESSY II, showing the apparatus used in this work. The analysis chamber is located at a level lower with respect to the preparation chambers.

collected.

The excitation energy chosen for the UPS experiments was 35 eV. For XPS, different energies were used, as to fix the photoelectron kinetic energy at ~ 100 eV, thus keeping the same inelastic mean free path for all the core levels recorded, at ~ 1 nm (see universal curve Fig. 3.2). The pass energy was set to 5 eV for measuring the SECO and 20 eV for valence- and core- levels, while a pass energy of 50 eV was used for collecting XPS surveys. The energy resolution was 150 meV for UPS and 300 meV for XPS.

4.2.3 Laboratory photoemission setup

Photoemission studies were also performed at Humboldt University in Berlin, using a commercial UHV system. The apparatus consists of a preparation chamber with base pressure $1 \cdot 10^{-9}$ mbar and analysis chamber with base pressure $1 \cdot 10^{-10}$ mbar. The preparation chamber was connected to a load-lock for fast sample entry without breaking vacuum con-

ditions. A schematic drawing of the experimental chambers is shown in Fig. 4.4.

The analysis chamber is equipped with a scanning tunnelling / atomic force microscope (VT-STM/AFM, Omicron), an X-ray gun (SPECS), a Helium discharge lamp (SPECS) and a hemispherical electron analyser (Phoibos 100, SPECS). For the collection of UPS and XPS spectra, a pass energy of 20 eV was used. XPS spectra were collected either with Mg Kα radiation ($h\nu$ = 1253.6 eV, natural linewidth 0.7 eV) or with Al Kα radiation ($h\nu$ = 1486.6 eV, natural linewidth 0.85 eV). The sampling area was $\sim$1 cm^2 for XPS and $\sim$ 0.5 cm^2 for UPS. For all UPS experiments, an aluminium filter was used in order to avoid photo-induced degradation of the organic films.
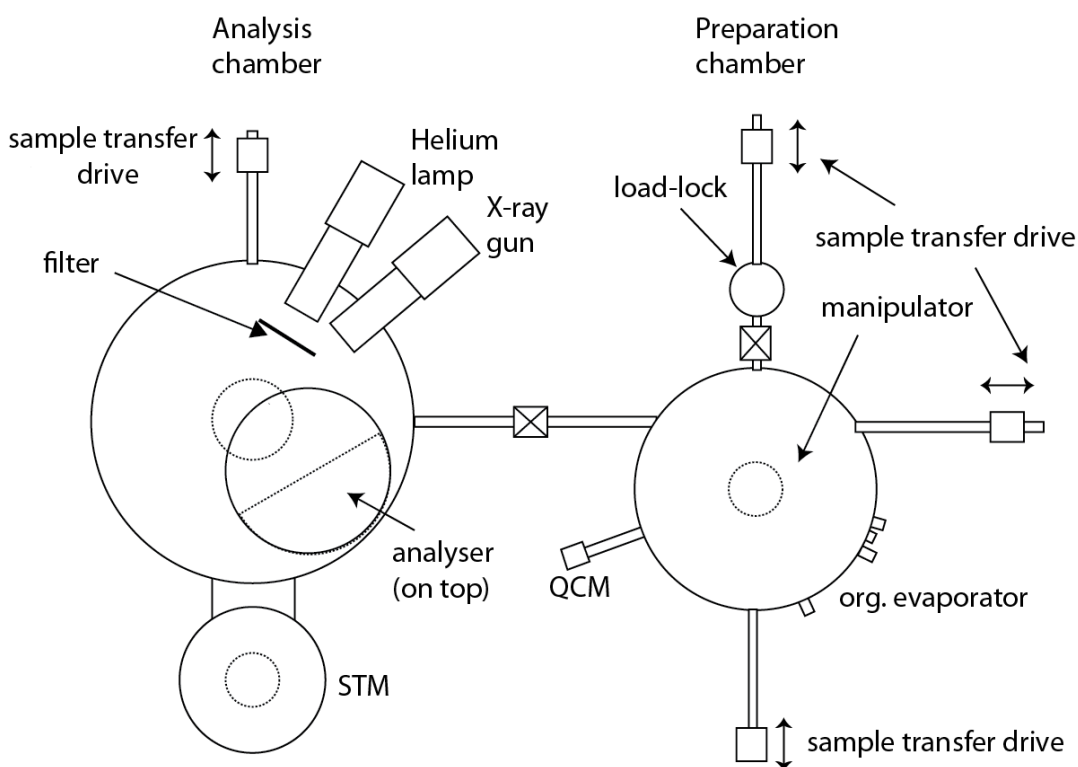

Figure 4.4: Schematic drawing of the experimental details of the commercial UHV system at Humboldt University in Berlin, showing the apparatus used for this work.

4.3   Data collection and analysis

Photoemission spectra

For analysing UPS and XPS spectra, the commercial programs OriginPro and IgorPro were used. To determine SECO in the low kinetic energy region of the UPS spectra, the intersection of linear extrapolations of the background and the cutoff was used, as shown in Fig. 4.5.
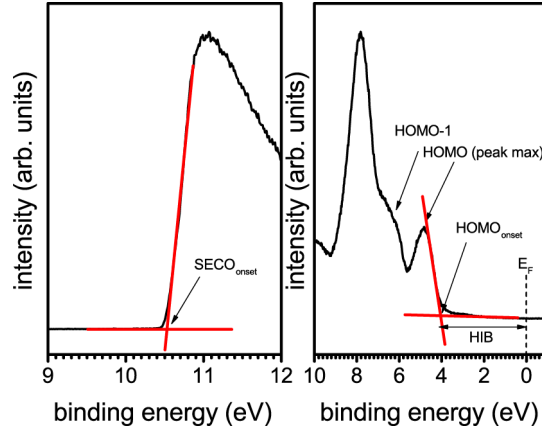
Figure 4.5: Fitting routine showing the determination of the onsets of the secondary electron cutoff ($SECO_{onset}$) and the highest occupied molecular orbital ($HOMO_{onset}$).The HOMO and HOMO-1 are also shown in the diagram.

To determine the Fermi level, a clean gold foil was used. The binding energies of the corresponding spectra were referred to this E_F as in this equation:

$$BE = E_{kin|E_F} - E_{kin} \qquad (4.1)$$

with E_{kin} the kinetic energy and $E_{kin|E_F}$ the kinetic energy of the Fermi level.

Similarly, the HOMO onset was also determined as intersection of two linear extrapolations, as shown in Fig. 4.5. The HOMO onset gives the value of the HIB. The IE is calculated using the following equation:

$$IE = h\nu - (E_{kin|HIB} - E_{kin|SECO} + eV_{bias}) \qquad (4.2)$$

with IE the ionization energy, $h\nu$ the excitation energy, $E_{kin|HIB}$ the kinetic energy of the hole injection barrier as determined by the HOMO onset,

$E_{kin|SECO}$ the kinetic energy SECO onset, e the electron charge and V_{bias} the bias voltage applied between the sample and the analyser.

When the experiments were performed using synchrotron radiation, for each core level measured, the energy of the photons was calibrated by measuring the BE of the Au 4f, from a gold foil attached to the manipulator. After the collection of every core level, the gold foil was measured with the same energy and the energy was calibrated, as depicted in Fig. 4.6. The resolution of the radiation was determined by the full width half maximum (ΔE_{XPS}) of the Au foil.
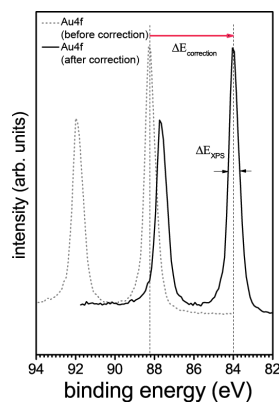
Figure 4.6: Au 4f core level of the Au foil, showing the calibration applied to the photon energy and the determination of the energy resolution of the incident light (ΔE_{XPS}).

Data fitting (Voigt peaks, Shirley or linear background) was performed with the freeware XPSPeak.

X-ray absorption spectra

There are various methods to probe the core level excitation event, which is the basis of X-ray absorption measurements. The transmission mode involves measurement of the X-ray intensity that passes through the sample,

$$I = I_0 e^{-\rho d} \tag{4.3}$$

with I_0 and I the incident and transmitted X-ray intensities, respectively, d the sample thickness and ρ the absorption coefficient (proportional to the absorption cross section). This method requires samples in the form of thin transparent foils, so that the X-ray can be effectively transmitted through

the sample. This limits its usage, in particular when organic molecules on a substrate are being studied.

Apart from the transmission mode, other methods for measuring NEX-AFS involve probing the decay channels of the core holes. After a core hole is created by X-ray absorption, electrons from a higher energy level relaxes into the energy level of that core hole. Simultaneously, this electron releases its energy either by emitting a fluorescent photon (radiative energy release) or by emitting an Auger electron (non-radiative energy release). These decay channels are directly related to the absorption cross-section. The fluorescence yield (FY) involves the detection of fluorescent photons by a photon detector and the probing depth is of the order of 100 nm. The Auger electron yield (AEY) involves the detection of the elastically scattered Auger electron intensity, using an electron analyser. The probing depth in this case is of the order of 1 nm. The total electron yield (TEY) involves the collection of emitted electrons of all kinetic energies. This signal is dominated by low kinetic energy inelastically scattered secondary electrons. The emitted electrons in TEY can be collected in two ways: (a) using an electron analyser or (b) measuring the sample drain current. With this mode, the probing depth is 5-10 nm. A variant of TEY is partial electron yield (PEY), where an electron analyser performs the electron detection and only electrons with energies exceeding a treshold are filtered out. The probing depth in this case is similar to AEY i.e., of the order of 1 nm. In this work, the TEY method was used and the drain current of the sample upon X-ray illumination was measured.

4.4   Theoretical simulations

Density-functional theory (DFT) is one of the most successful approaches to simulating matter using quantum mechanics. It is being routinely used for calculating properties of molecules, solids and atoms, e.g., the binding energies of molecules or the band structures of solids.

The versatility of DFT as a tool for performing simulations, is due to the fact that it makes the particle density n($\mathbf{r}$) of the system, the key variable that describes it. This realisation came by Hohenberg and Kohn, that postulated that the ground state of the ground state electron density of a system contains all the information of the many-body electronic wave-

function [135] Knowledge of n($\mathbf{r}$), implies the knowledge of the wavefunction and the potential and hence all the other observables of the system. Consequently, a many-body problem can be mapped onto a single-body problem, thus the size of the problem is reduced significantly.

XPS spectra were calculated with the DSCF method and the aug-cc-pVDZ basis set [136] on the free HATCN molecule using Dalton2011 [137]. The simulations were performed by Angelos Gianakopoulos at Uni. Mons, Belgium.

NEXAFS simulations were performed using the DFT code STOBE using the gradient corrected RPBE exchange-correlation functional [138, 139]. The simulations were performed by Prof. L. Pasquali at the University of Modena.

Further theoretical calculations were carried out with the Vienna Ab initio Simulation Package (VASP) [140–142] using the PerdewBurkeErnzerhof (PBE)[138] exchange-correlation functional and a plane-wave basis set with an energy cutoff of 400 eV. Grimme-type (DFT-D) dispersion corrections were applied [143], since van der Waals interactions play a significant role in noncovalent functionalization. In all calculations, the whole system (graphene and molecule) was optimized until the remaining atomic forces were smaller than 0.02 eV/Å. All the 3D isodensity representations in this work were produced by XCrysDen [144]. The simulations were performed by A. Giannakopoulos at University of Mons.

5 Results and discussion

The chapter begins with the characterisation of the as-received single layer graphene-on-quartz and graphene-on-copper and proceeds with the presentation of the procedure used to clean the samples in UHV. The chapter is then separated into three sections, which correspond to the three systems studied: (a) the molecular acceptor HATCN deposited on G/Qu, G/Cu and HOPG, (b) the molecular acceptor F_6TCNNQ deposited on G/Qu and G/Cu and (c) the molecular donors [RhCp*Cp]$_2$ and [RuCp*mes]$_2$ on G/Qu.

5.1   Cleaning procedure of graphene samples

The single layer graphene samples used in this work were produced in Max Planck Institute for Polymer Science, Mainz, Germany, by the CVD procedure on copper foil and were subsequently transferred onto the desired substrate using a wet chemical technique. For the purpose of this work, quartz was mainly used as a support of the graphene film. Since the CVD production of graphene is a relatively new method and the quality of the graphene can be dependent on the fabrication laboratory, a thorough photoemission characterisation of the sample was performed.

This section begins with an overview of the fabrication of CVD graphene-on-quartz by our collaborators and continues with the the subsequent in-house annealing treatment of the as-received G/Qu, which is proven to be a crucial step to recover a clean graphene layer. The final sample used throughout this work was the graphene-on-quartz sample after the in-house annealing treatment. The purity of the graphene layer as probed by XPS and UPS before and after the annealing treatment in UHV will be discussed and representative spectra will be presented and described.

5.1.1   Annealing of as-received graphene in UHV

An overview of the procedure leading to the as-received sample is shown
in Fig. 5.1. It is presented here, in order to underline the necessity of fur-
ther cleaning of the graphene sample after being prepared by our collab-
orators. In step (a), a mixture of methane and hydrogen gases flow in the
preparation chamber, while keeping a polycrystalline copper foil of thick-
ness 25 μm at 1020°C, for 1 hour. At the end of this procedure, both sides of
the copper foil are covered by predominantly single layer graphene [20].

   To enable the transfer of the CVD graphene sheets onto the desired sub-
strate, the top graphene layer is then covered by the protective polymethyl-
acrylate (PMMA) support [7, 21, 39]. Finally, the graphene sheet formed
on the bottom part of the copper foil is removed by plasma etching.
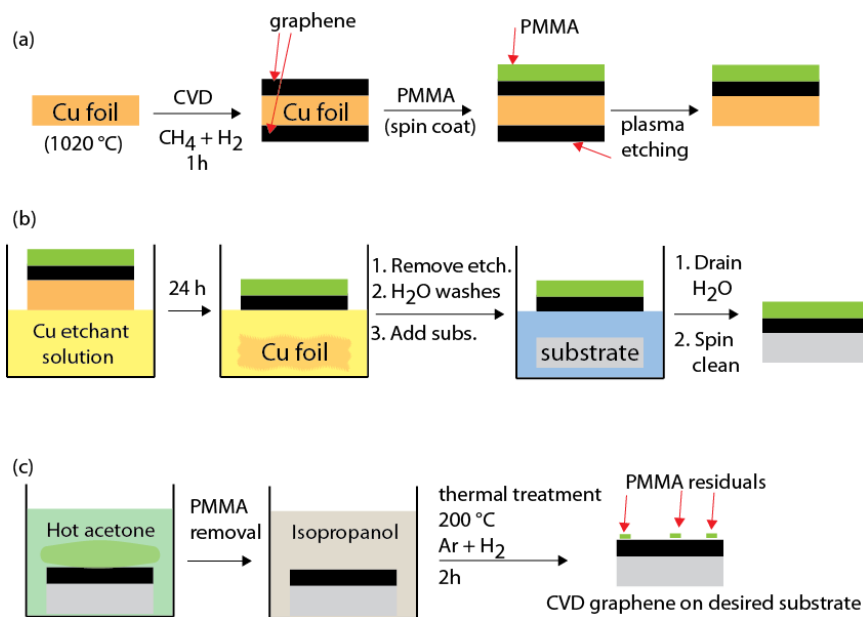
Figure 5.1: Schematic representation of the process of graphene fabricated by
chemical vapour deposition, the transfer to the desired substrate and the re-
moval of the polymethyl-acrylate (PMMA) polymer that supports and protects
the graphene layer from subsequent steps in the process.

   In step (b), the PMMA/G/Cu sample is immersed in an acidic solu-
tion for 24 hours in order to etch the Cu foil away. After 24 hours, the
etchant solution is drained out followed by 3-4 cycles of water washing
leaving behind the free-standing PMMA/graphene membrane that can be
easily handled. Subsequently, the PMMA/graphene membrane is man-

ually placed on the desired substrate. To reduce the amount of water molecules trapped between the graphene/substrate interface, the resulting PMMA/graphene/substrate is spin-cleaned. One has to note, that even after the spin cleaning, studies support that water molecules are trapped between the graphene layer and the graphene support and can not be removed entirely [145, 146]. In step (c), the PMMA is removed from the graphene/substrate by first immersing the sample in hot acetone and isopropanol and afterwards by thermally annealing it at 200°C in Ar/H_2 atmosphere for 2 hours. Finally, CVD graphenes on desired substrates are produced that preserve their continuity to a very high extent. The graphene films are strongly attached to substrates of virtually any material via van der Waals interactions. Note that, even after the extensive cleaning treatment to remove PMMA from the top of the graphene layer, the surface of the graphene layer still contains a substantial amount of PMMA [21, 39, 147].

The additional step employed in order to improve the purity of the graphene surface before depositing the COM on top is presented in the following. The method followed was prolonged thermal annealing of the samples at 550 °C in UHV (base pressure $< 10^{-9}$ mbar).
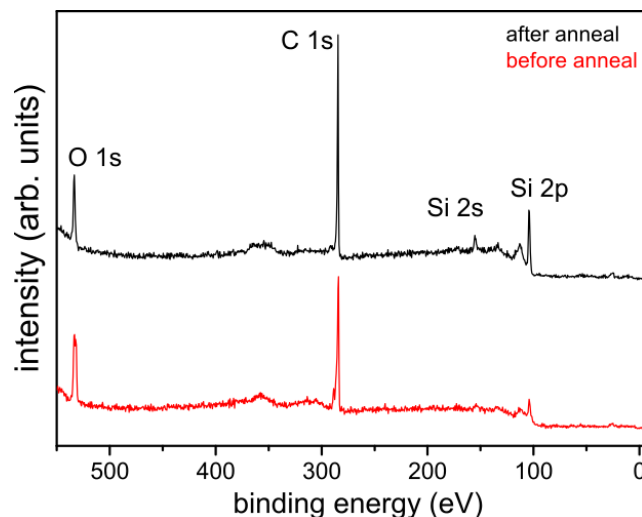

Figure 5.2: XPS survey spectra of graphene before and after annealing in UHV.

The in-situ cleaning in UHV and the immediate deposition of the COM is a practical and crucial method for fabricating the graphene/COM interface without exposing the graphene sample in ambient conditions. Thus,

the surface purity was probed in-situ, by investigating the emissions that appear in the C 1s and O 1s core level spectra, together with the valence level spectra. Fig. 5.2 shows the XPS survey spectra of the CVD graphene-on-quartz samples before and after annealing in UHV. Very importantly, the only elements that are observed in the spectra are O, C and Si. Fe and Cl that are present in $FeCl_3$, which is the etching agent for the Cu foil are not present in the spectra, suggesting that the graphene/substrate is not contaminated by the etchant. The absence of these features is critical, since any contamination from $FeCl_3$ would effectively dope the graphene [148]. Another significant feature contained in the survey spectra is that after annealing, the emission intensity from Si, coming from quartz, increases. This is explained by assuming that PMMA desorbs from the top of graphene as a result of the thermal annealing. This causes an increased intensity of photoelectrons stemming from quartz. Since the PMMA on top of the graphene sheet is reduced, more photoelectrons can escape from deeper layers in the sample and reach the electron analyser, enhancing the substrate-related emissions.

C 1s core level spectra were measured for the as-received graphene-on-quartz (G/Qu'), the G/Cu and the annealed G/Qu samples. Fig. 5.3 (a) shows three corresponding representative spectra.

After the wet chemical transfer using PMMA, G/Qu shows various emission features in the C 1s core level spectrum in the region from BE = 287 eV to BE = 289 eV, which are attributed to residual PMMA [147, 149] that remained on the graphene layer after the cleaning treatment performed using hot acetone and thermal annealing at 200°. After the annealing treatment performed in UHV, these emissions are singificantly damped and the chemical integrity of graphene is confirmed by comparing the C 1s core level spectra of G/Qu and G/Cu in Fig. 5.3. The shift in the binding energy of the peak maximum between G/Cu (284.2 eV) and G/Qu ($\sim$ 284.6 eV) is due to PMMA being a cause of a slight p-doping of the graphene layer [150, 151]. After annealing, the C 1s core level peak maximum of G/Qu is at $\sim$ 284.4 eV, as a high amount of PMMA leaves the sample surface. The additional $\Delta E = 0.2$ eV energy difference with respect to the case of G/Cu is attributed to the different electronic coupling of graphene with copper and quartz substrates [149].
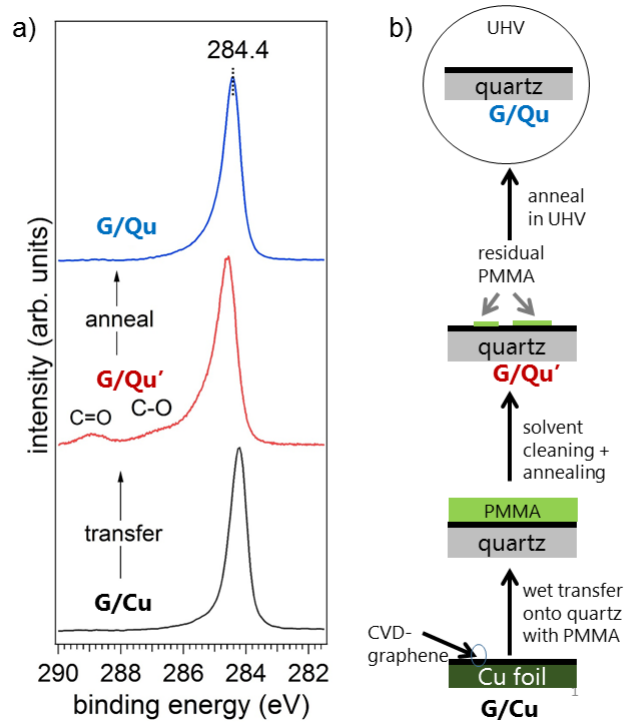
Figure 5.3: (a) C 1s core level spectra of graphene-on-copper (G/Cu - black), of graphene-on-quartz before annealing (G/Qu', red colour) and of graphene-on-quartz after annealing in UHV (G/Qu, blue colour). (b) Steps of graphene treatment in UHV to get from G/Cu to a clean G/Qu in UHV.

Quantitative C 1s core level analysis

Fig. 5.4a shows the C 1s spectrum of the cleaned G/Cu sample. The peak was fitted by a single asymmetric Voigt profile, resembling the Doniach-Sunjic function commonly used to deconvolute the emission profiles resulting from X-ray induced photoelectrons emerging from metals [152]. The FWHM used was 0.5 eV.

The C 1s core level of graphene has to be fitted with an asymmetry in the higher binding energy, since photoelectrons from the core levels are interacting with the delocalised cloud of electrons present in the valence band and thus lose some of their kinetic energy in their way out, giving the asymmetric lineshape. [147, 152].

Fig. 5.4b shows the C 1s core level spectrum of the as-received G/Qu together with the repeating unit of PMMA in the inlet. Five components were needed to reliably deconvolute the spectrum and are explained in the following. The C 1s core level emission stemming from sp^2 hybridised
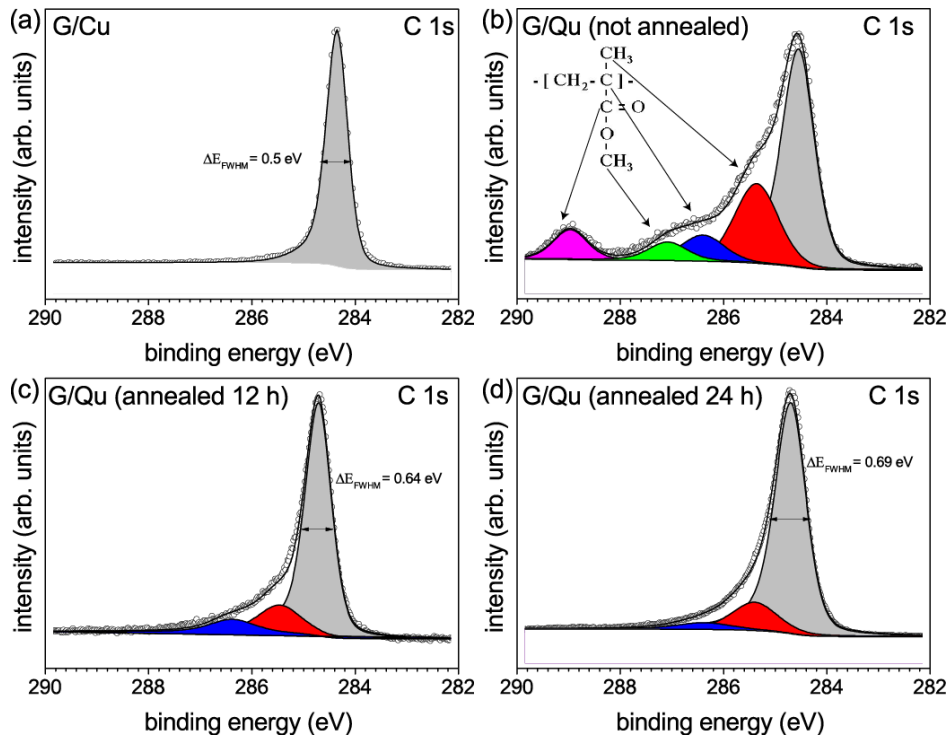
Figure 5.4: C 1s spectra of a) as-received graphene on polycrystalline copper foil, b) as received graphene-on-quartz, c) graphene-on-quartz annealed for 12 hours, d) graphene-on-quartz annealed for 24 hours. The inlet in b) shows the monomer of PMMA.

carbon atoms in the graphene layer is located at BE = 284.4 eV [147] (grey colour). This peak was constrained to the same Voigt function parameters as the C 1s core level in G/Cu, but with a higher FWHM = (0.65-0.7) eV. The C 1s core level emission with peak maximum at BE = 285.4 eV (red colour) is attributed to sp^3 hybridised C-C at, that can be contained in the PMMA. Emissions from ambient contamination are located at this BE, so the unambiguous assignment of this peak is not possible. At BE = 286.4 eV there are also emissions attributed to sp^3 hybridised carbon atoms, that are shown in the inlet containing the PMMA structure in Fig. 5.4b. As before, emissions from contaminants from ambient can be situated at this BE. At BE = 287.1 eV (green colour) emissions from the carbon on the C-O group in PMMA are located and at BE = 289 eV, (purple colour) there are the emissions from the carbon on the O-C=O group.

By measuring the area of each deconvoluted peak, it is found that ca. 44 % of the graphene surface is covered with the PMMA prior to the an-

nealing treatment in UHV. Fig. 5.4c shows the C 1s core level of G/Qu after annealed in UHV for 12 hours. After the annealing procedure, the emissions stemming from PMMA result to 22 %.

Annealing of the G/Qu samples up to 24 hours, results to even further reduction of the PMMA. Fig. 5.4d shows the deconvolution of the C 1s core level of G/Qu annealed for 24 hours. In this case, the PMMA emissions are 17 %. Despite the prolonged annealing in UHV, the sp^3 type carbon contaminations are never completely eliminated from the surface of graphene. This results since some of the contaminants can be trapped on specific sites in graphene, such as defects, or at the boundaries between the different two-dimensional crystallites that are a result of the nucleation in the CVD process [149]. In addition, these contaminants could be also located between the graphene and substrate (quartz). In this case, these contaminants are well trapped under the graphene layer with low probability of being removed [149].

C 1s core level emissions quantification						
Sample	G	=CH2 =CH3	>C=	-C-O	O-C=O	Total contam.
G/Qu as-received	0.56	0.23	0.08	0.05	0.08	0.44
G/Qu annealed 12h	0.78	0.15	0.07	0	0	0.22
G/Qu annealed 24h	0.83	0.13	0.04	0	0	0.17

Table 5.1: Fractions of distinguishable chemical species obtained from the deconvolution of the C 1s core level emission of graphene-on-quartz (G/Qu).

The quantification of the emissions stemming from graphene and from contaminations are summarised in table 5.1. A surface with contamination as low as 17 % could serve as a virtually clean surface to form the hybrid structure using organic molecules.

Fig. 5.5 shows the O 1s core level spectra of the G/Qu substrate before annealing in UHV for 24 hours (black spectrum) and after annealing (red spectrum). The spectrum contains emissions from the underlying quartz [147, 153], PMMA [154] or water trapped between graphene and the substrate [145, 146]. The spectra are difficult to deconvolve unambiguously, however, two features are clearly distinguished. Before the anneal-

ing treatment, the feature at BE = 534 eV is attributed to emissions from the oxygen coming from SiO_2 in the underlying quartz support [153], water trapped between graphene and support [155], and PMMA [154]. Combining these results with the C 1s core level spectra, the feature at BE = 532.3 eV is attributed to PMMA, since, after annealing, this emission disappears, confirming the absence of C=O or C-O groups from the surface.
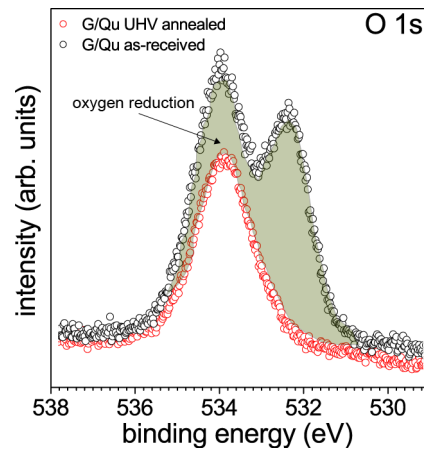
Figure 5.5: Representative O 1s core level spectra of graphene-on-quartz before and after annealing for 24 hours at 500° C.

Valence level analysis

SECO and valence level spectra of G/Qu before and after annealing were recorded using UPS. Fig. 5.6a shows that the work function of the PMMA-contaminated G/Qu is at 3.85 eV and only after the UHV annealing recovers the value of 4.45 eV, which corresponds to the work function of graphene [156, 157]. Fig. 5.6b shows that, the as-received sample shows a valence electronic structure governed by emissions stemming from the PMMA [158]. After annealing, the valence electronic signature of graphene is clear in the spectra [156]. The emissions with peak maxima at ~ 3.2 eV (labeled I in Fig. 5.6), ~ 6.3 eV (labeled II in Fig. 5.6) and ~ 8 eV (labeled III in Fig. 5.6) are attributed to the π band, the crossing between σ and π bands and σ band respectively. This provides further evidence that the as-received sample has the majority of the surface still covered with the spin-coated PMMA and proves the necessity of prolonged annealing of the graphene sheet in order to get sufficiently clean again.
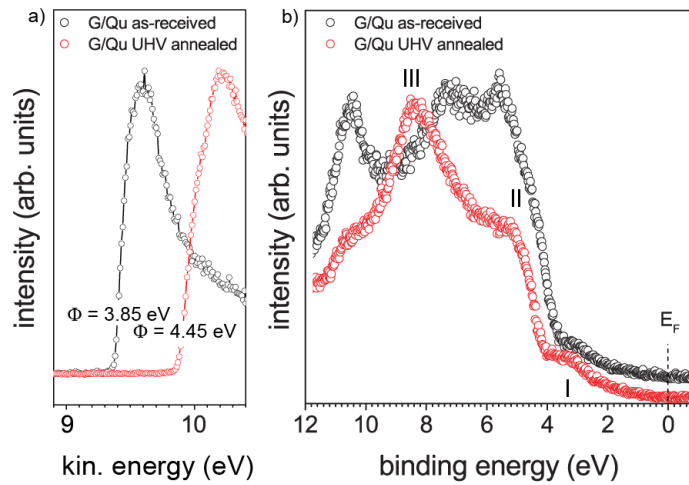
Figure 5.6: Representative a) SECO spectra and b) valence level spectra of graphene-on-quartz before and after annealing in ultrahigh vacuum.

5.1.2 Conclusion

In this section, the procedure for preparing the as-received CVD graphene-on-quartz was discussed, together with the characterisation of the as-received and the UHV annealed samples. The UHV annealing results in a significant reduction of the contamination on top of the graphene, as evidenced by XPS and UPS measurements. Thus, it was confirmed that the graphene could serve as a sufficiently clean surface to be used for the adsorption of a subsequent organic semiconductor and to study the electronic and structural properties of the interface formed.

5.2 Functionalisation of graphene with HATCN

The molecular acceptor HATCN has been found to exhibit a transition between lying and vertically inclined monolayer on Ag(111) and Au(111), depending on the molecular density in the monolayer. It was successfully used e.g., as a HIB tuner [88, 120], as a "decoupling" interlayer between Ag(111) and C_{60} molecules [121], as an electron acceptor on $Alq3_3$ precovered Ag(111) [89] and as a work function tuner for indium tin oxide (ITO) [64]. The main characteristic of this electron acceptor is its highly electron deficient molecular core that causes it to avoid π stacking [131].

The molecular orientation and electronic structure of HATCN on G/Qu were studied in detail using XPS, UPS and NEXAFS. The results for the HATCN/G/Qu system were supported and were consistent with DFT calculations from our collaborators. The molecular acceptor was deposited as well on G/Cu, in order to compare the electronic structure of these systems with G/Qu. In addition, an analysis about the occurrence of push-back related phenomena on graphene/graphitic substrates was performed.

5.2.1 Electronic properties of HATCN on graphene-on-quartz

Valence electronic structure

Fig. 5.7a,b depict the SECO and valence region spectra (recorded in normal emission), of increasing nominal thickness (θ) of HATCN adsorbed on graphene-on-quartz.

The work function of pristine graphene-on-quartz is 4.5 eV and increases incrementally by a total of $\Delta\Phi = 1.2$ eV upon sequential deposition of HATCN, saturating at a value of $\Phi = 5.2$ eV. Fig. 5.7c is a plot of the Φ against nominal mass thickness of HATCN (θ) deposited on G/Qu. The plot clearly shows an abrupt linear increase of the work function by 0.4 eV up to a $\theta = 2$ nm, amounting to a work function of 4.9 eV. After ca. 2 nm, the work function continues to increase sub-linearly, until it saturates at $\Phi = 5.7$ eV at ca. 12 nm nominal thickness. From the profile of the work function evolution, the growth mode points towards very late filling of the first monolayer of HATCN on graphene, since the saturation of the work function happens at a coverage of $\theta \sim 12$ nm.
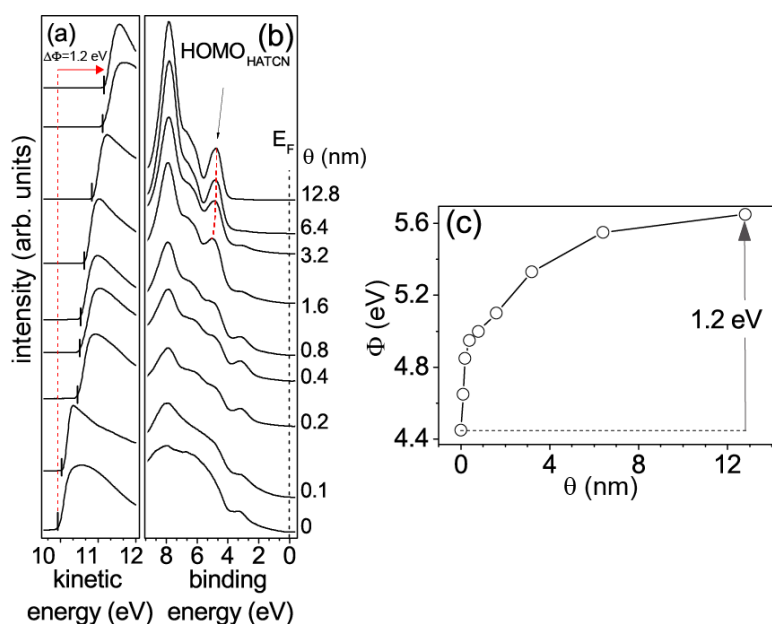
Figure 5.7: a) SECO evolution and b) Valence band evolution upon HATCN deposition on graphene-on-quartz (G/Qu), c) Work function change (Φ) vs. HATCN nominal thickness (θ).

The valence level spectra correspond, from bottom to top, to pristine graphene-on-quartz and the subsequent HATCN thickness-dependent series up to nominally 12.8 nm of HATCN. With increasing nominal thickness of HATCN, the emissions stemming from graphene get damped very slowly. At $\theta = 0.2$ nm, the molecular features start to get identifiable, however, only at $\theta = 1.6$ nm the HOMO of HATCN forms a clear distinguishable peak in the spectra. At this nominal thickness, the HOMO onset and HOMO peak maximum are located at BE = 4 eV and BE = 5 eV respectively. The HOMO peak maximum then shifts by a total of 0.2 eV and is located at BE = 4.8 eV. This shift can not be attributed to insufficient photohole screening in the bulk, as in that case, the HOMO peak maximum would shift to a higher BE. As it was previously reported, especially for HATCN adsorbed on Ag(111), HATCN adopts a flat-lying orientation for the initial coverages and a density-dependent re-orientation occurs for higher coverages [88, 120, 159]. Thus the shift in the HOMO peak maximum is attributed to the existence of different molecular orientations between high and low coverages [160].

Given the large work function increase, one would expect CT-related

features arising due to CT between the molecule and G/Qu. This does not occur, and can be corroborated by hypothesizing that only a small fraction of the HATCN layer in contact with graphene needs to be in an anionic state in order to establish thermodynamic equilibrium. Thus, emissions from the LUMO-derived state, which can be present only in the first monolayer, are masked by photoelectron signals stemming from graphene and neutral molecules. Hence, this feature is not experimentally accessible. According to ref. [161], that performed a simulation of HATCN on the exact system that was studied in this work, the LUMO of HATCN turns out to be pinned around E_F.

Core electronic structure

In Fig. 5.8a the spectra show the evolution of C 1s core level emissions upon incremental deposition of HATCN on G/Qu. The spectral evolution shows an increasing intensity of HATCN-related emission features, with peak maximum at BE = 287.1 eV and an attenuation of emission from graphene at BE = 284.4 eV with increasing molecular coverage. The presence of graphene features at HATCN coverages as high as θ = 12.8 nm readily evidences pronounced island growth of the molecule, since the electron escape depth with the photon energy used (hv = 390 eV), is ~ 1 nm [111]. Fig. 5.8b shows the C 1s core level emission at the highest HATCN coverage of θ = 12 nm. The chemical structure of HATCN, highlighting the carbon atoms in different chemical environment, i.e., carbon atoms in CN groups (red) and carbon atoms in heterocycle (blue) are depicted in Fig. 5.8c. The deconvolution shows a 1:2 ratio of carbon atoms on cyano-groups (red) to carbons on heterocycles (blue), as expected from the chemical structure of HATCN. The emissions at higher BE are attributed to shake-ups from the molecule.

Fig. 5.9a presents the N 1s core level spectrum with a zoom at the low BE region (Fig. 5.9b) together with the chemical structure of HATCN, highlighting the different chemical environments for nitrogen in the cyanogroups (blue) and nitrogen in the heterocycles (red) in Fig. 5.9c.

The N 1s core level emission maximum is located at BE = 400.3 eV. In addition to this emission, which is attributed to the neutral HATCN another low intensity emission is observed at BE = 399 eV. The presence of the feature at the low BE side of the main feature is attributed to charge
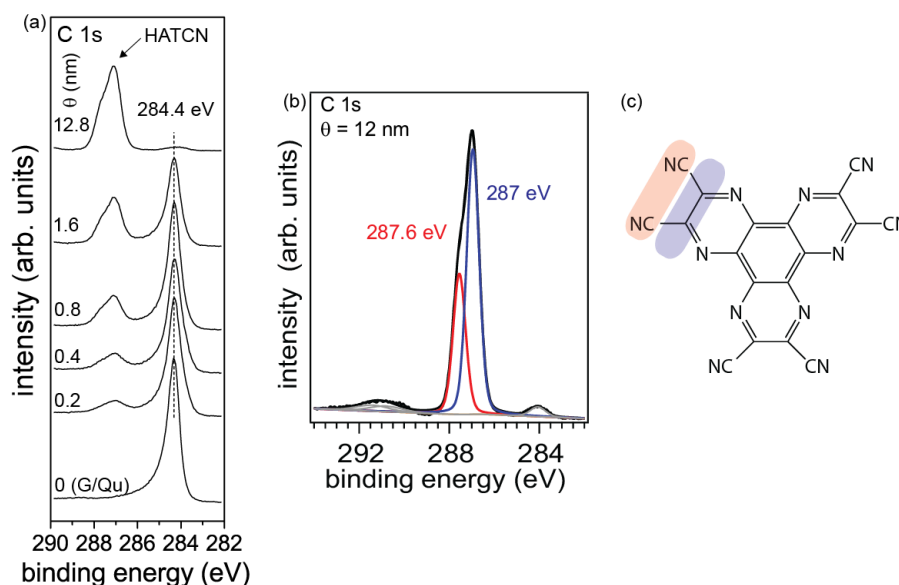
Figure 5.8: (a) Evolution of C1s upon HATCN deposition. (b) Deconvolution of the C 1s core level at coverage (θ) = 12 nm, showing the carbon atoms in the cyanogroups (red) and on the heterocycle (blue). (c) Chemical structure of HATCN, highlighting the carbon atoms in different chemical environment with red (cyanogroups) and blue (heterocycles).

transfer occurring at the interface, i.e., negative charge being transferred from graphene to HATCN. By deconvoluting the N 1s core level spectra for bulk coverage HATCN, the contributions of nitrogen atoms in the heterocycle (N_{in}) and those in the peripheral CN groups (N_{out}) can be clearly distinguished; these two are separated by an energy difference (ΔE) of 0.5 eV and are located at BE = 400.5 eV and BE = 400 eV, respectively.

Deconvolution of the interface feature due to CT, representing the negatively charged molecules was performed using a fitting routine with two components of identical intensity and FWHM and a constraint for the energy difference between them $\Delta E = 0.5$ eV, as for the neutral HATCN. The fitting uncovers two new states at BE = 399 eV and BE = 398.5 eV and yields a peak-area percentage of $(10 \pm 1)\%$ at 0.1 nm and 0.2 nm nominal coverage, $(7 \pm 1)\%$ at 0.4 nm, and $(5 \pm 1)\%$ at 0.8 nm coverage (Fig. 5.9b, insets) for the negatively charged HATCN species compared to the neutral one. The low-BE emission is damped and eventually quenched for $\theta \geq 1.6$ nm by emissions from the neutral HATCN molecules adsorbed on top of the first monolayer. The quenching of this emission at higher coverages verifies that it is indeed an interface feature resulting from electron transfer
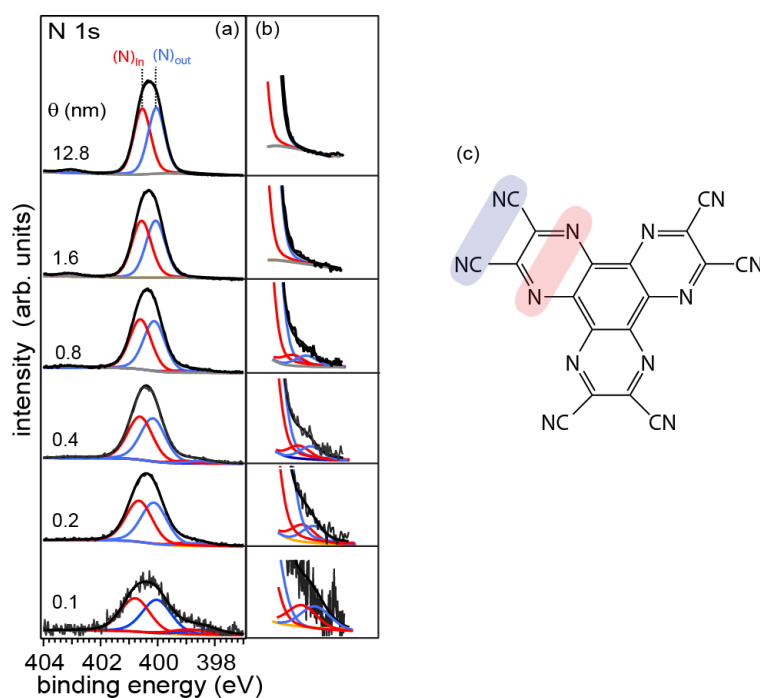
Figure 5.9: a) Deconvolution of the N 1s emissions from HATCN with (b) zoom at the low binding energy region. c) Chemical structure of HATCN, with the nitrogens in different chemical environments highlighted with blue for cyanogroups and red for heterocycle.

from graphene to the molecules in direct contact with graphene.

Another interesting feature observed in the N 1s core level spectrum is the presence of neutral HATCN already at very low θ values, indicating that multilayer formation proceeds most likely already before the monolayer is completed (Volmer-Weber growth), in agreement with the work function evolution.

5.2.2 Electronic properties of HATCN on graphene-on-copper

Valence electronic structure

In Fig. 5.10 the evolution of the SECO (a) and the valence electronic structure (b) upon deposition of HATCN on G/Cu is presented. A similar sub-linear evolution of the work function is observed, as shown in Fig. 5.10c) indicating that the growth proceeds in a very similar way as the HATCN/G/Qu system, as discussed above. The initial Φ of G/Cu is 4.3 eV. At bulk HATCN coverage, Φ saturates at 5.3 eV, presenting a

$\Delta\Phi$ of 1 eV. The valence electronic structure is a convolution of features arising graphene and Cu. The emission with peak maximum at 1.5 eV and onset at 0.8 eV in the low binding energy region, close to E_F stems from oxidized Cu [162]. The π band emission from graphene is clearly evident at BE = 3 eV (peak maximum) and disappears at bulk HATCN coverage.

Very interestingly, and in contrast to previous studies of HATCN deposited on Cu(111)[163], no interface features were observed near the Fermi level, in a very similar fashion to the HATCN/G/Qu system. In that study, the rather strong interaction between HATCN and Cu(111), induces the chemisorption of the molecular acceptor on the metal. This is manifested in the UPS spectra as an additional emission feature cutting E_F. This feature is the former LUMO of the neutral molecule, that gets partially populated upon adsorption on the metal. The absence of similar features for HATCN adsorbed on G/Cu, suggests that the graphene sheet acts as a decoupling layer, preventing the metallic orbitals to hybridise with the molecular ones. In the case of G/Qu, the resulting interaction is a weak physisorption of the molecule on graphene, with a low amount of charge being transferred to the LUMO of the molecule. The absence of observable emissions near the Fermi level indicates that the concentration of charged molecules is very low to be detected by UPS, as observed for HATCN/G/Qu, and as it will be explained in the following section.
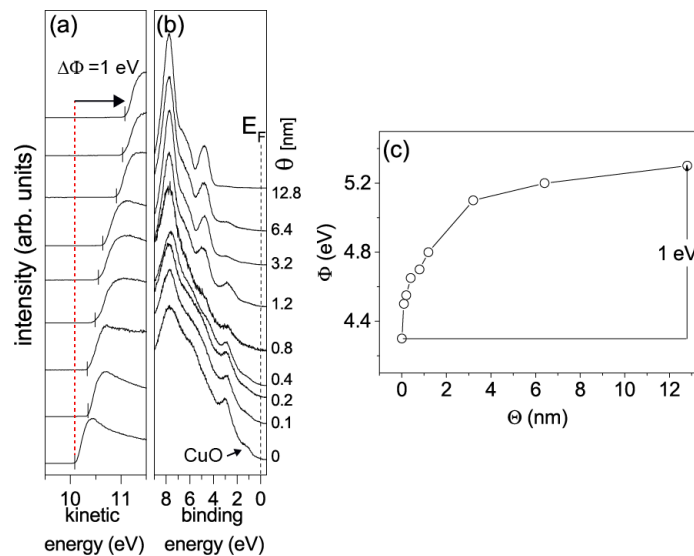

Figure 5.10: a) SECO evolution and b) Valence band evolution upon HATCN deposition. c) Work function change (Φ) vs. HATCN nominal thickness (θ).

Core electronic structure

Fig. 5.11a shows the evolution of the C 1s core level emission region upon incremental deposition of HATCN on graphene-on-copper. In a very similar fashion as with the HATCN/G/Qu system, the C 1s emission from graphene is reduced in intensity and at the same time the features arising from the HATCN C 1s increase in intensity. Despite the fact that graphene-on-copper is in principle much flatter and uniform than graphene transferred on other substrates[147], the growth mode proceeds in a very similar fashion, since graphene features are presented up to the bulk HATCN coverage (θ = 12.8 nm). This provides evidence that the growth mode is not dependent on possible corrugation or contamination of graphene due to any residual polymer residing on top, but it is a result of graphene/molecule and molecule/molecule interactions.

The N 1s core level emissions were also fitted and shown in Fig. 5.11b, in a procedure similar to what was used for the N 1s of HATCN/G/Qu. The two emissions stemming from the cyano-groups, N_{out} (blue) and heterocycles, N_{in} are shown. They appear at the same binding energies of 400.5 eV (N 1s in heterocycles) and 400 eV (N 1s in cyano-groups). The deconvolution contains the two additional features arising from the electron-enriched HATCN species at lower binding energy, with $\sim$ 10 % emission intensity, compared to the entire peak, very similar to the
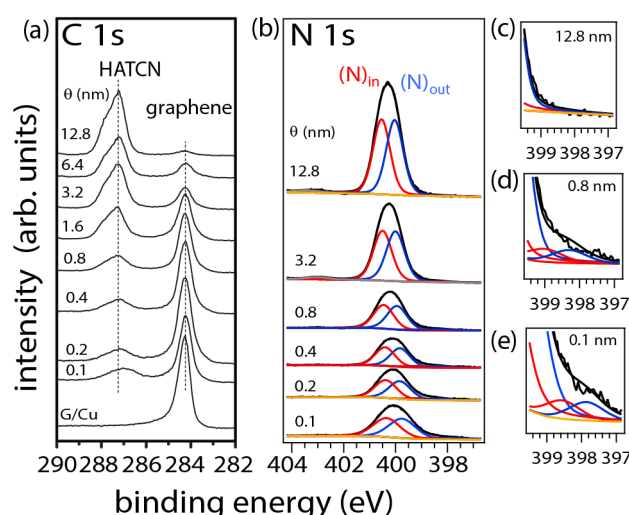

Figure 5.11: Evolution of C 1s emission region upon HATCN deposition

HATCN/G/Qu case. The emissions stemming from the charged HATCN species are shown in Fig. 5.11c-e, for nominal thicknesses of 0.1 nm, 0.8 nm and 12.8 nm. The low amount of charged species in the monolayer, can now explain, very similar to the HATCN/G/Qu system, the absence of emissions resulting from the populated LUMO of the molecule in the UPS spectra.

5.2.3   Push-back effect on graphitic surfaces

Previous studies have reported an initial decrease of the work function of the substrate upon (sub-)monolayer HATCN adsorption, on metals, e.g., atomically clean Ag(111) or Au(111) [88, 89, 121], as well as metal oxides, e.g., indium tin oxide (ITO) [64, 78]. The initial decrease of the work function was attributed to push-back effect. This occurs, due to the excess electronic distribution spilling out of the surfaces of these systems. After they are interfaced with another material - organic molecules in this case - the spilled-out electrons are forced to (partially) reenter into the bulk due to the Pauli exclusion princile, inducing a change of the surface dipole [61, 74, 80]. For the case of graphene-on-quartz and graphene-on-copper, no similar decrease in the work function was observed upon (sub-)monolayer coverage of HATCN. The absence of push-back on graphene can be attributed to two reasons: a) the graphene-on-quartz is not atomically clean, since PMMA residues can still be located on the surface, even after the prolonged high temperature annealing in UHV. Thus, the push-back effect would already occur by the PMMA remnants on the surface and b) due to the linear band dispersion of graphene, the density of states at the Fermi level vanishes (see Fundamental section). Thus, the resulting electronic cloud spilling out of graphene is negligible and produces no UPS-observable energy shifts.

It should be noted that previous studies invoking adsorption of organic molecules on graphene with a virtually atomically clean surface, e.g., for graphene thermally grown on 6H-SiC(0001) [100] or for graphene synthesised by the CVD process on n-doped 4H-SiC(0001) [164] did not report an observable push-back effect as well.

In order to study any push-back related phenomenon, HATCN the work function evolution is monitored for G/Cu and G/Qu and the molec-

ular acceptor was deposited on HOPG as well. The work function vs the nominal thickness is plotted in Fig. 5.12. For all of these graphitic surfaces, no push back effect was observed with UPS. The absence of any detectable push-back also on HOPG thus, very likely does not stem due to PMMA remnants on the surface, but instead, it originates from the lower free valence electron density of these graphitic systems than metals or metal oxides.
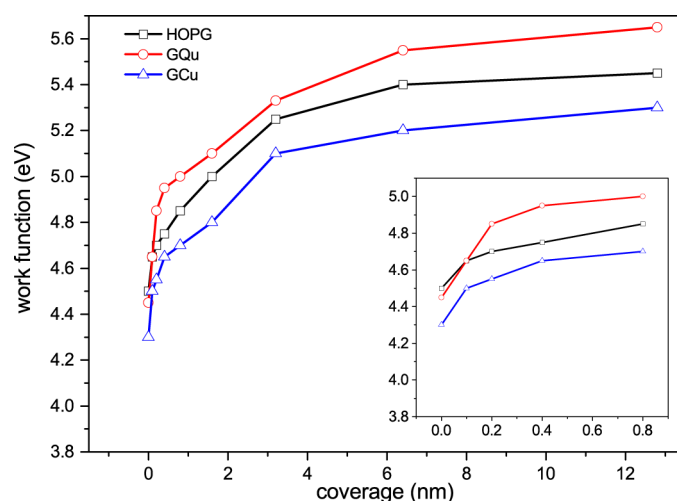
Figure 5.12: Work function evolution upon HATCN deposition on HOPG, graphene-on-quartz (GQu) and graphene-on-copper (GCu) up to a coverage of 12 nm HATCN. The inset shows a zoom for the evolution of the work function until 0.8 nm.

5.2.4 Molecular orientation

To obtain insight into the molecular orientation of HATCN in the monolayer (deposited on graphene-on-quartz), NEXAFS was performed for θ = 0.3 nm (Fig. 5.13a) and θ= 1.2 nm (Fig. 5.13b). Since, from the XPS and UPS results, the growth seems to be dominated vastly by island growth, NEXAFS was selectively performed at sufficiently low coverages, as to ensure that the island formation is minimum and the coverage was still in the monolayer regime.

Fitting the intensity ratio of the two experimentally resolved peaks as a function of polarization incidence angle [119] for the two coverages investigated verifies the existence of two different orientations of the molecule

on the surface. For θ = 0.3 nm we find a fitted molecular inclination angle of ψ_{inc} = (10 ± 5)° with respect to the graphene surface, suggesting essentially flat-lying HATCN in the lowest coverage regime. For θ = 1.2 nm, the fitting yields an inclination angle of ψ_{inc} = (40 ± 5)°, indicating significantly vertically inclined HATCN molecules at that coverage.

At this point, it should be pointed out that since NEXAFS is an area-averaging technique, different orientations may actually coexist. Thus, one might speculate that molecules in the monolayer are flat-lying and that molecules only in the multilayer are vertically inclined. However, the data also allow an interpretation that includes a coverage-dependent (or molecular density-dependent) re-orientation of HATCN molecules from flat-lying to vertically inclined already in the monolayer, in analogy to what has been reported for the growth of HATCN on Ag(111) [120]. As it will be shown in detail in the theoretical section, the calculations favour this second growth model, based on total energy considerations.

The two different orientations in conjunction with the pronounced island growth account for the gradual decrease and eventual disappearance of the interface emission feature (assigned to the monolayer molecules with CT interaction with graphene) in the XPS spectra (Fig. 5.13c) for θ ≥ 1.6 nm. Bi- and multilayer formation sets in very early, with neutral HATCN located in upper layers, which attenuate the interface emission, since the electron escape depth is around $\sim$ 1 nm for the kinetic energies selected in this study [111].

5.2.5   Theoretical modelling

Modelling of N K-edge of free HATCN

In Fig. 5.14 the NEXAFS simulations were performed by our collaborators and are presented here. The simulations were performed for a free HATCN molecule to help identifying the two main components in the experimental spectra peaking at photon energy 400.9 eV and 402.2 eV, respectively. The lowest energy peak in the experimental spectra seems to involve two N 1s $\rightarrow \pi^*(p_z)$ transitions. These two transitions are not observed in the experimental spectra, since the experimental resolution convolutes these two peaks into a single one. The lowest-energy peak is localized on the nitrogens of the CN groups and the one at 0.2 eV higher energy
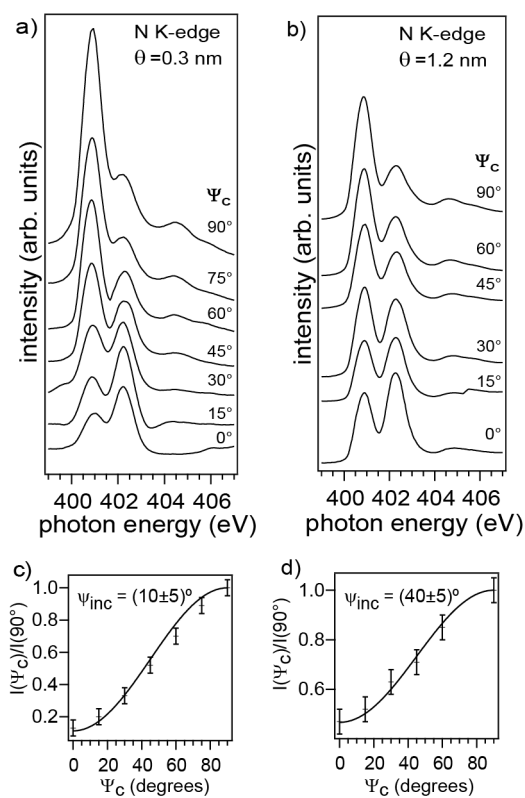
Figure 5.13: Series of NEXAFS spectra as a function of incidence angle Ψ_c from normal incidence (0°) to grazing incidence (90°) of the π^*-region at the N K-edge for a 0.3 nm (a) and a 1.2 nm (b) thick HATCN film grown on graphene-on-quartz. c) and d) are plots of the relative π^*-orbital intensities as a function of the photon incidence angle Ψ_c. The solid curve corresponds to the best fit of the intensity evolution of the molecule giving aromatic plane tilt angle of 10° (a) and 40° (b).

relates to the nitrogen atoms in the heterocycle. The transition at 402.2 eV corresponds to the N 1s $\rightarrow \pi^*(p_{xy})$ transition within the CN groups.
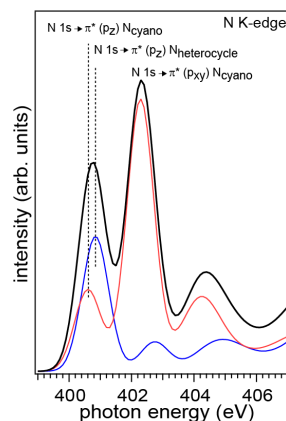
Figure 5.14: Calculated NEXAFS spectrum for free HATCN molecule showing the intensity distribution of the three dominant peaks.

Modelling of molecular orientation

To understand the effect of different molecular orientations with respect to the graphene surface on the electronic properties, DFT calculations were performed by our collaborators. In addition, these calculations also provide additional insight into the most plausible growth mode, as mentioned previously.

Starting from a flat-lying conformation, the angle between the HATCN plane and the plane of graphene was increased in steps of 20° until an edge-on conformation was reached (Fig. 5.15a). A large supercell was used in order to suppress interactions between neighboring molecules. In this case, the system is effectively in a low-density regime. For all orientations, a CT of 0.35 e-/molecule (0.14 e$^-$/nm^2) was found, resulting in a work function change ranging from $\Delta\Phi = 0.55$ eV (for 0°, i.e., flat-lying) up to $\Delta\Phi = 1.27$ eV (90°, i.e., edge-on), as shown in Fig. 5.15b.

Further investigations were performed with smaller supercells to include also intermolecular interactions between neighbouring molecules, i.e., effectively bringing the system into a "high-density" regime. In particular, four structures were studied, shown in Fig. 5.16: (a) flat-lying HATCN, (b) & (c) two HATCN dimers with different intermolecular displacements standing edge-on (90°), and (d) a HATCN dimer inclined 45°

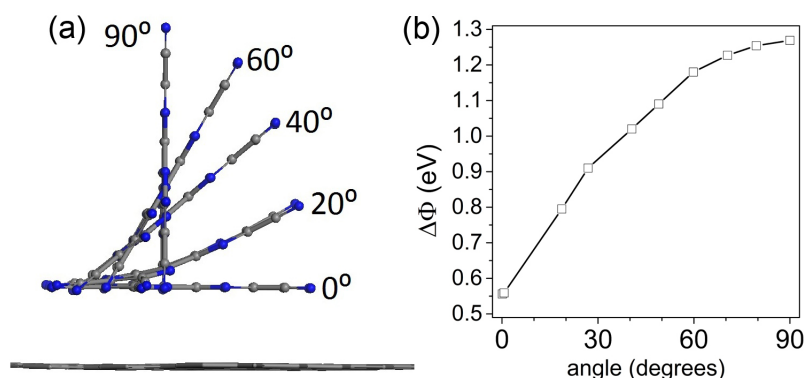Figure 5.15: Low-density case regime, showing (a) schematic representation of the relative orientation of HATCN molecules with respect to the graphene surface (b) calculated change in work function ($\Delta\Phi$) as a function of inclination angle.

with respect to the graphene plane. Adsorption energies, E_{ads}, per unit cell for monolayers of HATCN on graphene (thus encompassing both interactions with the graphene surface and among neighboring HATCN molecules) are shown in Fig. 5.16e. The results show that the flat-lying and edge-on configurations have similar adsorption energies of E_{ads} = -0.9 eV, while the 45° vertically inclined structure is much more stable with E_{ads} = -1.2 eV. This arises from the trade-off between surface-molecule and molecule-molecule interactions, with the 45° tilting angle corresponding to a sliding of neighbouring molecular planes close to the one observed in the crystal structure [131]. Moreover, this model structure results in $\Delta\Phi$ = 1.5 eV, close to the experimentally observed value of $\Delta\Phi$ = 1.2 eV.

Summary

By combining the experimental and theoretical results, a coherent picture for the significant work function increase of G/Qu upon HATCN deposition, and its evolution as function of nominal coverage can now be constructed. Up to $\theta \sim 0.4$ nm, HATCN arranges in a flat-lying, low-density monolayer on graphene and generates an abrupt work function change $\Delta\Phi_{exp,0°}$ = 0.5 eV via a CT induced interface dipole (ID) (Fig. 5.17b), in very good agreement with the theoretical simulations where a value of $\Delta\Phi_{sim,0°}$ =0.55 eV was obtained. The CT is manifested experimentally as the low BE emission in the N 1s spectra (Fig. 5.9b. This comes in agreement with the theoretical simulations as shown in Fig. 5.17a. Intuitively,
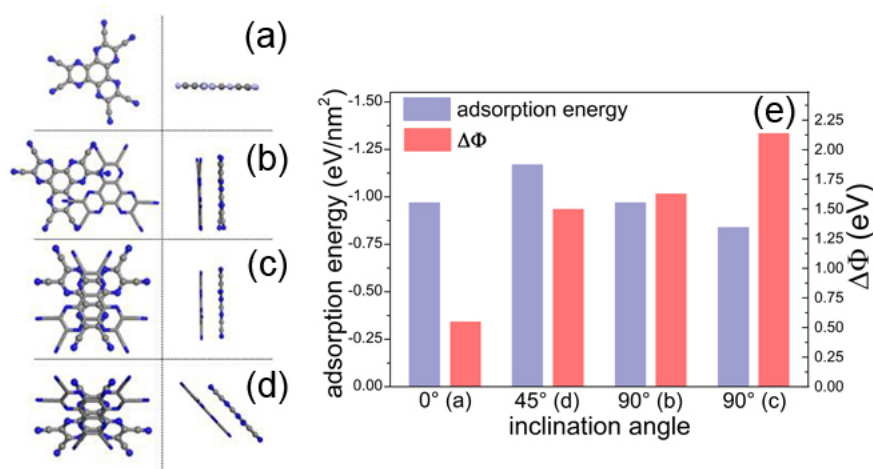
Figure 5.16: High density case. (a) flat lying HATCN (left: top-view, right: side-view, supercell surface 1.90nm^2), (b) dimer a inclined at 90° (supercell surface 1.49nm^2), (c) dimer b inclined at 90° (supercell surface 1.08nm^2), (d) dimer b inclined at 45° (supercell surface 1.69nm^2), (e) Adsorption energy and change in work function ($\Delta\Phi$) for the four orientations.

the (partial) negative charges are localized at the nitrogens, since they are the electron withdrawing groups.

Noteworthy, peak fitting yielded a peak-area-fraction of only about 10 % of charged species vs. neutral ones. This discrepancy may have two reasons: (i) The pronounced Volmer-Weber growth, where multi-layer HATCN may mask the signal from those HATCN molecules that directly interact with graphene. (ii) In the actual experiment the charge transfer to HATCN may be integer, i.e., not fractional as returned by simulations. However, the surface electrostatics are governed by the area-averaged charge distribution, and the co-existence of neutral and anionic HATCN molecules in the monolayer could result, as shown recently for C60 molecules adsorbed on a molecularly modified metal electrode [165, 166]. As θ increases, the system comes into the high-density regime and the molecules arrange vertically inclined (most likely at ca. 45°) to minimize the system E_{ads}, as revealed by DFT calculations. In this conformation, the work function is further increased as the nominally same CT/molecule induces a larger ID. At an inclination of 45°, the distance between the "centre" of negative charge (d) lies further away from graphene and according to $\mu = q * d$ (μ electric dipole, q charge, d distance be-

tween charges) the interface dipole (ID') increases due to the increased distance (Fig. 5.17c). This re-orientation in the high density regime unravels the second, additional $\Delta\Phi$ observed in Fig. 5.7c. This work function change occurs very slowly as function of nominal coverage due to the pronounced island growth, and a high nominal coverage is required to close the vertically inclined monolayer.
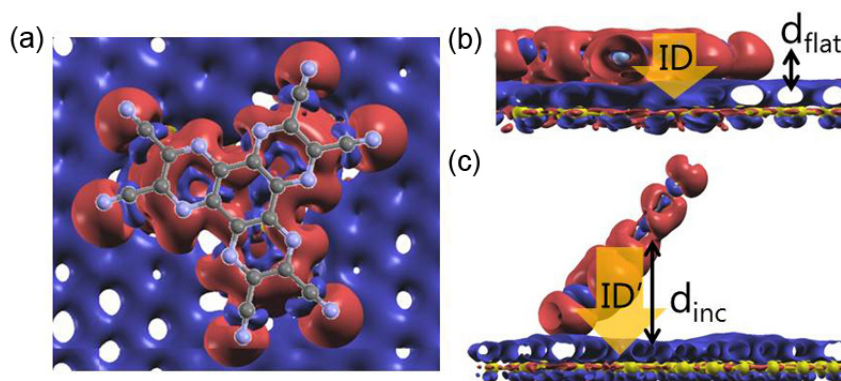
Figure 5.17: (a) Charge re-distribution of lying HATCN on graphene with molecule overlaid on top. Red represents build-up of negative charge and blue of positive charge, (b) Interface dipole (ID) for lying HATCN and (c) ID' when it is inclined at 45°.

A summary of the HATCN/G/Qu interface growth mode is given in Fig. 5.18. The very first molecules adsorb flat-lying on the surface (0.3 nm), as the molecular density is too low to find neighbours and form dimers. At higher coverages (1.2 nm) the flat-lying molecules in the monolayer re-orient (marked green with dashed green outline) to form a vertically inclined (sub)monolayer, with simultaneous multilayer formation. At even higher coverages ($\theta \geq 3.2$ nm), pronounced islanding occurs, but still molecules (marked green with dashed black outline) find the path to the bare graphene sheet and hence contribute to further increase the work function Φ via the CT mechanism described above. The molecules in direct contact with graphene are coloured green, while the molecules on the second layer and in the islands (not in contact) with the graphene sheet are marked grey.
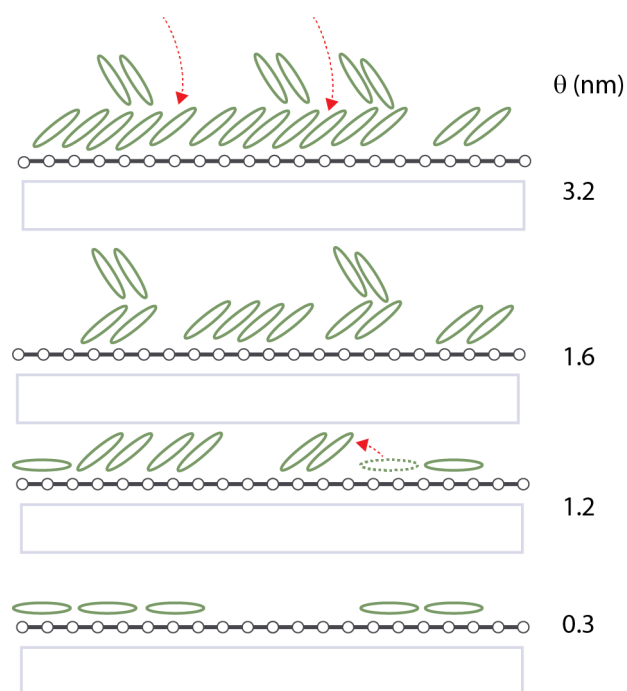
Figure 5.18: Model of growth of HATCN on graphene, showing the flat lying (sub)monolayer (0.3 nm), quasi vertically inclined (sub)monolayer (1.2 nm), vertically inclined (sub)monolayer with islands (1.6 nm) and molecules still reaching the surface at higher coverage (3.2 nm).

Energy level alignment

Fig. 5.19 shows a schematic of the energy level alignment occurring upon deposition of HATCN on G/Qu.

Before contact, the work function of G/Qu is at 4.5 eV. The theoretical I.E. and E.A. of HATCN are 9.1 eV and 4.7 eV respectively. When the HATCN is lying on G/Qu (Fig. 5.19b), the $\Delta\Phi$ = 0.5 eV, giving rise to the initial and abrupt work function increase. Upon the reorientation of HATCN (Fig. 5.19c) to 45°, once the coverage is increased, $\Delta\Phi$ finally reaches 0.7 eV, resulting to the final Φ = 5.7 eV. Since no shift is observed in the valence band or the C 1s core level of graphene, E_F is assumed to coincide with E_D. A possible reason for that, is that only a very low amount of HATCN is needed to be negatively charged on the surface of graphene, in order for equilibrium to be re-established (as observed also in the N 1s core level results, see Fig. 5.9a). This means that there is only a very low concentration of positive charges accumulated in the graphene layer to induce any observable shift in the valence- or core- level spectra
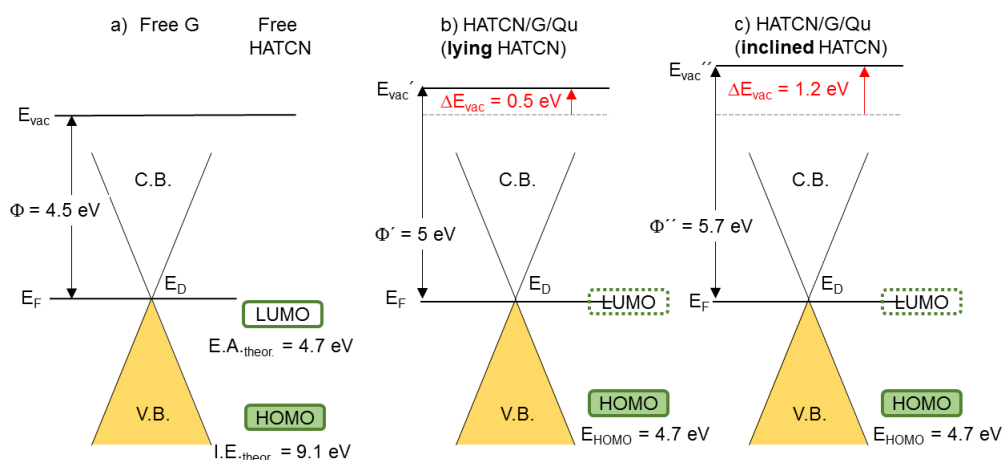
of graphene.

Figure 5.19: Energy level diagram (a) before adsorption of HATCN on graphene-on-quartz (G/Qu), (b) for HATCN adsorbed flat-lying on G/Qu and (c) for HATCN adsorbed vertically inclined on G/Qu.

5.2.6   Conclusion

The main result of this study is that the work function of graphene supported-on-quartz can be continuously tuned from 4.5 eV up to 5.7 eV upon depositing the strong molecular acceptor HATCN. The mechanism for this huge work function increase is attributed to a charge transfer between graphene and HATCN, and the complex behaviour of the work function as function of nominal coverage is rationalized by the combination of a density-dependent re-orientation of HATCN in the monolayer accompanied by pronounced overall Volmer-Weber growth of the molecular film. Angle-dependent DFT calculations together with NEXAFS measurements show that HATCN initially forms a flat-lying (sub)monolayer that increases the work function by 0.5 eV at low coverage, and a re-orientation of HATCN molecules on graphene to ca. 45° with respect to the graphene surface occurs at higher coverages. This is driven by a competition of minimizing the surface energy of graphene on one hand and maximizing molecule-molecule interactions on the other hand. The re-orientation causes a larger overall interface dipole that raises Φ by an additional 0.7 eV compared to the flat-lying acceptor layer.

HATCN was additionally deposited on G/Cu and HOPG, showing a very similar work function evolution, with no detectable push-back. The deposition of HATCN on these two flatter and more pure substrates, confirms that the growth of the molecule on graphene is not dependent on the possible corrugations, defects and contaminations that can be present on the transferred graphene sheet.

5.3 Functionalisation of graphene with F_6TCNNQ

The molecular acceptor F_6TCNNQ has already been used as p-dopant for organic semiconductors and was proved to improve the efficiency of devices, e.g., organic transistors and OLEDs [124, 125, 167, 168].

F$_6$TCNNQ was deposited on G/Qu and G/Cu, to study the work function change as the molecular acceptor is adsorbed on graphene as well as to exemplify whether the underlying graphene support plays a role in the charge transfer. Using UPS and XPS, electron transfer to the F_6TCNNQ was demonstrated and induced an increase in the work function of 1 eV (G/Qu) and 1.3 eV (G/Cu). NEXAFS was performed in order to study the orientation of the molecule when adsorbed on G/Qu. The results concerning the F_6TCNNQ/G/Qu were supported by DFT calculations from our collaborators.

5.3.1 Electronic properties of F_6TCNNQ on graphene-on-quartz

Valence electronic structure

Fig. 5.20 shows the UPS spectra upon incremental deposition of F_6TCNNQ on G/Qu. With increasing nominal mass thickness, the SECO shifts and yields an increase in Φ from the initial value of $\Phi = 4.5$ eV to the saturated value of $\Phi = 5.5$ eV, at a coverage of 0.4 nm, as shown in in Fig. 5.20a. The saturation of the work function is reached at a much lower coverage, in contrast to the case of HATCN adsorbed on graphene, indicating that a complete monolayer of the acceptor is readily formed with much lower amount of molecule being sublimed.

At a nominal mass thickness of $\theta = 0.2$ nm, a rigid shift of the valence level spectrum by ca. 0.6 eV towards higher BE is observed, as shown in Fig. 5.20b. The red dotted lines in Fig. 5.20b indicate the shift of the σ and π bands of graphene, which initially exhibit their peak maxima at ca. 8 eV BE and ca. 3.4 eV BE respectively. This energy shift is due to electron donation from the graphene sheet to F_6TCNNQ, that leaves excess holes accumulated in the graphene sheet, that causes p-type surface CT doping [56, 100, 169–171]. The p-doping is manifested energetically as a shift in the Fermi level of graphene. Thus, its entire valence level spectrum shifts towards higher BE.
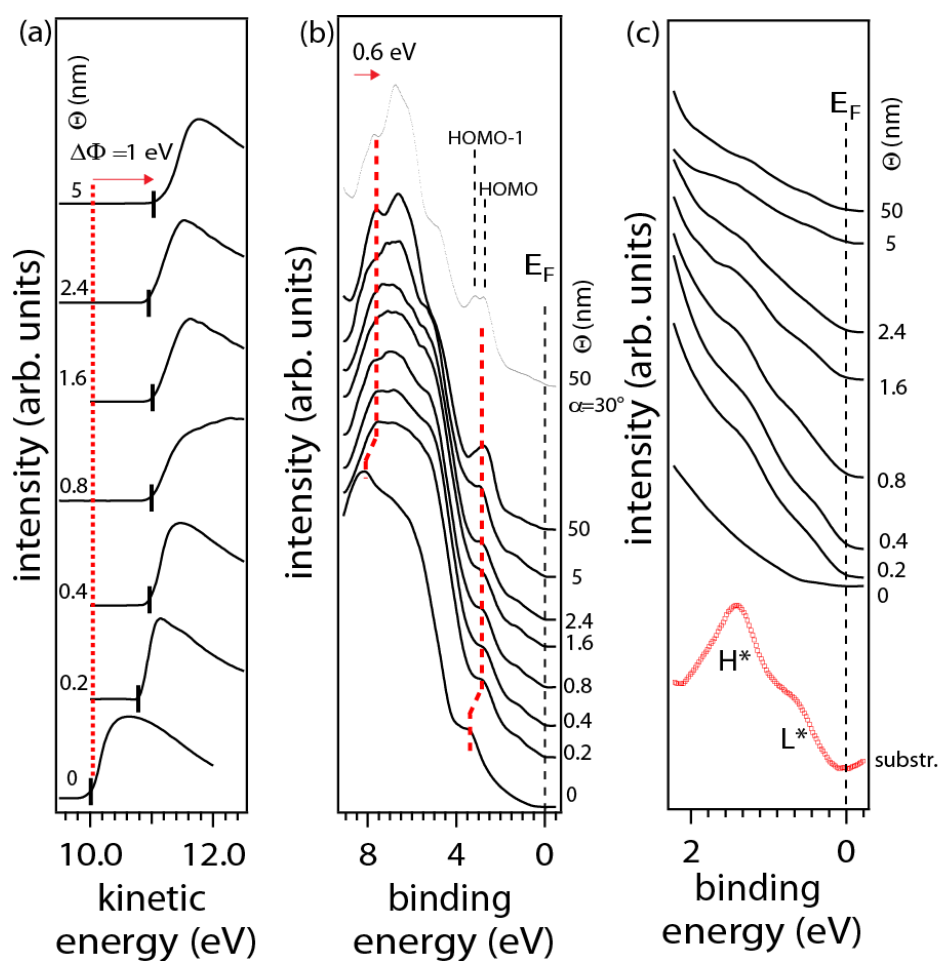
Figure 5.20: a) SECO onset b) valence level c) zoom of valence level spectra upon deposition of F_6TCNNQ on graphene-on-quartz. The red dotted line in (b) shows the energy shift of the valence level spectrum and in (c) the molecular valence level spectrum, after the graphene spectrum is subtracted as background.

This energy shift is accompanied by the appearance of two new photo-electron signals in the valence level region, labelled H* and L* with their peak maxima located at BE = 1.3 eV and BE = 0.6 eV respectively, as depicted in Fig. 5.20c. In order to obtain the molecular spectrum (at θ = 0.4 nm), without the contribution from graphene, the graphene photoelectron signal was subtracted. The subtracted spectrum clearly shows the two features H* and L* near the E_F region and is depicted with the red dotted line in Fig. 5.20c. Similar interfacial electronic states have been reported in the case of F_4TCNQ for e.g., the F_4TCNQ/Au(111) interface [22] and F_4TCNQ/graphene (epitaxially grown on SiC(0001)) [100]. The L* feature is assigned to emission from the former LUMO of the neutral molecule,

that now becomes populated, while the H* feature is assigned to emission stemming from former HOMO of the neutral molecule, which now gets energetically relaxed due to the reorganisation of the charges within the molecule, upon charge transfer. For the neutral molecule in the gas phase, the calculated IE = 7.41 eV and the EA = 5.17 eV (calculated using PBE0 functional and 6-31Gdp basis set), resulting in an energy gap of 2.23 eV. Thus, the energy separation of these two states is ca. 0.7 eV, much lower than the HOMO-LUMO gap of the neutral molecule. Such a drastic reduction in the energy gap between the frontier orbitals indicates a strong interaction between the molecular acceptor and the graphene layer [172].

After multilayer coverage of F_6TCNNQ on G/Qu, the features H* and L* are attenuated but do not get completely quenched, indicating non-uniform coverage of the substrate and the formation of islands. At θ = 50 nm, an emission feature attributed to the HOMO of the neutral molecule is clearly visible, exhibiting a peak maximum at BE = 2.8 eV and onset at BE = 2 eV. Using the HOMO onset, the I.E. of the molecule in the bulk is 7.5 eV, very close to the calculated I.E. of the molecule in the gas phase. Acquisition of the UPS spectra at emission angle (α) of 30° (see Fig. 5.20b, reveals two features with ΔE = 0.3 eV. The two peaks are attributed to the HOMO and HOMO-1 of the neutral molecule, with peak maximum at BE = 3 eV (onset at 2 eV) and 3.3 eV respectively.

Core level analysis

Fig. 5.21 shows the C 1s, N 1s , F 1s and Si 2p core level spectra as a function of F_6TCNNQ coverage on G/Qu. The C 1s core level of graphene shifts from BE = 284.5 eV to BE = 283.9 eV, after deposition of θ = 0.2 nm, accompanying the rigid shift of ΔE = 0.6 eV observed in the valence level spectrum. Emission from the graphene C 1s core level is strongly attenuated with increasing molecular coverage, however emissions are still visible in the spectrum even up to θ = 50 nm, suggesting strong island growth. Combining the C 1s evolution together with the Φ evolution, that saturates already at θ = 0.4 nm, at the coverage where the monolayer is presumably filled, the most probable mechanism of the film growth mode is concluded to be Stranski-Krastanov, where the molecules first proceed to form a closed monolayer on the surface and the subsequent molecules grow as islands on top of this first filled monolayer. Two new peaks are

observed in the C 1s core level region at BE = 287.4 eV and BE = 286 eV and are assigned to emissions from the CF groups and the CN groups together with the rest of the carbons in the heterocycle, respectively.

The N 1s core level spectra are deconvoluted using four Voigt components, as shown in Fig. 5.21b. The peak at BE = 397.5 eV (red colour) is assigned to emission from electron enriched F_6TCNNQ, in direct contact with the graphene layer, very similar to the already reported N 1s feature of anionic F4TCNQ on epitaxially grown graphene on SiC(0001) [56, 100, 173]. At θ = 0.1 nm, i.e., at sub-monolayer coverage, the N 1s spectrum contains only the CT-related peak, proposing that at this coverage, all the adsorbed molecules are electron enriched due to the CT occurring at the interface.

The peak at BE = 399.4 eV (blue colour), is clearly visible at θ = 0.2 nm and is assigned to emissions from nitrogens in two different environments: a) nitrogens in the neutral molecules that are located in the first monolayer that did not accept electrons from graphene, and b) nitrogens in neutral molecules located in multilayers. At multilayer coverage, the peak maximum of this feature shifts incrementally towards lower BE, and it saturates at BE = 399 eV at θ = 1.6 nm. This effect can have two origins: a) different molecular orientations in the multilayer coverage, resulting in different IEs of the molecule [160] or b) different screening of the photohole by the molecules than by the graphene layer. Since the first monolayer in direct contact with graphene is assumed to be complete at a coverage of ca. 0.4 nm, the fact that emissions from nitrogens located in neutral molecules are already present at nominal mass thickness of 0.2 nm supports growth of molecular islands already starting at sub-monolayer coverage.

The peaks at higher BE (green and orange colour) are attributed to shake-ups and are present already at very low coverage, since the screening of the photohole created during the photoemission process is not efficiently screened by the graphene layer, which is supported by an insulating substrate [100, 173, 174].

The CT-related feature is dominant at (sub)monolayer coverage, where all the adsorbed molecules appear to be negatively charged, and by increasing the film thickness the intensity of neutral F_6TCNNQ increases. This verifies that the CT occurs right at the interface between the molecules that are in direct contact with graphene layer. Fig. 5.21c shows the F 1s
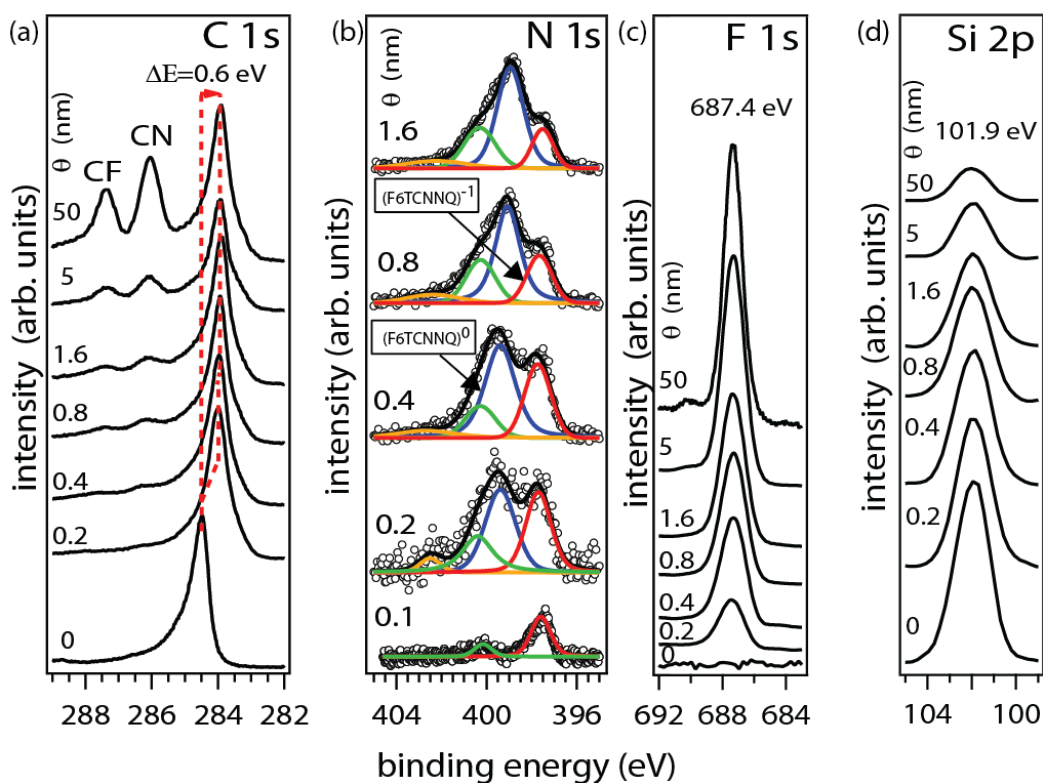
Figure 5.21: Core level spectra showing the evolution of (a) C 1s, (b) N 1s (c) F 1s and (d) Si 2p upon deposition of F_6TCNNQ on top of G/Qu. The N1s spectrum in (b) is fitted to uncover the underlying emissions.

spectrum of the molecule, which is at a constant BE = 687.4 eV from $\theta = 0.2$ nm up to $\theta = 5$ nm. No extra feature is observed at lower BE, as in the case of the N 1s, showing that there is no electronic interaction of the fluorines located on the periphery of F_6TCNNQ with the graphene layer, similarly to what was also observed for F_4TCNQ related interfaces in previous studies [175] and as will be explained in the theoretical section later.

Fig. 5.21d depicts the Si 2p core level due to emission from the supporting quartz (SiO_2) and is located at BE = 101.9 eV. Since there is no detectable energy shift in the BE of the Si 2p core level peak, it can be concluded that none or minimal CT occurs between the molecule and the underlying quartz support.

From the core level emissions, it is concluded that the withdrawn electrons are mainly localised in the nitrogens of the CN groups, located at the external part of the molecule.

5.3.2 Electronic properties of F_6TCNNQ on graphene-on-copper

Valence electronic structure

Fig. 5.22 shows the evolution of the valence level spectra of G/Cu with increasing coverage of F_6TCNNQ. With increasing nominal mass thickness, the SECO shifts in a similar manner to the F_6TCNNQ/G/Qu system and yields a $\Delta\Phi = 1.3$ eV from the initial value of $\Phi = 4.35$ eV to the saturated value of $\Phi = 5.65$ eV. The saturated work function is reached at a coverage of $\theta = 0.4$ nm, as shown in Fig. 5.22a.

The UPS spectra are dominated by emissions emerging from the underlying polycrystalline Cu support, hindering the discrimination between Cu and graphene features. Thus, it is not possible to unambiguously track any shift in the valence level spectra, as was observed in the F_6TCNNQ/G/Qu case. Accordingly to the G/Qu case, two new features labelled H* and L* appear close to the BE and are depicted in Fig. 5.22c. Their peak maxima are located at BE = 1.4 eV and BE = 0.7 eV respectively, as shown by the UPS spectrum at $\theta = 0.4$ nm with the pristine graphene spectrum subtracted (red dotted lines). The energy separation is similar to the case of F_6TCNNQ/G/Qu system, i.e., $\Delta E = 0.7$ eV, revealing a similar HOMO-LUMO gap renormalisation of the electron enriched F_6TCNNQ on G/Cu. Non-uniform coverage and island growth of the G/Cu substrate is evident, since the interfacial electronic states H* and L* are present up to multilayer coverage $\theta = 5$ nm, similar to the case of F_6TCNNQ adsorbed on G/Qu.

Core level analysis

The XPS spectra of the associated core levels are shown in Fig. 5.22. The C 1s core level due to emission from graphene (Fig. 5.22a) is initially at BE = 284.4 eV and after deposition of $\theta = 0.4$ nm F_6TCNNQ it shifts towards lower BE by $\Delta E = 0.4$ eV. This shift is attributed to a potential difference built between the copper support and the overlaid molecular acceptor, and will be discussed in more detail in the theoretical section.

Upon further molecular deposition, no further shift in the BE is observed. The molecule-related emissions in the C 1s core level region are located at a lower BE = 286.3 eV for the carbons in the CF groups and BE = 284.9 eV for the carbons in the CN groups when compared to the G/Qu
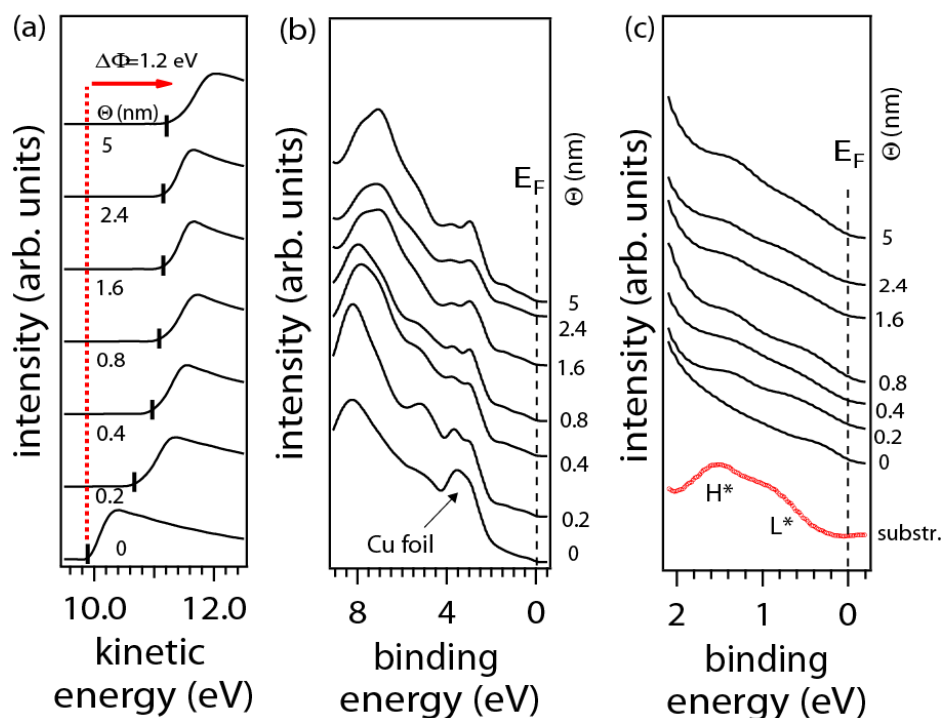
Figure 5.22: a) SECO onset b) valence level spectra c) zoom of valence level spectra upon deposition of F_6TCNNQ on graphene-on-copper. Red dotted lines in (c) indicate the molecular spectrum at $\theta = 0.4$ nm, after subtraction of the pristine graphene spectrum.

case, but the energy difference (ΔE) between these two emissions is constant at $\Delta E = 1.4$ eV, similar to the G/Qu system. The appearance of these emissions at lower BE is attributed to better photohole screening when graphene is on conducting support, i.e. Cu, versus the insulating support, i.e. quartz.

The N 1s core level spectra of the F_6TCNNQ/G/Cu interface show significant differences when compared to the F_6TCNNQ/G/Qu system, as depicted in Fig. 5.23b. Up to $\theta = 0.2$ nm, a fitting routine with only a single Voigt profile provides a satisfactory fit for the N 1s core level spectrum. Similar to F_6TCNNQ/G/Qu case, the peak at BE = 397.7 eV is assigned to emission from the nitrogens in the molecule that have withdrawn electrons from the underlying substrate. The absence of shake-up satellites evidences the common behaviour in the case of a metallic substrate [176]: the valence electrons with energy near the Fermi level of the metal readily screen the photo-hole induced by the excitation of the photo-electron
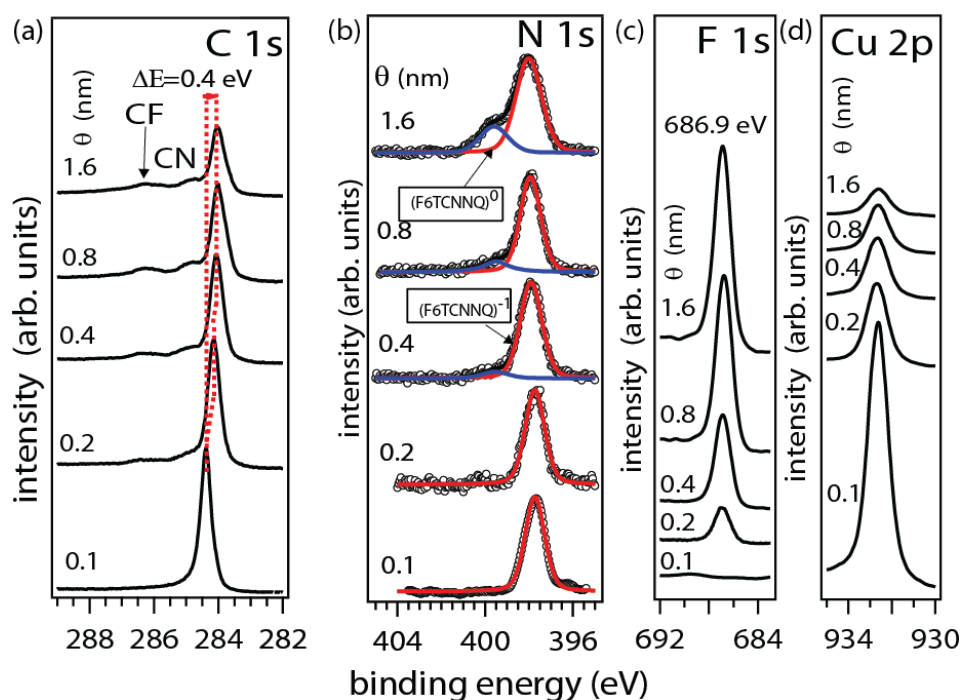
Figure 5.23: Evolution of a) C 1s, b) N 1s c) F 1s and d) Cu $2p_{3/2}$ upon deposition of F_6TCNNQ on graphene-on-copper. The N 1s spectrum contains the deconvolution to the underlying emissions.

and consequently suppress shake-up satellites. For $\theta > 0.2$ nm, the N 1s core level emissions stemming from the neutral F_6TCNNQ species start appearing in the spectra and increase in intensity with increasing nominal mass thickness. Interestingly, the molecular monolayer on the G/Cu substrate has the majority of the molecules negatively charged, in contrast to the G/Qu interface, where neutral molecules are present already at $\theta = 0.2$ nm.

The F 1s core level spectrum, assigned to emissions from the fluorines (Fig. 5.23c further corroborates more efficient photohole screening, as it is also located at $\Delta E = 0.5$ eV lower in BE than the F 1s core level when the molecule is deposited on G/Qu. Furthermore, the core level emission from the fluorines support, similar to G/Qu, that no, or minimal charge is transferred into the the fluorines. The Cu $2p_{3/2}$ core level spectrum in Fig. 5.23d shows the emission from the copper support, verifying that no chemical interaction between the molecule and copper is present, since no extra peak arises in the Cu$2p_{3/2}$ spectrum.

5.3.3 Molecular orientation

To obtain insight into the molecular orientation of F$_6$TCNNQ deposited on G/Qu in submonolayer and ca. monolayer coverage, NEXAFS was performed for $\theta = 0.2$ nm (Fig. 5.24a) and $\theta = 0.4$ nm (Fig. 5.24b) respectively. The transitions at the N K - edge are identified by NEXAFS simulations that will be presented later on. Fitting the intensity ratio of the peak at 399.1 eV that corresponds to transition from N 1s $\rightarrow \pi^*$ (p_{xy}) as a function of polarisation incidence angle, shown in Fig. 5.24c for $\theta = 0.2$ nm and Fig. 5.24d for $\theta = 0.4$ nm, with the molecular orientation on the graphene layer being $\psi_{inc} = (23 \pm 1)°$ and $\psi_{inc} = (24 \pm 1)°$. Given that NEXAFS is an area-averaging technique, the result implies that the majority of molecules are flat lying on G/Qu, in both sub-monolayer and monolayer coverages.
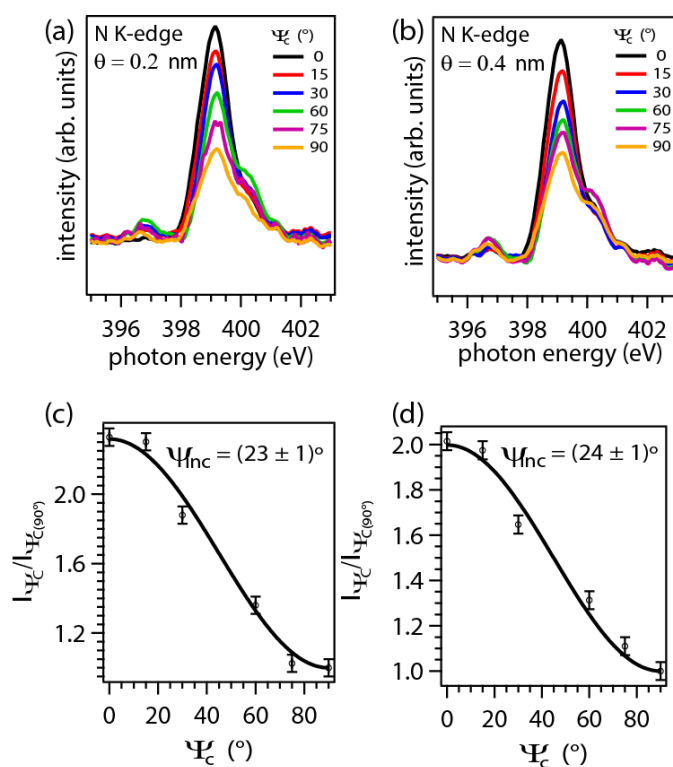
Figure 5.24: Series of NEXAFS spectra as a function of incidence angle Ψ_c from normal incidence (0°) to grazing incidence (90°) of the π^*-region at the N K-edge for a 0.2 nm (a) and a 0.4 nm (b) thick F$_6$TCNNQ film grown on G/Qu. c) and d) are plots of the relative π^*-orbital intensities as a function of the photon incidence angle Ψ_c. The solid line corresponds to the best fit of the intensity evolution of the molecule giving aromatic plane tilt angle of 23° (c) and 24° (d).

5.3.4 Theoretical modelling

Modelling of N K-edge of free F_6TCNNQ

In Fig. 5.25, the calculated NEXAFS spectrum of gas-phase F_6TCNNQ is presented. The simulations help to identify the three main transitions that involve the nitrogens in the CN groups and are observed in the experimental NEXAFS spectra. The lowest and highest energy transitions (at photon energies 398 eV and 402.2 eV) involve N 1s $\rightarrow \pi^*(p_z)$ transitions and are observed in the experimental spectra at photon energy = 396.6 eV and photon energy = 402.2 eV, respectively. The peak at photon energy 401 eV involves N 1s $\rightarrow \pi * (p_{xy})$ transitions and is observed in the experimental spectra at 399.1 eV.
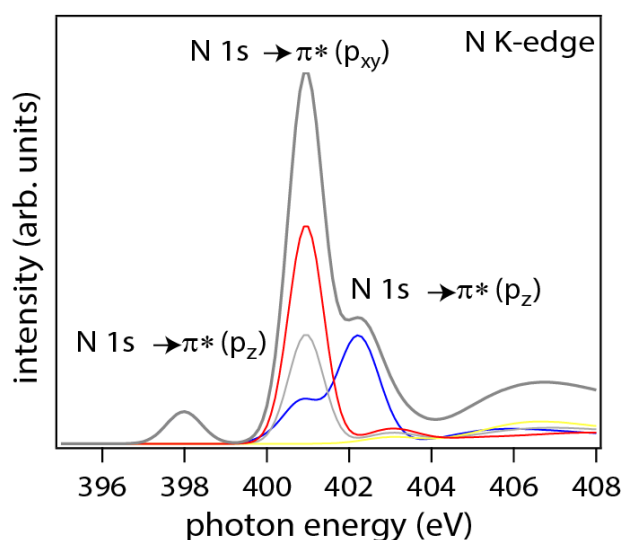
Figure 5.25: Calculated NEXAFS spectrum for free F_6TCNNQ molecule, showing the intensity distribution of the three dominant peaks.

Charge densities and band structures calculations

First principle calculations were performed in order to elucidate the features observed in the valence region of the F_6TCNNQ/G interface. Fig. 5.26 shows the density of States (DOS) of graphene (black) and F_6TCNNQ/G (red). The quartz support was not implemented in the following simulations, since, due to its highly insulating character it does not affect the charge redistribution at the F_6TCNNQ interface. Thus,

the experimentally studied G/Qu substrate corresponds to free-standing graphene (G) in the simulations.
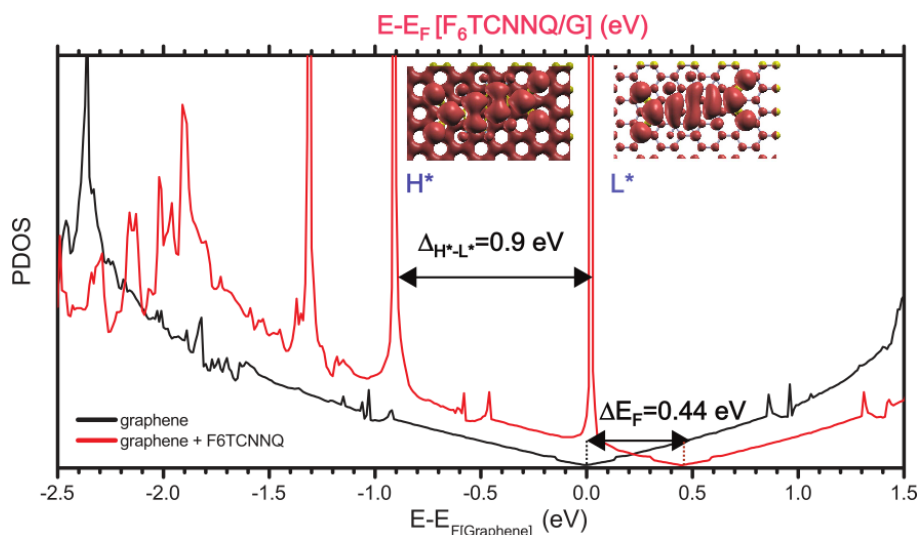
Figure 5.26: Partial density of states (PDOS) of graphene (black) and F_6TCNNQ adsorbed on graphene (red) and LDOS of the H* and L* peaks. ΔE_F depicts the shift of the Fermi level and $\Delta_{H'-L'}$ the energy difference between H* and L*. Calculations performed by A. Giannakopoulos (Uni. Mons).

There is good agreement between theory and experiment in two important aspects. At first, density of states simulations capture the shift of the Dirac Point (E_D) of graphene towards lower BE, by $\Delta E_F = 0.44$ eV. This shift is reproduced in the band structure calculations in Fig. 5.27c. The shift in the vacuum level is also reproduced in the simulations, giving $\Delta E_{vac}= 0.64$ eV. The total theoretical $\Delta \Phi$ turns to be 1.08 eV. Secondly, there are two new electronic states close to E_F. Integration around the energy of the two new states (L* and H*) gives the local density of states (LDOS). The LDOS displays the features of the LUMO (L*) and HOMO (H*) of F_6TCNNQ. Furthermore, the LUMO of the molecule is found close to the E_F. The energy gap between H* and L* ($\Delta E = 0.9$ V) agrees with the experimental values obtained by UPS ($\Delta E = 0.7$ eV).

In order to investigate how the copper/graphene contact interferes with the CT mechanism at the graphene/molecule interface, DFT simulations for graphene placed on top of five layers of Cu(111) were performed. The band structures of the resulting unit cells are shown in Fig. 5.27.

Reference [177] gives a good account on the interaction between Cu

and graphene. In the case of copper, due to the push back effect, the surface chemical potential of metal and graphene are not equal, thus, interface CT leads to their final equilibration, with the common chemical potential between graphene and copper being determined by the metal. The Dirac point of graphene does not coincide with the E_F of the metal, because the Pauli exclusion interaction is negligible for graphene compared to the 3D metal, leading to different modification of the vacuum level for each of them.
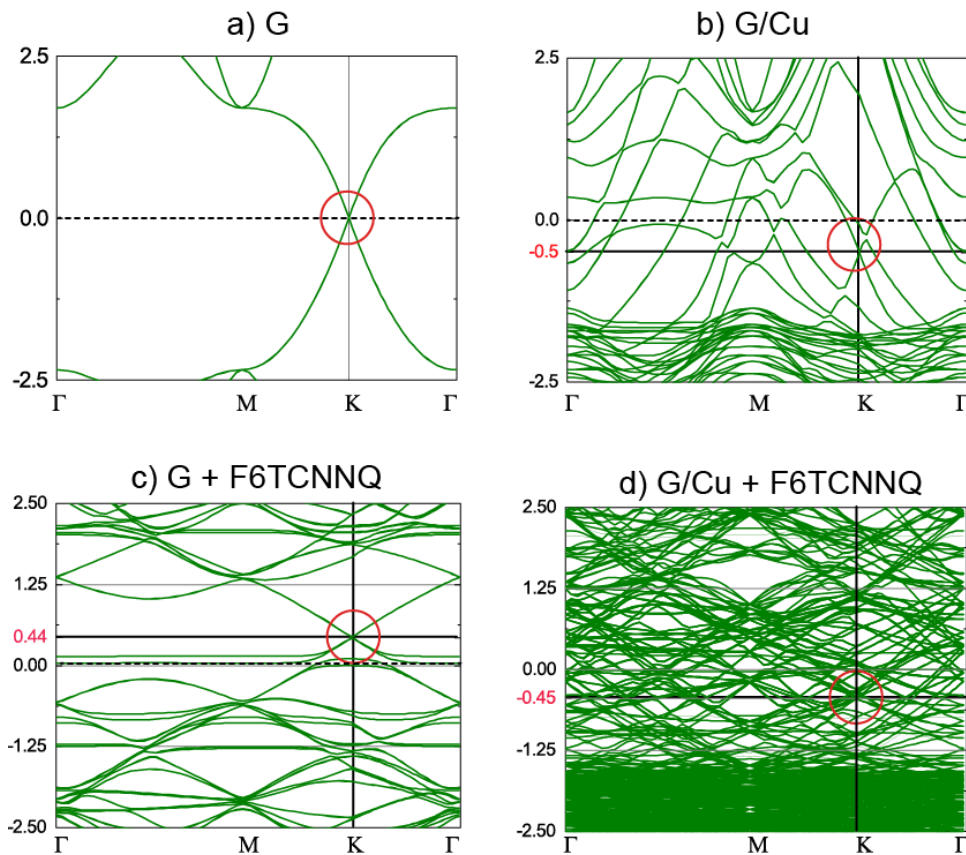
Figure 5.27: Electronic band structures of (a) graphene (G) and (b) G on Cu unit cells. Figures (c) and (d) show the electronic band structures of F_6TCNNQ adsorbed on top of (a) and (b) supercells respectively. The red circles indicate the position of the Dirac point and the dashed line indicates the position of Fermi level, which is set to zero. Calculations performed by A. Giannakopoulos (Uni. Mons).

The push back induced reorganisation of the electronic density is visualised in the charge density plot in Fig. 5.28b. The plot shows excess electron density at the Cu surface and reduced electron density close to

graphene, resulting to the reduction of the work function. As a result, electron transfer from Cu to graphene occurs. The resulting electron enrichment in graphene is however masked by the larger push back effect, hence the shift of the Dirac point is located 0.5 eV below the Fermi level, corresponding to n-doping of the graphene layer.

The next step was to simulate the physisorbtion of F_6TCNNQ on top of graphene lying on Cu(111). Interestingly, an almost negligible shift in the Dirac point is observed with respect to E_F, $\Delta E = 0.05$ eV, leaving the Dirac point 0.45 eV below E_F. I.e., the adsorption of F_6TCNNQ on G/Cu only slightly affects the doping level of the graphene sheet, which is quantified as the energy difference between E_F and E_D.

The vacuum level shift in the case of graphene placed on Cu(111) is much larger than for free-standing graphene, $\Delta E_{vac} = 1.25$ eV giving a total $\Delta\Phi$ of 1.3 eV, supporting the experimental observations.

In order to quantify the origin and magnitude of the charge being exchanged between F_6TCNNQ and G or G/Cu, the differential charge densities (DCD) were derived and are presented in Fig. 5.28. In the case of F_6TCNNQ adsorbed on free standing graphene (G) Fig. 5.28a the CT reaches the maximum value of -0.38 e (e is the elementary charge of one electron) at the G/F_6TCNNQ interface.

In the case of G/Cu (Fig. 5.28b,c,d) the charge density plots were computed using two different charge partitioning schemes, in order to elucidate the charge transfer mechanism.

The first scheme considers the following fragments to compute the DCD: (a) the Cu(111) and (b) graphene interacting with F_6TCNNQ (GF_6TCNNQ in Fig. 5.28c). This DCD is reminiscent of Fig. 5.28a and Fig. 5.28b, i.e., push-back induced charge redistribution at the G/Cu interface and increased electronic density on the molecular acceptor. The second scheme considers: (a) graphene interacting with Cu (CuG in Fig. 5.28d) and (b) F_6TCNNQ. This partitioning helps to "mask" the push-back contributions caused by the G/Cu interface, since the molecular acceptor on top does not cause significant pillow effect. Thus, the contributions to the charge density distributions are now dominated by the electron transfer to the molecular layer rather than charge density redistributions due to the push-back effect. Fig. 5.28d now clearly shows an increased charge density around graphene, that was not observable in Fig. 5.28c due to the
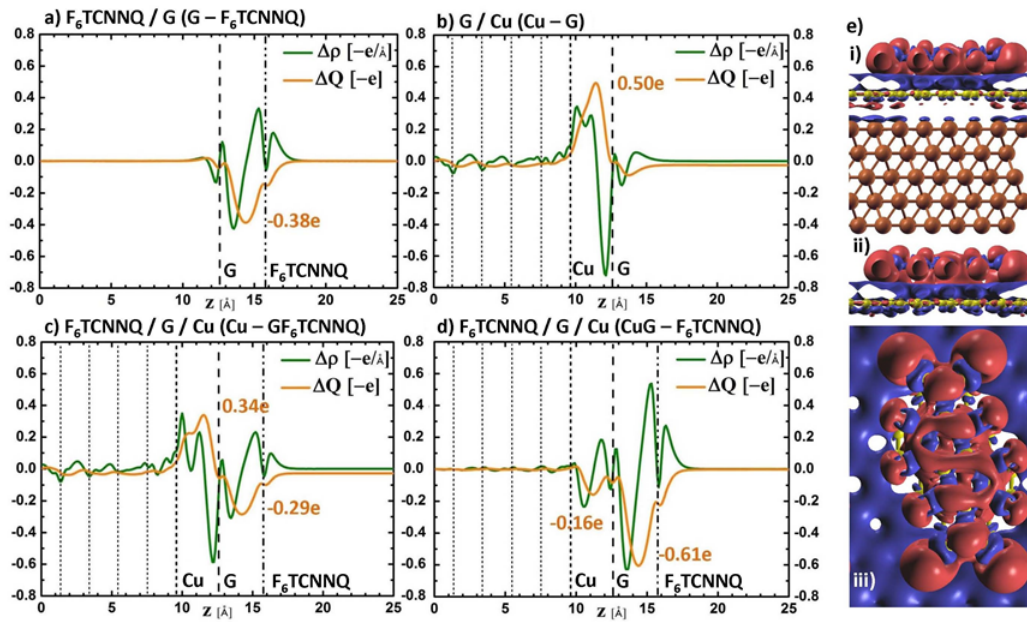
Figure 5.28: Plane averaged differential charge density (DCD), $\Delta\rho$ (z) (green), charge transfer amount Δ Q(z) (orange), side view of the DCD isosurface for F_6TCNNQ adsorbed on (e(i)) graphene and (e(ii)) graphene-on-copper and e(iii) represents a top view DCD isosurface for F_6TCNNQ on graphene. The electron accumulation and depletion regions in the DCD isosurface are indicated by red and blue colour for negative and positive charge respectively. The amount of charge transfer is indiccated in each plot. Parentheses indicated the subsystems used for the DCDs. Short dashed lines indicate the copper layers, dashed lines indicate the graphene layer and double dotted lines indicate the F_6TCNNQ layer. Calculations performed by A. Giannakopoulos (Uni. Mons).

dominance of the push-back effect. This increased charge density around graphene is in line with n-doping of the graphene layer, manifested as the lower energy of E_D with respect to E_F in the band diagram in Fig. 5.27d. As a conclusion, the charge transfer occurs from the Cu vast electron reservoir into the combined graphene/molecule system, with the majority of the charge being transferred into the molecular acceptor. This CT then generates a potential difference across the graphene sheet being sandwiched between the positive image charges in Cu and the negative charges in F_6TCNNQ. Consequently, this potential difference shifts the energy levels of graphene to lower BE. The experimentally observed 0.4 eV shift in the C 1s for F_6TCNNQ/G/Cu is due to this effect.

An additional important information extracted from the DCD plots is

the amount of charge being transferred, crucial in explaining the difference in the N 1s and F 1s core level emissions observed in XPS.

At first, the top view of the DCD isosurface for F_6TCNNQ interacting with free standing graphene, establishes that the major electron density is localised around the CN groups. Secondly, the minimal electron density around the F atoms explains the absence of any observable shift in the BE of the F 1s core level emission in the XPS spectra.

The total amount of electrons being transferred predominantly in the CN groups of the molecular acceptor in the case of G/F_6TCNNQ is -0.38 e. This amount almost doubles to -0.61 e when graphene lies on Cu(111). Under the assumption that the growth mode of the acceptor on G/Qu and G/Cu is the same, which is evidenced by the UPS and XPS evolution profiles, it is concluded that more molecules are charged when graphene is supported by Cu than Qu. This comes in agreement with the observation that in the N 1s core level spectra, 50% of the molecules are charged in the first monolayer for G/Qu but ca. 100% are charged in the first monolayer for G/Cu.
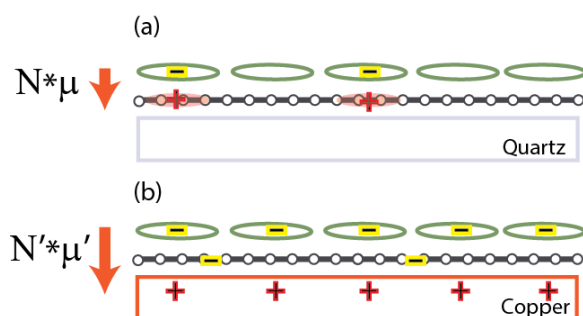
Figure 5.29: Schematic illustration showing the charge transfer occurring for the case of (a) graphene-on-quartz and (b) graphene-on-copper. Electrons are originating from graphene in the case of graphene-on-quartz and copper in the case of graphene-on-copper. N (N') represent the number of formed dipoles and μ (μ') the magnitude of the formed dipoles. The dipoles are represented red arrows.

This increased amount of CT, together with the fact that being withdrawn from Cu, provide an explanation for the higher $\Delta\Phi$ observed for G/Cu (1.3 eV). In this case (a) the dipole formed between the negative charge in the molecule and the image positive charge in the metal would be greater, since the distance between the charges is larger (see Fig. 5.29b) and (b) the number of such dipoles is larger (see Fig. 5.29b) since more

molecules get charged. When the transferred charge originates from graphene, this dipole is lower since (a) the molecule-graphene distance is lower and (b) less molecules get charged (see Fig. 5.29a. The calculated values of the $\Delta\Phi$ are in very good agreement with the experimental ones. The $\Delta\Phi$ in the case of standalone graphene is 1.05 eV, while for the case of the metalic substrate is 1.27 eV.

Energy level alignment scheme
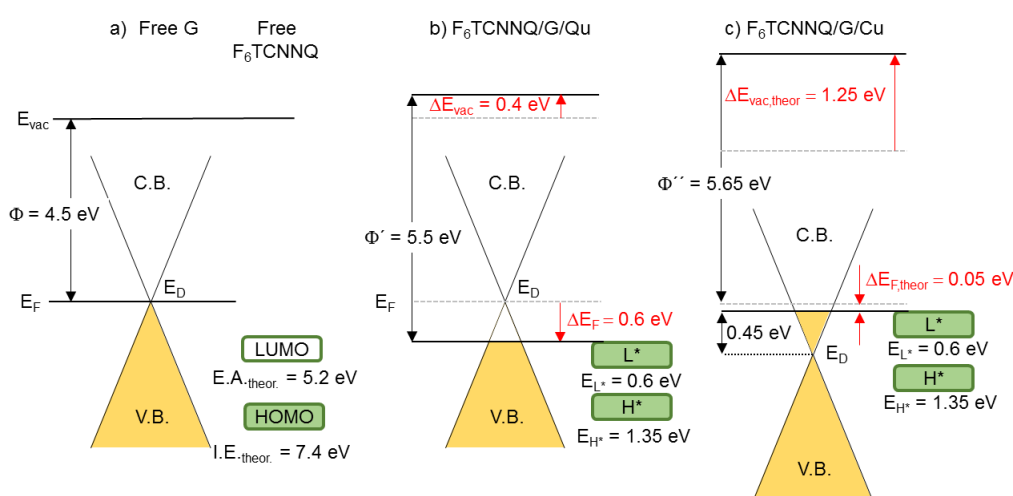
Figure 5.30: Energy level diagram for (a) free graphene (G) and free F_6TCNNQ, (b) F_6TCNNQ/G/Qu interface, (c) F_6TCNNQ/G/Cu interface. In (a), the electron affinity (E.A.) and the ionization energy (I.E.) are calculated for the gas phase (free) molecule before contact with graphene. In (b) and (c), the energy positions of the populated LUMO (L*) at E_{L*} = 0.6 eV and of the relaxed HOMO (H*) at E_H = 1.35 eV are derived from the experimental data. Φ corresponds to the work function, E_{vac} the vacuum energy level, E_F the Fermi level and E_D is the Dirac point of graphene. C.B. and V.B. are the conduction and valence band of graphene. The values are experimentally obtained unless otherwise indicated (theor.).

Fig. 5.30 shows a simplified valence energy level diagram before and after the formation of the interface for the case of F_6TCNNQ physisorbed on G/ Cu and G/Qu. To position the frontier molecular levels of F_6TCNNQ the calculated DFT gas phase values of the ionization energy (7.4 eV) and electron affinity (5.2eV) were used.

In the G/Qu case, the measured initial work function of graphene is 4.5 eV (Fig. 5.30a). After contact, a shift in E_F is observed, since doping of the graphene sheet occurs, lowering E_F by $\Delta E_F \sim 0.6$ eV, as measured experimentally (the calculated shift is 0.45 eV). The remaining work function increase results from an upward vacuum level shift due to the reorganization of positive and negative charges giving rise to a dipole at the interface between F$_6$TCNNQ and graphene, with yields an additional shift of ~ 0.4 eV (~ 0.65 eV) as measured (calculated). The overall change in work function is $\Delta\Phi$= 1.0 eV (1.1 eV) from measurements (calculations).

In the G/Cu case, the measured (calculated) initial work function of graphene lowers to 4.35 eV (4.15 eV) due to n-doping. The graphene layer remains n-doped in the presence of the overlaid acceptors with additional electronic density being transferred from the vast metal electron reservoir through graphene. As a result, the Dirac point shifts marginally, but the larger in amplitude and longer distance electron transfer from Cu to F$_6$TCNNQ is accompanied by a very large vacuum level shift that accounts for more than 95 % of the total work function shift, $\Delta\Phi$=1.3eV from both measurements and calculations.

5.3.5   Conclusion

In this chapter, a detailed insight into the interaction of graphene molecularly modified by F$_6$TCNNQ supported by insulating quartz versus metallic copper was presented. A substantially large work function increase of 1.0 eV was observed when the molecular acceptor F$_6$TCNNQ was deposited onto G/Qu. The work function increase was experimentally and theoretically deconvoluted into two contributions: (a) surface charge-transfer p-doping of graphene that gives $\Delta E_F = 0.6$ eV and (b) dipole formation at the F$_6$TCNNQ/G interface, resulting from the charge reorganization that gives a further $\Delta E_{vac} = 0.4$ eV.

When the underlying substrate was G/Cu, the work function reached a larger increase of 1.3eV. The transferred charged was theoretically confirmed to originate from the Cu substrate and the doping level of graphene did not change and remained of n-type. In this case, a potential difference was built between the molecular acceptor and Cu that consequently shifted the energy levels of graphene, sandwiched between the two. The

potential difference is manifested experimentally as a shift in the C 1s core level of G/Cu.

The charge transfer was experimentally confirmed by the lower BE N 1s emissions for both substrates.

The molecular acceptor F_6TCNNQ offers another alternative for raising significantly the work function of graphene, which, in contrary to HATCN (discussed in previous section), can readily saturate the work function with only a low molecular coverage of $\theta \sim 0.4$ nm.

Thus, it provides a transparent electrode that is highly conducting, since the graphenes sp2 network is only weakly perturbed after physisorption of F_6TCNNQ. Furthermore, it provides a p-doped graphene layer with a work function that matches the frontier energy levels of transport materials commonly used in many (opto-)electronic devices. When, instead, a Cu substrate is used, the work function is increased even further (by 1.3eV), albeit the fact graphene is n-doped. Therefore, this n-doped graphene, and generally any molecular-acceptor-modified n-type graphene, can yet be employed for hole injection into (organic) semiconductors in devices.

5.4 Functionalisation of graphene with organometallics

A lot of effort has been dedicated in designing stable and efficient donor molecules to be used as n-dopants and subsequently reduce the work function of electrodes.

A very recent class of such molecules are dimeric organometallics (or metallocenes). The monomeric form of these compounds consists of a transition metal atom, that is bound via a five-fold coordination to two cyclopentadienyl rings, with further ligands attached around the cyclopentadienyl ring [178]. These kind of monomers have been proved efficient electron donors [178, 179] but their low molecular weight together with their low ionisation energy introduce the disadvantage of high reactivity in air and high volatility[180]. The dimeric forms of these compounds, exhibiting twice the molecular weight have lower volatility and in addition, the formation of the dimers "masks" the highly reactive monomers [127, 129].

In this chapter, the dimers of: (a) ([RhCp*Cp]$_2$) and (b) ([RuCp*mes]$_2$) [126–129] were employed in order to n-dope and in parallel decrease the work function of G/Qu. In the following, the photoemission results of the [RhCp*Cp]$_2$ and [RuCp*mes]$_2$ molecules adsorbed on G/Qu will be shown.

5.4.1 [RhCp*Cp]$_2$ on graphene-on-quartz

Valence electronic structure

Fig. 5.31 presents the evolution of the UPS spectra upon sequential sublimation of [RhCp*Cp]$_2$ on G/Qu. Fig. 5.31a the SECO onset, that corresponds to Φ decreases by 1.4 eV. Note that, this molecule did not give a rate in the QCM, but only an increase in the base pressure in the preparation chamber, hence what is reported here will be the sublimation time t in seconds. The saturation of Φ is achieved with a very small amount of molecule deposited, t = 10 s; and after this deposition, the work function saturates at Φ = 3 eV.

The large range UPS spectrum (Fig. 5.31b) shows three photoelectron signals at BE = 2.5 eV (peak A) and BE = 4.4 eV (peak C). Between these two peaks a shoulder, marked (B), is evident. According to a recent the-
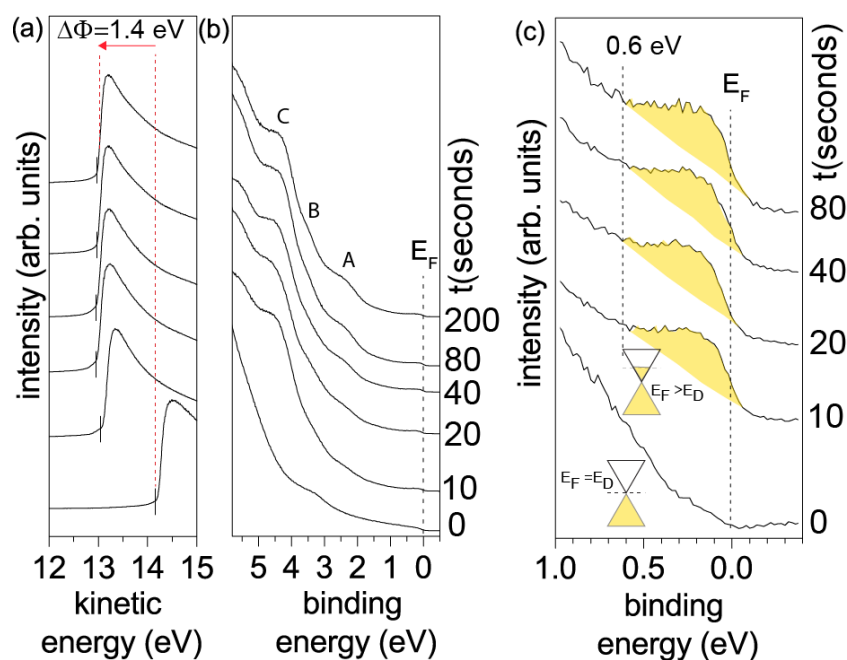
Figure 5.31: (a) SECO evolution and (b) Valence level evolution upon [RhCp*Cp]$_2$ deposition. (c) Zoom of UPS spectra near E$_F$. The shaded parts show the filled conduction band of graphene. The energy distribution around the Dirac point is schematically illustrated for t = 0 s and 10 s, with t being the sublimation time.

oretical study on the electronic structure of [RhCp*Cp]$_2$ [181], the emission features assigned with A and B can be attributed to the HOMO and HOMO-1 of the dimer, [RhCp*Cp]$_2$. They consist predominantly of the d orbital of rhodium hybridised with C-C bonding orbitals associated with the central molecular bond, while feature marked C corresponds, again, to the d orbital of rhodium, mixed with the cyclopentadienyl π orbitals. As will be shown later in the XPS spectra, a high amount of the adsorbed molecular donor exists on the interface in its cationic form. Thus, these molecular features are convoluted with the photoelectron emissions stemming from the the cations. The intensity of these peaks remains approximately constant up to t = 200 s.

When zooming into the E_F region in Fig. 5.31c, an additional emission feature appears in close proximity to E_F (shaded area), creating a dip in the otherwise linear spectrum of graphene.

The assignment of this peak is already reported in ref. [128]. It is attributed to the filled conduction band (C.B.) of graphene by donation of

electrons from [RhCp*Cp]$_2$. This emission feature could be alternatively attributed to molecular feature stemming from the positively charged monomer, since the theoretical value of the IE of the cation is 2.7 eV, the HOMO should theoretically be located at a BE near the E_F. Since such kind of emission close to the E_F was not observed after deposition of this donor molecule on a variety of substrates, e.g. Au(111), Ag(111), ITO, PEDOT:PSS the attribution of this emission to a molecular feature can be excluded (unpublished work).

The dip in the spectrum is attributed to the location of the Dirac point, that is shifted by $\Delta E = 0.6\,$eV relative to E_F upon deposition of [RhCp*Cp]$_2$ (which is aligned with the electron analyser, at BE = 0 eV). The dip in the emission intensity does not fall to zero, as one would expect, due to experimental limitations in resolution.

As this feature is evidently an interface feature, one would expect that it should disappear with longer sublimation times. The reason this does not take place can be explained using the following argument: the multilayers are weakly physisorbed and desorb on a time scale of the order of the transfer of the sample from the preparation chamber to the analysis chamber with base pressure $< 10^{-9}$. Moreover, the high concentration of cations at the surface can result to a Coulombic repulsion of subsequently deposited dimers, which can convert to their monomeric cationic form during sublimation. In addition, prominent island growth of the molecule on the graphene layer occurs, thus photoelectron signals stemming from the interface are always present, despite the fact that the sublimation time is increased. This reasoning is further supported by the following discussion concerning the core level spectra.

Core level analysis

The core-level spectra upon deposition of [RhCp*Cp]$_2$ are shown in Fig. 5.32. After deconvolving the C 1s core level spectrum into the underlying emissions, shown in Fig. 5.32a, a shift of the graphene-related feature by ~ 0.4 eV towards higher BE is evidenced, similar in magnitude to the shift observed in the UPS spectra. The unambiguous determination of the exact ΔE in C 1s core level spectrum is not possible, even after the deconvolution of the spectrum, because the carbon emissions stemming from the molecule are very close in BE to the carbon emissions from
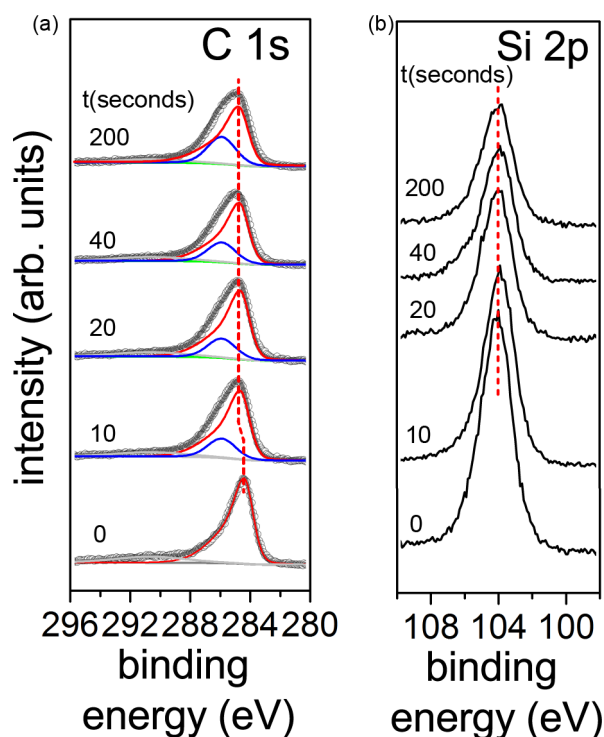
Figure 5.32: Evolution of (a) C 1s core level spectra with red lineshape showing the emissions stemming from graphene and blue lineshape are molecular features and (b) Si 2p XPS spectra upon deposition of [RhCp*Cp]$_2$ on graphene-on-quartz (G/Qu). The red line in C 1s core level spectrum is a guide to the eye, showing the shift in energy upon the first deposition.

graphene. Still, the spectra clearly verify a rigid shift of all the energy levels of graphene towards higher BE as a result of n-doping of graphene that induces the shift of E_F upwards with respect to E_D.

The Si 2p core level, Fig. 5.32b, stemming from the supporting quartz shows no energy shift, which evidences that the underlying quartz substrate is not involved in the charge transfer process, as was also observed in the case of HATCN and F_6TCNNQ.

Upon increasing the nominal thickness of the adsorbate, the adsorbate-related emissions in the C 1s core level emission region do not increase significantly in intensity, confirming the instability of the multilayers and/or the island growth of the molecule on the graphene layer. This is also consistent with the low attenuation of graphene related C 1s core level emission and Si 2p core level from quartz.

Fig. 5.33 shows the Rh 3d core level emission region. The fitting was
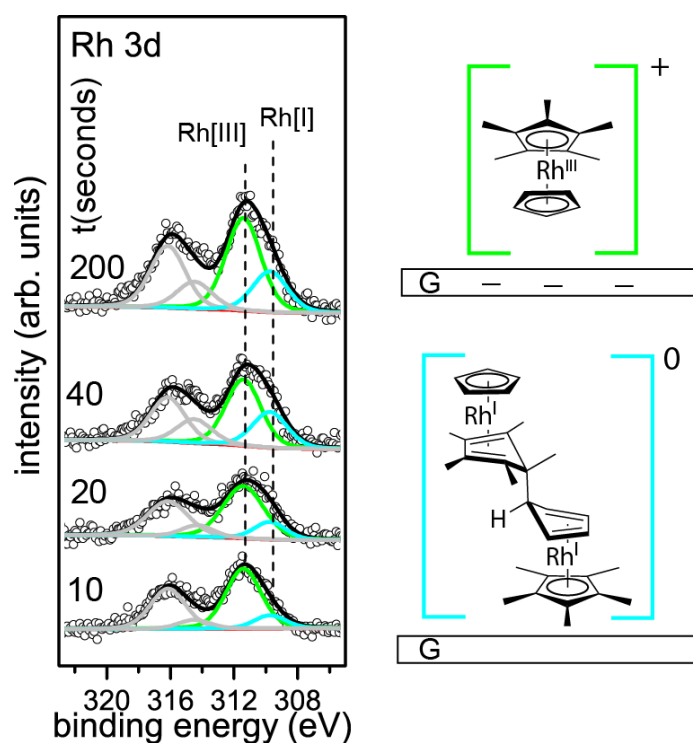
Figure 5.33: Evolution of Rh 3d emission upon deposition of [RhCp*Cp]$_2$ on graphene-on-quartz. The spectrum is deconvoluted to show the underlying emissions stemming from different species of Rh present on the surface. The blue lineshape corresponds to neutral Rh(I) and the green lineshape to positively charged Rh(III). On the right, schematic illustrations showing the monomeric cation (top) and the unreacted dimer (bottom) are drawn.

performed using a routine that preserves the intensity ratio and the energy difference between the Rh 3d$_{3/2}$ and Rh 3d$_{5/2}$ doublet. The Rh 3d$_{5/2}$ feature, which has the higher intensity of the two can be fit by using two Voigt profiles. The emission at BE = 309.8 eV (blue colour) is attributed to neutral [RhCp*Cp]$_2$ with the Rh atom having the oxidation number I, marked as Rh(I) in the spectra and the emission at BE = 311.4 eV (green colour) is attributed to the positively charged [RhCp*Cp]$^+$ monomer, with the Rh having the oxidation number III, marked as Rh(III) [128]. The neutral species arises from molecules that remain unreacted on the surface of the graphene layer or in multilayers, while the positively charged species corresponds to the molecules that each donated an electron to graphene.

Energy level alignment

The large decrease of the work function by $\Delta\Phi$ = 1.4 eV can be separated into two contributions, similar to the case of F_6TCNNQ adsorbed on graphene: (a) donation of electrons to the graphene layer that enter the CB of graphene, causing the E_F to shift upwards with respect to E_D, giving rise to the ΔE_F = 0.6 eV and (b) ID formed at the interface due to the formation of a (sub)monolayer that is partially populated with cations on top of the n-doped graphene layer, shifting E_{vac} and giving rise to ΔE_{vac} = 0.8 eV.
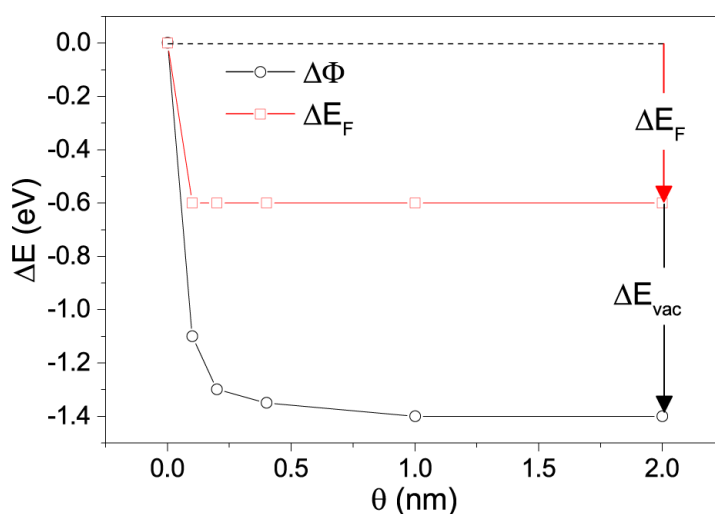
Figure 5.34: Work function shift ($\Delta\Phi$) and shift of the Fermi level (E_F) with respect to the Dirac point upon deposition of [RhCp*Cp]$_2$ on graphene-on-quartz (G/Qu). ΔE_F shows the change of the work function due to the shift of the Fermi level in the graphene layer due to the surface charge transfer doping of graphene and ΔE_{vac} shows the shift in the vacuum energy level, due to the formation of the interface dipole.

The $\Delta\Phi$ and ΔE_F after incremental deposition of [RhCp*Cp]$_2$ on G/Qu are shown in Fig. 5.34.

The associated shifts of the energy levels of graphene that give rise to the work function change are depicted in Fig. 5.35.

5.4.2 [RuCp*mes]$_2$ on graphene-on-quartz

The ruthenium-containing dimer [RuCp*mes]$_2$ has already been used to n-dope C_{60}, via a reaction where the molecule reacts with two C_{60} molecules,
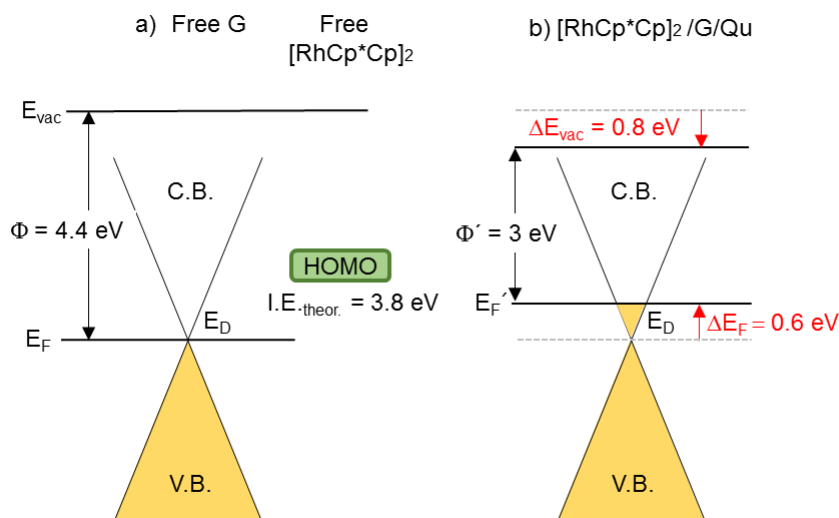
Figure 5.35: Energy level diagram of graphene-on-quartz (a) before and (b) after adsorption of [RhCp*Cp]$_2$.

converting to two cationic monomers [RuCp*mes]$^+$ and forming two C$_{60}$ anions. [130].

Valence electronic structure

Fig. 5.36 presents the UPS results upon sequential deposition of [RuCp*mes]$_2$ on G/Qu. A sequential decrease of the SECO onset is observed Fig. 5.36a, that translates to a work function decrease, $\Delta\Phi$ = -1.2 eV. Two new emissions are present near the E_F, as shown in Fig. 5.36b), with peak maxima at BE of 2.5 eV and 4.1 eV, that are attributed to emissions from the donor molecule. These emissions appear already at θ = 0.2 nm and increase in intensity up to θ = 1.6 nm. Taking a closer look at the low BE region (Fig. 5.36c), a new emission with a very weak intensity arises near E_F, in a very similar manner as [RhCp*Cp]$_2$. This feature disappears at higher θ, directly evidencing the interface character of this emission, when also taking into account that [RuCp*mes]$_2$ has a better sticking coefficient than [RhCp*Cp]$_2$ and the multilayers are stable, as will be also shown in the discussion of the core level spectra. The dip in the spectra at θ = 0.2 nm and 0.5 nm corresponds to E_D, that shifts away from E_F by ~ 0.6 eV.
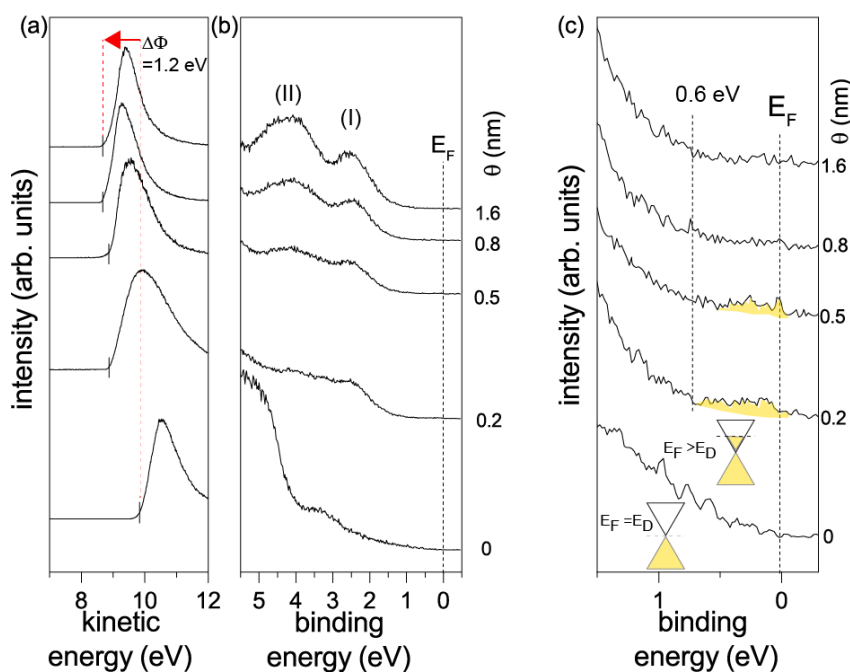
Figure 5.36:   a) SECO evolution and b) valence band evolution upon [RuCp*mes]$_2$ deposition. c) Zoom at low binding energy region showing the occupied conduction band of graphene. The insets show the position of the Dirac point E_D with respect to E_F.

Core level analysis

Fig. 5.37a) shows the evolution of the C 1s and Ru 3d core level spectra. The Ru 3d$_{3/2}$ state overlaps with the C 1s core level emissions. Following a consistent fitting routine, the emissions are deconvolved by taking a single Voigt function (red) for all the C 1s core level emissions arising from the molecule and an asymmetric Voigt profile for the C 1s core level of graphene, together with emissions coming from residual carbon resting on the surface of the graphene sheet after annealing in UHV (depicted by light grey). Fig. 5.37b) shows a zoom at the Ru 3d emission region. At θ = 0.2 nm, two emissions are observed at the Ru 3d. The emission at at BE = 282.2 eV is attributed to unreacted dimer on the surface, [Ru3d$_{5/2}$]^0. The second peak, at a higher BE = 281.1 eV arises from the reacted dimer that exists on the surface in a monomeric, cationic form, depicted by [Ru3d]$^+_{5/2}$ on the spectrum.
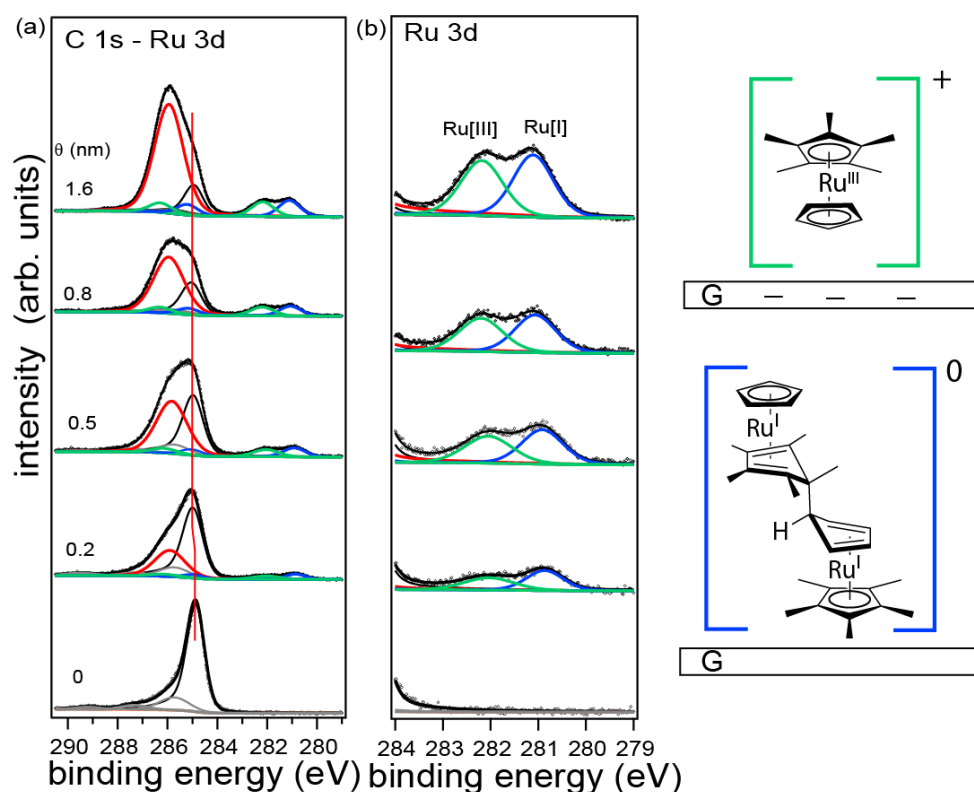
Figure 5.37: Evolution of the C 1s - Ru 3d core level region. The spectra are fitted in order to identify the underlying emissions.

Energy level alignment

As in the previous case, the large decrease of the work function by $\Delta\Phi = 1.2\,\text{eV}$ is decomposed into two contributions: $\Delta E_F = 0.6\,\text{eV}$, due to surface CT doping of the graphene sheet and $\Delta E_{vac} = 0.6\,\text{eV}$, due the formation of an interface dipole. The $\Delta\Phi$ and ΔE_F after incremental deposition of [RuCp*mes]$_2$ on G/Qu are shown in Fig. 5.38. The associated shifts of the energy levels of graphene that give rise to the work function change are depicted in Fig. 5.39.
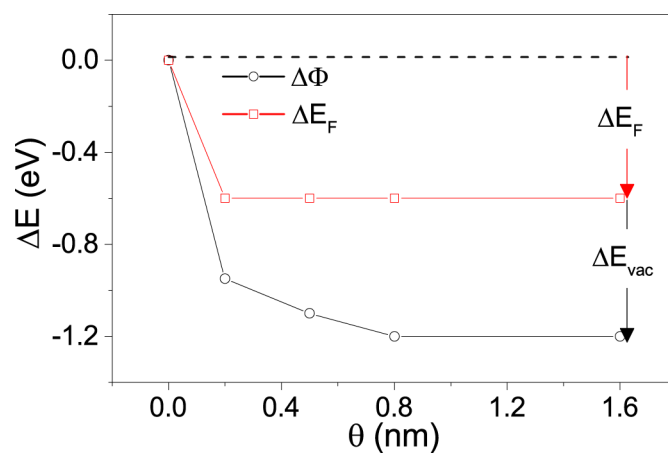
Figure 5.38: Work function shift ($\Delta\Phi$) and shift of the Dirac point E_D with respect to the Fermi level E_F upon deposition of [RuCp*mes]$_2$ on graphene-on-quartz (G/Qu). ΔE_F shows the contribution to the work function decrease induce by the band filling of the graphene by the surface-dopant and ΔE_{vac} shows the contribution of the vacuum level shift to the work function change, that is induced by an interface dipole forming at the interface.
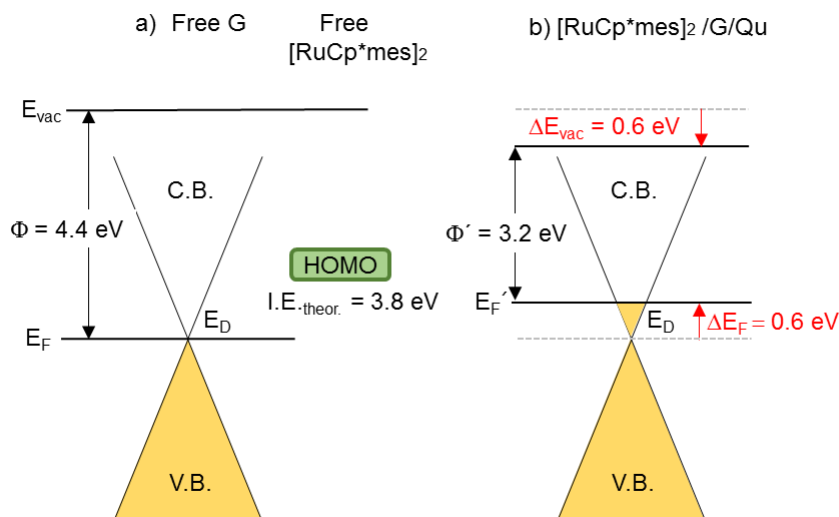
Figure 5.39: Energy level alignment diagram (a) before and (b) after contact between graphene-on-quartz (G/Qu) and [RuCp*mes]$_2$.

5.4.3   Conclusion

In this chapter it has been shown that [RhCp*Cp]$_2$ and [RuCp*mes]$_2$ act as strong molecular donors when deposited on G/Qu.

A work function reduction of $\Delta\Phi$ = 1.4 eV for the case of [RhCp*Cp]$_2$ was observed. This decrease could be explicitly decomposed into a contribution arising from n-type doping of the graphene sheet causing electrons to fill the conduction band and giving rise to a shift in E_F of 0.6 eV. The remainder of the work function decrease stems from the ID that builds up at the interface CT takes place. This ID translates into a downward shift of E_{vac} of 0.8 eV resulting to the final $\Delta\Phi$ = 1.4 eV, i.e., a final Φ for G/Qu of 3 eV.

From the Rh 3d spectra, two features that correspond to two different species of the donor molecule could be identified. A low BE, the emissions due to neutral dimeric [RhCp*Cp]$_2$ is evident and a higher BE emission corresponding to cationic [RhCp*Cp]$^+$. This clearly shows that indeed a CT occurs at the interface.

Regarding the C 1s features, a ΔE of the similar magnitude and in the same direction as the shift in the E_F is observed, verifying the rigid shift of the energy levels of graphene towards lower BE.

For the case of [RuCp*mes]$_2$ on G/Qu similar results were obtained. The work function reduction was $\Delta\Phi$=1.2 eV, decomposed to ΔE_F = 0.6 eV and ΔE_{vac} = 0.6 eV. In this case, the interface feature arising from the filled conduction band of graphene vanished at multilayer coverages, confirming that multilayer formation was possible.

From the Ru emissions, two electronic states corresponding to [RuCp*mes]$_2$ at lower BE and [RuCp*mes]$^+$ at higher BE were observed, confirming the CT occurring at the interface.

6 Summary and outlook

In this work, tailoring of the work function of graphene-on-quartz was successfully accomplished by using air stable molecular acceptor and donor materials to pre-cover the surface of graphene.

The interfaces formed between the studied COMs and graphene were investigated with complementary experimental techniques in order to study the electronic and structural properties of the COMs adsorbed on the graphene layer. UPS was performed to investigate the valence electronic structure and measure the work function induced by the graphene/COM interface formation. With XPS, the chemical state of the molecules was investigated, which was crucial in identifying the cases where interfacial CT occurred, and allowed localising the transferred charge in the molecules in these cases. Information on the film growth modes was obtained by observing overlayer coverage dependent attenuation of the photoelectron signals coming from the substrate. NEXAFS was used in order to monitor the orientation of the COMs on the graphene layer, allowing in some cases to correlate the work function change with the structural properties of the organic film. The results were crucial in identifying the interaction between the graphene layer and the adsorbed COMs, providing significant insight into the electronic and structural properties of the COM/graphene interfaces.

By using the molecular donors and acceptors, the work function of G/Qu could be reduced down to $\Phi = 3\,\mathrm{eV}$ and increased up to $\Phi = 5.7\,\mathrm{eV}$.

During the first experiments, which employed the strong molecular acceptor HATCN, the work function of graphene was incrementally increased by a value of $\Delta\Phi = 1.2\,\mathrm{eV}$, resulting in a final $\Phi = 5.7\,\mathrm{eV}$ for the modified G/Qu. Applying a simple model, the work function change was attributed to a CT occurring at the interface between HATCN and G/Qu, resulting in an ID that shifts E_{vac} upwards. This CT was manifested as an additional emission peak at lower BE in the N 1s core level spectra, and was attributed to a charge exchange between graphene and HATCN, as was consistently predicted from the theoretical calculations. Two different

orientations of HATCN were identified using NEXAFS providing an explanation of the sublinear work function increase via a density-dependent re-orientation of the molecules in the first monolayer. The potential to alter the molecular orientation in the first monolayer in contact with graphene by changing the molecular density can be crucial in the correct design of device architectures. HATCN was also deposited on HOPG and G/Cu, to investigate whether the "push-back" phenomenon was observed in graphitic surfaces. The occurrence of "push-back" was not observable with UPS for G/Qu, G/Cu and HOPG.

Deposition of the molecular acceptor F_6TCNNQ resulted in the incremental work function increase of $\Delta\Phi = 1\,\mathrm{eV}$ (G/Qu) and $\Delta\Phi = 1.3\,\mathrm{eV}$ (G/Cu). The CT mechanism was identified by new emission features in the valence level spectra close to the Fermi level, corresponding to the (partially) populated LUMO of the charged molecule and its relaxed HOMO. Further evidence of the CT occurring at the interface was manifested in the N 1s core level spectra as a feature at a lower BE with respect to the N 1s corresponding to neutral molecules. A difference was found between G/Qu and G/Cu in terms of the amount of molecules that were negatively charged. A higher amount of transferred electrons in the case of G/Cu resulted in a higher amount of charged molecules present in the first monolayer that was manifested as a higher work function increase. Furthermore, with the aid of theoretical simulations involving band structure and DOS calculations, the significant work function increase of 1 eV in the case of G/Qu could be identified as stemming from two contributions. Due to the CT occurring at the interface, the graphene layer becomes effectively p-doped. This p-doping lowers the Fermi level with respect to the Dirac point by 0.6 eV. Furthermore, the CT induced an interface dipole between the molecule and graphene, that further increased the work function of the system by 0.4 eV. In the case of F_6TCNNQ adsorbed on G/Cu, the simulations showed that the transferred charge originated from the Cu substrate and the doping level of graphene did not change and instead remained n-type. NEXAFS was performed for the G/Qu substrate, showing that the majority of molecules absorb flat-lying in the first monolayer, independent of the molecular density.

Lastly, the molecular donors [RhCp*Cp]$_2$ and [RuCp*mes]$_2$ were used to modify n-dope G/Qu. A significant work function decrease of $\Delta\Phi =$

1.4 eV was observed in the case of [RhCp*Cp]$_2$ and $\Delta\Phi = 1.2$ eV in the case of [RuCp*mes]$_2$. Using UPS and XPS, this effect was disentangled and assigned to (a) n-doping of the graphene layer, by electron donation from the respective metal atoms to the graphene conduction band, that shifts the Fermi level upwards with respect to the Dirac point and (b) an interface dipole that additionally shifts the vacuum level, leading to the final work function alterations. The mechanism leading to the electron donation was explained by a cleavage of the stable dimer into monomers when coming into contact with the graphene surface and the subsequent donation of electrons that turned the monomers into cations. The ability to lower the work function of graphene by as low as 1.4 eV, opens the possibility to use graphene as a cathode, as to facilitate electron injection.

Since the cost of synthesis of high quality and large area graphene sheets gets rapidly reduced due to lower manufacturing costs, it is expected that graphene will be increasingly used in electronic devices. Already in 2014 (IDTechEx report), various commercial applications were announced and the graphene industry showed an expansion with numerous investments. For the upcoming era of "graphene electronics", this work provides a readily applicable method for tailoring the work function of graphene in a non-covalent manner, by a suitable choice of molecular acceptors/donors, as to facilitate charge injection at interfaces between organic/graphene interfaces and consequently improve the efficiency and functionality of future graphene based organic (opto)electronic devices.

Abbreviations

This list contains all the abbreviations used in this work.

OLED	Organic light emitting diode
CNT	Carbon nanotube
OSC	Organic semiconductor
OPVC	Organic photovoltaic cell
COM	Conjugate organic molecule
XPS	X-ray photoelectron spectroscopy
UPS	Ultraviolet photoelectron spectroscopy
NEXAFS	Near edge X-Ray absorption fine structure spectroscopy
Qu	Quartz
Cu	Copper
G/Cu	Graphene-on-copper
G/Qu	Graphene-on-quartz
UHV	Ultra high vacuum
CT	Charge transfer
ID	Interface dipole
E_F	Fermi level energy
E_D	Dirac point energy
Φ	Work function
E_{vac}	Vacuum level energy
CVD	Chemical vapour deposition

$\rho(E)$	Density of states
GO	Graphene oxide
rGO	Reduced graphene oxide
IE	Ionization energy
EA	Electron affinity
HOMO	Highest occupied molecular orbital
LUMO	Lowest unoccupied molecular orbital
ELA	Energy level alignment
EA_{gas}	Electron affinity of molecules in gas phase
IE_{gas}	Ionization energy of molecules in gas phase
IE_{con}	Ionization energy of molecules in condensed phase
EA_{con}	Electron affinity of molecules in condensed phase
$E_{G,transport}$	Transport gap
$E_{G,gas}$	Energy gap of molecules in gas phase
FET	Field effect transistor
HIB	Hole injection barrier
EIB	Electron injection barrier
ETM	Electron transport material
EIB	Electron injection barrier
ETL	Electron transport layer
HTL	Hole transport layer
$h\nu$	photon energy
G	Graphene
E	Energy
μ	Dipole moment or electric dipole operator
ϵ	Dielectric constact
ϵ_0	Vacuum permittivity

ΔE	Energy level shift
ΔE_F	Energy shift of the Fermi level
ΔE_{vac}	Energy shift of the vacuum level
$\Delta \Phi$	Work function change
SAM	Self assembled monolayer
ν	Frequency
q	Elementary charge
Φ_d	Work function of electron analyser
Φ_s	Work function of sample
E_{kin}	Kinetic energy
E_b	Binding energy
VL	Valence level
VB	Valence band
CL	Core level
CLR	Core level region
VLR	Valence level region
CNL	Charge neutrality level
SECO	Secondary electron cut off
BE	Binding energy
EM	Electromagnetic
PES	Photoemission spectroscopy
V_{bias}	Potential applied between sample and analyser
Φ_{light}	Scalar potential of the incident electromagnetic radiation
$\mathbf{A}$	Vector potential of the incident electromagnetic radiation
I_{ext}	Total external emission current
$I^{int}(E_{kin}, h\upsilon, \boldsymbol{k})$	Internal photoelectron current
$T(E_{kin}, \boldsymbol{k})$	Transport function

$X(E_{kin}, \boldsymbol{k})$	Escape function
p	Momentum of electron
I_{sample}	Current generated in the sample during NEXAFS measurement
I_{mesh}	Current generated in the mesh during NEXAFS measurement
I_{Au}	Current generated in the Au foil during NEXAFS measurement
$E_{kin|E_F}$	Kinetic energy of the Fermi level
$E_{kin|HOMO_{onset}}$	Kinetic energy of the HOMO onset
E_{bound}	Bound electronic state
M_{if}	Transition matrix element
EDC	Energy distribution curve
w	Transition probability
$\boldsymbol{O}$	Final state orbital vector
$\boldsymbol{E}$	Electric field
δ	Angle between electric field direction and final state orbital vector
DOS	Density of states
DFT	Density functional theory
α	emission angle
QCM	Quartz crystal microbalance
d	Distance
Ψ_c	Angle with respect to horizontal of the analysis chamber in BEAR endstation
Θ_M	Incidence angle between incident light and sample surface plane
ψ_{inc}	Inclination angle between molecular plane and the plane of the substrate

ρ	Absorption coefficient
σ_x	Absorption cross section
θ	Nominal mass thickness, or coverage
C.B.	Conduction band
V.B.	Valence band
t	Time
N_{in}	Nitrogens located in the outer part of the molecule
N_{out}	Nitrogens located in the inner part of the molecule
E_{ads}	Adsorption energy
DCD	Differential charge density
LDOS	Local density of states

Bibliography

[1] K. S. Novoselov, A. K. Geim, S. V. Morozov, D. Jiang, Y. Zhang, S. V. Dubonos, I. V. Grigorieva, and A. A. Firsov, "Electric Field Effect in Atomically Thin Carbon Films," *Science*, vol. 306, pp. 666–669, Oct. 2004.

[2] K. S. Novoselov, A. K. Geim, S. V. Morozov, D. Jiang, M. I. Katsnelson, I. V. Grigorieva, S. V. Dubonos, and A. A. Firsov, "Two-dimensional gas of massless Dirac fermions in graphene," *Nature*, vol. 438, pp. 197–200, Nov. 2005.

[3] A. K. Geim and K. S. Novoselov, "The rise of graphene," *Nat Mater*, vol. 6, pp. 183–191, Mar. 2007.

[4] K. S. Novoselov, V. I. Fal'ko, L. Colombo, P. R. Gellert, M. G. Schwab, and K. Kim, "A roadmap for graphene," *Nature*, vol. 490, pp. 192–200, Oct. 2012.

[5] C. Lee, X. Wei, J. W. Kysar, and J. Hone, "Measurement of the Elastic Properties and Intrinsic Strength of Monolayer Graphene," *Science*, vol. 321, pp. 385–388, July 2008.

[6] R. R. Nair, P. Blake, A. N. Grigorenko, K. S. Novoselov, T. J. Booth, T. Stauber, N. M. R. Peres, and A. K. Geim, "Fine Structure Constant Defines Visual Transparency of Graphene," *Science*, vol. 320, pp. 1308–1308, June 2008.

[7] A. Reina, X. Jia, J. Ho, D. Nezich, H. Son, V. Bulovic, M. S. Dresselhaus, and J. Kong, "Large Area, Few-Layer Graphene Films on Arbitrary Substrates by Chemical Vapor Deposition," *Nano Letters*, vol. 9, pp. 30–35, Jan. 2009.

[8] A. A. Balandin, S. Ghosh, W. Bao, I. Calizo, D. Teweldebrhan, F. Miao, and C. N. Lau, "Superior Thermal Conductivity of Single-Layer Graphene," *Nano Lett.*, vol. 8, pp. 902–907, Mar. 2008.

[9] T.-H. Han, Y. Lee, M.-R. Choi, S.-H. Woo, S.-H. Bae, B. H. Hong, J.-H. Ahn, and T.-W. Lee, "Extremely efficient flexible organic light-emitting diodes with modified graphene anode," *Nat Photon*, vol. 6, pp. 105–110, Feb. 2012.

[10] F. Schedin, A. K. Geim, S. V. Morozov, E. W. Hill, P. Blake, M. I. Katsnelson, and K. S. Novoselov, "Detection of individual gas molecules adsorbed on

graphene," *Nat Mater*, vol. 6, pp. 652–655, Sept. 2007.

[11] E. Yoo, J. Kim, E. Hosono, H.-s. Zhou, T. Kudo, and I. Honma, "Large Reversible Li Storage of Graphene Nanosheet Families for Use in Rechargeable Lithium Ion Batteries," *Nano Lett.*, vol. 8, pp. 2277–2282, Aug. 2008.

[12] X. Wang, L. Zhi, and K. Müllen, "Transparent, conductive graphene electrodes for dye-sensitized solar cells," *Nano Lett.*, vol. 8, pp. 323–327, Jan. 2008. WOS:000252257700057.

[13] S. Bae, H. Kim, Y. Lee, X. Xu, J.-S. Park, Y. Zheng, J. Balakrishnan, T. Lei, H. Ri Kim, Y. I. Song, Y.-J. Kim, K. S. Kim, B. Özyilmaz, J.-H. Ahn, and S. Hong, B. H.and Iijima, "Roll-to-roll production of 30-inch graphene films for transparent electrodes," *Nat Nano*, vol. 5, pp. 574–578, Aug. 2010.

[14] L. Schmidt-Mende, A. Fechtenkätter, K. Müllen, E. Moons, R. H. Friend, and J. D. MacKenzie, "Self-Organized Discotic Liquid Crystals for High-Efficiency Organic Photovoltaics," *Science*, vol. 293, pp. 1119–1122, Aug. 2001.

[15] U. Bach, D. Lupo, P. Comte, J. E. Moser, F. Weissörtel, J. Salbeck, H. Spreitzer, and M. Grätzel, "Solid-state dye-sensitized mesoporous TiO2 solar cells with high photon-to-electron conversion efficiencies," *Nature*, vol. 395, pp. 583–585, Oct. 1998.

[16] S.-I. Na, S.-S. Kim, J. Jo, and D.-Y. Kim, "Efficient and Flexible ITO-Free Organic Solar Cells Using Highly Conductive Polymer Anodes," *Adv. Mater.*, vol. 20, pp. 4061–4067, Nov. 2008.

[17] Z. Wu, Z. Chen, X. Du, J. M. Logan, J. Sippel, M. Nikolou, K. Kamaras, J. R. Reynolds, D. B. Tanner, A. F. Hebard, and A. G. Rinzler, "Transparent, Conductive Carbon Nanotube Films," *Science*, vol. 305, pp. 1273–1276, Aug. 2004.

[18] E. Vitoratos, S. Sakkopoulos, E. Dalas, N. Paliatsas, D. Karageorgopoulos, F. Petraki, S. Kennou, and S. A. Choulis, "Thermal degradation mechanisms of PEDOT:PSS," *Organic Electronics*, vol. 10, pp. 61–66, Feb. 2009.

[19] B. Dan, G. C. Irvin, and M. Pasquali, "Continuous and Scalable Fabrication of Transparent Conducting Carbon Nanotube Films," *ACS Nano*, vol. 3, pp. 835–843, Apr. 2009.

[20] X. Li, W. Cai, J. An, S. Kim, J. Nah, D. Yang, R. Piner, A. Velamakanni, I. Jung, E. Tutuc, S. K. Banerjee, L. Colombo, and R. S. Ruoff, "Large-Area Synthesis of High-Quality and Uniform Graphene Films on Copper Foils," *Science*, vol. 324, pp. 1312–1314, June 2009.

[21] X. Li, Y. Zhu, W. Cai, M. Borysiak, B. Han, D. Chen, R. D. Piner, L. Colombo, and R. S. Ruoff, "Transfer of Large-Area Graphene Films for High-Performance Transparent Conductive Electrodes," *Nano Letters*, vol. 9, pp. 4359–4363, Dec. 2009.

[22] N. Koch, S. Duhm, J. Rabe, A. Vollmer, and R. Johnson, "Optimized Hole Injection with Strong Electron Acceptors at Organic-Metal Interfaces," *Physical Review Letters*, vol. 95, Nov. 2005.

[23] E. L. Wolf, *Graphene: A New Paradigm in Condensed Matter and Device Physics*. Oxford University Press, Nov. 2013.

[24] A. H. Castro Neto, F. Guinea, N. M. R. Peres, K. S. Novoselov, and A. K. Geim, "The electronic properties of graphene," *Rev. Mod. Phys.*, vol. 81, pp. 109–162, Jan. 2009.

[25] P. R. Wallace, "The Band Theory of Graphite," *Phys. Rev.*, vol. 71, pp. 622–634, May 1947.

[26] D. P. DiVincenzo and E. J. Mele, "Self-consistent effective-mass theory for intralayer screening in graphite intercalation compounds," *Phys. Rev. B*, vol. 29, pp. 1685–1694, Feb. 1984.

[27] X. Du, I. Skachko, A. Barker, and E. Y. Andrei, "Approaching ballistic transport in suspended graphene," *Nat Nano*, vol. 3, pp. 491–495, Aug. 2008.

[28] P. Blake, P. D. Brimicombe, R. R. Nair, T. J. Booth, D. Jiang, F. Schedin, L. A. Ponomarenko, S. V. Morozov, H. F. Gleeson, E. W. Hill, A. K. Geim, and K. S. Novoselov, "Graphene-Based Liquid Crystal Device," *Nano Lett.*, vol. 8, pp. 1704–1708, June 2008.

[29] Y. Hernandez, V. Nicolosi, M. Lotya, F. M. Blighe, Z. Sun, S. De, I. T. McGovern, B. Holland, M. Byrne, Y. K. Gun'Ko, J. J. Boland, P. Niraj, G. Duesberg, S. Krishnamurthy, R. Goodhue, J. Hutchison, V. Scardaci, A. C. Ferrari, and J. N. Coleman, "High-yield production of graphene by liquid-phase exfoliation of graphite," *Nat Nano*, vol. 3, pp. 563–568, Sept. 2008.

[30] H. C. Schniepp, J.-L. Li, M. J. McAllister, H. Sai, M. Herrera-Alonso, D. H. Adamson, R. K. Prud'homme, R. Car, D. A. Saville, and I. A. Aksay, "Functionalized Single Graphene Sheets Derived from Splitting Graphite Oxide," *J. Phys. Chem. B*, vol. 110, pp. 8535–8539, May 2006.

[31] T. Ohta, A. Bostwick, T. Seyller, K. Horn, and E. Rotenberg, "Controlling the Electronic Structure of Bilayer Graphene," *Science*, vol. 313, pp. 951–954, Aug. 2006.

[32] C. Virojanadara, M. Syvajarvi, R. Yakimova, L. I. Johansson, A. A. Za-

kharov, and T. Balasubramanian, "Homogeneous large-area graphene layer growth on 6h-SiC(0001)," *Phys. Rev. B*, vol. 78, p. 245403, Dec. 2008.

[33] S. Stankovich, D. A. A. Dikin, G. H. B. Dommett, K. M. Kohlhaas, E. J. Zimney, E. A. Stach, R. D. Piner, S. T. Nguyen, and R. S. Ruoff, "Graphene-based composite materials," *Nature*, vol. 442, pp. 282–286, July 2006.

[34] G. Eda, G. Fanchini, and M. Chhowalla, "Large-area ultrathin films of reduced graphene oxide as a transparent and flexible electronic material," *Nat Nano*, vol. 3, pp. 270–274, May 2008.

[35] Y. Hernandez, M. Lotya, D. Rickard, S. D. Bergin, and J. N. Coleman, "Measurement of Multicomponent Solubility Parameters for Graphene Facilitates Solvent Discovery," *Langmuir*, vol. 26, pp. 3208–3213, Mar. 2010.

[36] G. Eda and M. Chhowalla, "Chemically Derived Graphene Oxide: Towards Large-Area Thin-Film Electronics and Optoelectronics," *Adv. Mater.*, vol. 22, pp. 2392–2415, June 2010.

[37] C. Mattevi, G. Eda, S. Agnoli, S. Miller, K. A. Mkhoyan, O. Celik, D. Mastrogiovanni, G. Granozzi, E. Garfunkel, and M. Chhowalla, "Evolution of Electrical, Chemical, and Structural Properties of Transparent and Conducting Chemically Derived Graphene Thin Films," *Adv. Funct. Mater.*, vol. 19, pp. 2577–2583, Aug. 2009.

[38] W. A. de Heer, C. Berger, X. Wu, P. N. First, E. H. Conrad, X. Li, T. Li, M. Sprinkle, J. Hass, M. L. Sadowski, M. Potemski, and G. Martinez, "Epitaxial graphene," *Solid State Communications*, vol. 143, pp. 92–100, July 2007.

[39] K. S. Kim, Y. Zhao, H. Jang, S. Y. Lee, J. M. Kim, K. S. Kim, J.-H. Ahn, P. Kim, J.-Y. Choi, and B. H. Hong, "Large-scale pattern growth of graphene films for stretchable transparent electrodes," *Nature*, vol. 457, pp. 706–710, Feb. 2009.

[40] S.-Y. Kwon, C. V. Ciobanu, V. Petrova, V. B. Shenoy, J. Bareo, V. Gambin, I. Petrov, and S. Kodambaka, "Growth of Semiconducting Graphene on Palladium," *Nano Lett.*, vol. 9, pp. 3985–3990, Dec. 2009.

[41] P. W. Sutter, J.-I. Flege, and E. A. Sutter, "Epitaxial graphene on ruthenium," *Nat Mater*, vol. 7, pp. 406–411, May 2008.

[42] J. Coraux, A. T. Ndiaye, C. Busse, and T. Michely, "Structural Coherency of Graphene on Ir(111)," *Nano Lett.*, vol. 8, pp. 565–570, Feb. 2008.

[43] R. Munoz and C. Gomez-Aleixandre, "Review of CVD Synthesis of Graphene," *Chem. Vap. Deposition*, vol. 19, pp. 297–322, Dec. 2013.

[44] G. A. Lopez and E. J. Mittemeijer, "The solubility of C in solid Cu," *Scripta*

Materialia, vol. 51, pp. 1–5, July 2004.

[45] P. Sutter, M. S. Hybertsen, J. T. Sadowski, and E. Sutter, "Electronic Structure of Few-Layer Epitaxial Graphene on Ru(0001)," *Nano Lett.*, vol. 9, pp. 2654–2660, July 2009.

[46] V. Georgakilas, M. Otyepka, A. B. Bourlinos, V. Chandra, N. Kim, K. C. Kemp, P. Hobza, R. Zboril, and K. S. Kim, "Functionalization of Graphene: Covalent and Non-Covalent Approaches, Derivatives and Applications," *Chemical Reviews*, vol. 112, pp. 6156–6214, Nov. 2012.

[47] H. Y. Mao, Y. H. Lu, J. D. Lin, S. Zhong, A. T. S. Wee, and W. Chen, "Manipulating the electronic and chemical properties of graphene via molecular functionalization," *Progress in Surface Science*, vol. 88, pp. 132–159, May 2013.

[48] S. Chen, L. Brown, M. Levendorf, W. Cai, S.-Y. Ju, J. Edgeworth, X. Li, C. W. Magnuson, A. Velamakanni, R. D. Piner, J. Kang, J. Park, and R. S. Ruoff, "Oxidation Resistance of Graphene-Coated Cu and Cu/Ni Alloy," *ACS Nano*, vol. 5, pp. 1321–1327, Feb. 2011.

[49] L. Yan, Y. B. Zheng, F. Zhao, S. Li, X. Gao, B. Xu, P. S. Weiss, and Y. Zhao, "Chemistry and physics of a single atomic layer: strategies and challenges for functionalization of graphene and graphene-based materials," *Chem. Soc. Rev.*, vol. 41, pp. 97–114, Dec. 2011.

[50] S. L. Wong, H. Huang, Y. Wang, L. Cao, D. Qi, I. Santoso, W. Chen, and A. T. S. Wee, "Quasi-Free-Standing Epitaxial Graphene on SiC (0001) by Fluorine Intercalation from a Molecular Source," *ACS Nano*, vol. 5, pp. 7662–7668, Sept. 2011.

[51] R. R. Nair, W. Ren, R. Jalil, I. Riaz, V. G. Kravets, L. Britnell, P. Blake, F. Schedin, A. S. Mayorov, S. Yuan, M. I. Katsnelson, H.-M. Cheng, W. Strupinski, L. G. Bulusheva, A. V. Okotrub, I. V. Grigorieva, A. N. Grigorenko, K. S. Novoselov, and A. K. Geim, "Fluorographene: A Two-Dimensional Counterpart of Teflon," *Small*, vol. 6, pp. 2877–2884, Dec. 2010.

[52] B. G. Choi, H. Park, M. H. Yang, Y. M. Jung, S. Y. Lee, W. H. Hong, and T. J. Park, "Microwave-assisted synthesis of highly water-soluble graphene towards electrical DNA sensor," *Nanoscale*, vol. 2, pp. 2692–2697, Dec. 2010.

[53] N. Mohanty and V. Berry, "Graphene-Based Single-Bacterium Resolution Biodevice and DNA Transistor: Interfacing Graphene Derivatives with Nanoscale and Microscale Biocomponents," *Nano Lett.*, vol. 8, pp. 4469–4476, Dec. 2008.

[54] S. Niyogi, E. Bekyarova, M. E. Itkis, J. L. McWilliams, M. A. Hamon, and R. C. Haddon, "Solution Properties of Graphite and Graphene," *J. Am. Chem. Soc.*, vol. 128, pp. 7720–7721, June 2006.

[55] H. Liu, Y. Liu, and D. Zhu, "Chemical doping of graphene," *J. Mater. Chem.*, vol. 21, pp. 3335–3345, Feb. 2011.

[56] W. Chen, D. Qi, X. Gao, and A. T. S. Wee, "Surface transfer doping of semi-conductors," *Progress in Surface Science*, vol. 84, pp. 279–321, Sept. 2009.

[57] X. Dong, Y. Shi, Y. Zhao, D. Chen, J. Ye, Y. Yao, F. Gao, Z. Ni, T. Yu, Z. Shen, Y. Huang, P. Chen, and L.-J. Li, "Symmetry Breaking of Graphene Mono-layers by Molecular Decoration," *Phys. Rev. Lett.*, vol. 102, p. 135501, Mar. 2009.

[58] Y. Liu, X. Dong, and P. Chen, "Biological and chemical sensors based on graphene materials," *Chem. Soc. Rev.*, vol. 41, pp. 2283–2307, Feb. 2012.

[59] Y. Wang, Z. Li, J. Wang, J. Li, and Y. Lin, "Graphene and graphene oxide: biofunctionalization and applications in biotechnology," *Trends Biotechnol.*, vol. 29, pp. 205–212, May 2011.

[60] W. R. Salaneck, K. Seki, A. Kahn, and J.-J. Pireaux, *Conjugated Polymer And Molecular Interfaces: Science And Technology For Photonic And Optoelectronic Application*. CRC Press, Oct. 2001.

[61] H. Ishii, K. Sugiyama, E. Ito, and K. Seki, "Energy level alignment and in-terfacial electronic structures at organic/metal and organic/organic inter-faces," *Advanced Materials*, vol. 11, no. 8, pp. 605–625, 1999.

[62] M. Schwoerer and H. C. Wolf, "Organic Molecular Solids," in *Organic Molecular Solids*, pp. i–xi, Wiley-VCH Verlag GmbH, 2006.

[63] R. Schlesinger, Y. Xu, O. T. Hofmann, S. Winkler, J. Frisch, J. Niederhausen, A. Vollmer, S. Blumstengel, F. Henneberger, P. Rinke, M. Scheffler, and N. Koch, "Controlling the work function of ZnO and the energy-level align-ment at the interface to organic semiconductors with a molecular electron acceptor," *Phys. Rev. B*, vol. 87, p. 155311, Apr. 2013.

[64] S. Winkler, J. Frisch, R. Schlesinger, M. Oehzelt, R. Rieger, J. Räder, J. P. Rabe, K. Müllen, and N. Koch, "The Impact of Local Work Function Variations on Fermi Level Pinning of Organic Semiconductors," *J. Phys. Chem. C*, vol. 117, pp. 22285–22289, Oct. 2013.

[65] C. Christodoulou, A. Giannakopoulos, M. V. Nardi, G. Ligorio, M. Oe-hzelt, L. Chen, L. Pasquali, M. Timpel, A. Giglia, S. Nannarone, P. Nor-man, M. Linares, K. Parvez, K. Mllen, D. Beljonne, and N. Koch, "Tuning

the Work Function of Graphene-on-Quartz with a High Weight Molecular Acceptor," *J. Phys. Chem. C*, vol. 118, pp. 4784–4790, Mar. 2014.

[66] M. Castellani, S. Winkler, B. Bröker, M. Baumgarten, K. Müllen, and N. Koch, "Work function increase of transparent conductive electrodes by solution processed electron acceptor molecular monolayers," *Appl. Phys. A*, vol. 114, pp. 291–295, Feb. 2014.

[67] B. Bröker, B.ker, R.-P. Blum, J. Frisch, A. Vollmer, O. T. Hofmann, R. Rieger, K. Mullen, J. P. Rabe, E. Zojer, and N. Koch, "Gold work function reduction by 2.2 eV with an air-stable molecular donor layer," *Applied Physics Letters*, vol. 93, no. 24, p. 243303, 2008.

[68] W. Gao and A. Kahn, "Controlled p-doping of zinc phthalocyanine by co-evaporation with tetrafluorotetracyanoquinodimethane: A direct and inverse photoemission study," *Applied Physics Letters*, vol. 79, pp. 4040–4042, Dec. 2001.

[69] H. Mendez, G. Heimel, A. Opitz, K. Sauer, P. Barkowski, M. Oehzelt, J. Soeda, T. Okamoto, J. Takeya, J.-B. Arlin, J.-Y. Balandier, Y. Geerts, N. Koch, and I. Salzmann, "Doping of Organic Semiconductors: Impact of Dopant Strength and Electronic Coupling," *Angew. Chem. Int. Ed.*, vol. 52, pp. 7751–7755, July 2013.

[70] W. Schottky, "Halbleitertheorie der Sperrschicht," *Naturwissenschaften*, vol. 26, pp. 843–843, Dec. 1938.

[71] I. G. Hill, A. Rajagopal, A. Kahn, and Y. Hu, "Molecular level alignment at organic semiconductor-metal interfaces," *Applied Physics Letters*, vol. 73, no. 5, pp. 662–664, 1998.

[72] P. S. Bagus, V. Staemmler, and C. Wöll, "Exchangelike Effects for Closed-Shell Adsorbates: Interface Dipole and Work Function," *Phys. Rev. Lett.*, vol. 89, p. 096104, Aug. 2002.

[73] X. Crispin, V. Geskin, A. Crispin, J. Cornil, R. Lazzaroni, W. R. Salaneck, and J.-L. Bredas, "Characterization of the Interface Dipole at Organic/ Metal Interfaces," *J. Am. Chem. Soc.*, vol. 124, pp. 8131–8141, July 2002.

[74] A. Kahn, N. Koch, and W. Gao, "Electronic structure and electrical properties of interfaces between metals and -conjugated molecular films," *Journal of Polymer Science Part B: Polymer Physics*, vol. 41, no. 21, pp. 2529–2548, 2003.

[75] N. D. Lang and W. Kohn, "Theory of Metal Surfaces: Work Function," *Phys. Rev. B*, vol. 3, pp. 1215–1223, Feb. 1971.

[76] P. S. Bagus, K. Hermann, and C. Wöll, "The interaction of C6h6 and C6h12 with noble metal surfaces: Electronic level alignment and the origin of the interface dipole," *The Journal of Chemical Physics*, vol. 123, p. 184109, Nov. 2005.

[77] L. Chai, R. T. White, M. T. Greiner, and Z. H. Lu, "Experimental demonstration of the universal energy level alignment rule at oxide/organic semiconductor interfaces," *Phys. Rev. B*, vol. 89, p. 035202, Jan. 2014.

[78] M. T. Greiner, M. G. Helander, W.-M. Tang, Z.-B. Wang, J. Qiu, and Z.-H. Lu, "Universal energy-level alignment of molecules on metal oxides," *Nat Mater*, vol. 11, pp. 76–81, Jan. 2012.

[79] N. Koch, "Electronic structure of interfaces with conjugated organic materials," *physica status solidi (RRL) Rapid Research Letters*, vol. 6, no. 7, pp. 277–293, 2012.

[80] I. G. Hill, D. Milliron, J. Schwartz, and A. Kahn, "Organic semiconductor interfaces: electronic structure and transport properties," *Applied Surface Science*, vol. 166, pp. 354–362, Oct. 2000.

[81] N. Koch and A. Vollmer, "Electrode-molecular semiconductor contacts: Work-function-dependent hole injection barriers versus Fermi-level pinning," *Applied Physics Letters*, vol. 89, pp. 162107–162107–3, Oct. 2006.

[82] S. Rentenberger, A. Vollmer, E. Zojer, R. Schennach, and N. Koch, "UV/ozone treated Au for air-stable, low hole injection barrier electrodes in organic electronics," *Journal of Applied Physics*, vol. 100, pp. 053701–053701–6, Sept. 2006.

[83] M. Fahlman, A. Crispin, X. Crispin, S. K. M. Henze, M. P. d. Jong, W. Osikowicz, C. Tengstedt, and W. R. Salaneck, "Electronic structure of hybrid interfaces for polymer-based electronics," *J. Phys.: Condens. Matter*, vol. 19, p. 183202, May 2007.

[84] M. Bokdam, D. Cakir, and G. Brocks, "Fermi level pinning by integer charge transfer at electrode-organic semiconductor interfaces," *Applied Physics Letters*, vol. 98, p. 113303, Mar. 2011.

[85] J. Hwang, E.-G. Kim, J. Liu, J.-L. Brdas, A. Duggal, and A. Kahn, "Photoelectron Spectroscopic Study of the Electronic Band Structure of Polyfluorene and Fluorene-Arylamine Copolymers at Interfaces," *J. Phys. Chem. C*, vol. 111, pp. 1378–1384, Jan. 2007.

[86] S. Winkler, J. Frisch, P. Amsalem, S. Krause, M. Timpel, M. Stolte, F. Würthner, and N. Koch, "Impact of Molecular Dipole Moments on Fermi

Level Pinning in Thin Films," *J. Phys. Chem. C*, vol. 118, pp. 11731–11737, June 2014.

[87] J. Frisch, M. Herder, P. Herrmann, G. Heimel, S. Hecht, and N. Koch, "Photoinduced reversible changes in the electronic structure of photochromic diarylethene films," *Appl. Phys. A*, vol. 113, pp. 1–4, Oct. 2013.

[88] J. Niederhausen, P. Amsalem, J. Frisch, A. Wilke, A. Vollmer, R. Rieger, K. Müllen, J. P. Rabe, and N. Koch, "Tuning hole-injection barriers at organic/metal interfaces exploiting the orientation of a molecular acceptor interlayer," *Phys. Rev. B*, vol. 84, p. 165302, Oct. 2011.

[89] P. Amsalem, J. Niederhausen, J. Frisch, A. Wilke, B. Bröker, A. Vollmer, R. Rieger, K. Müllen, J. P. Rabe, and N. Koch, "Metal-to-Acceptor Charge Transfer through a Molecular Spacer Layer," *The Journal of Physical Chemistry C*, vol. 115, pp. 17503–17507, Sept. 2011.

[90] B. de Boer, A. Hadipour, M. M. Mandoc, T. van Woudenbergh, and P. W. M. Blom, "Tuning of Metal Work Functions with Self-Assembled Monolayers," *Adv. Mater.*, vol. 17, pp. 621–625, Mar. 2005.

[91] S. F. J. Appleyard, S. R. Day, R. D. Pickford, and M. R. Willis, "Organic electroluminescent devices: enhanced carrier injection using SAM derivatized ITO electrodes," *J. Mater. Chem.*, vol. 10, pp. 169–173, Jan. 2000.

[92] J. Topping, "On the Mutual Potential Energy of a Plane Network of Doublets," *Proc. R. Soc. Lond. A*, vol. 114, pp. 67–72, Feb. 1927.

[93] A. Natan, L. Kronik, H. Haick, and R. T. Tung, "Electrostatic Properties of Ideal and Non-ideal Polar Organic Monolayers: Implications for Electronic Devices," *Adv. Mater.*, vol. 19, pp. 4103–4117, Dec. 2007.

[94] P. J. Hotchkiss, S. C. Jones, S. A. Paniagua, A. Sharma, B. Kippelen, N. R. Armstrong, and S. R. Marder, "The Modification of Indium Tin Oxide with Phosphonic Acids: Mechanism of Binding, Tuning of Surface Properties, and Potential for Use in Organic Electronic Applications," *Acc. Chem. Res.*, vol. 45, pp. 337–346, Mar. 2012.

[95] S. M. Sze, *Semiconductor devices, physics and technology*. Wiley, Apr. 1985.

[96] J. Ristein, "Surface transfer doping of diamond," *J. Phys. D: Appl. Phys.*, vol. 39, p. R71, Feb. 2006.

[97] P. Strobel, M. Riedel, J. Ristein, and L. Ley, "Surface transfer doping of diamond," *Nature*, vol. 430, pp. 439–441, July 2004.

[98] H. Lüth, *Solid Surfaces, Interfaces and Thin Films*. Springer Berlin Heidelberg, Sept. 2010.

[99] V. Chakrapani, J. C. Angus, A. B. Anderson, S. D. Wolter, B. R. Stoner, and G. U. Sumanasekera, "Charge Transfer Equilibria Between Diamond and an Aqueous Oxygen Electrochemical Redox Couple," *Science*, vol. 318, pp. 1424–1430, Nov. 2007.

[100] W. Chen, S. Chen, D. C. Qi, X. Y. Gao, and A. T. S. Wee, "Surface Transfer p-Type Doping of Epitaxial Graphene," *J. Am. Chem. Soc.*, vol. 129, pp. 10418–10422, Aug. 2007.

[101] S. Pisana, M. Lazzeri, C. Casiraghi, K. S. Novoselov, A. K. Geim, A. C. Ferrari, and F. Mauri, "Breakdown of the adiabatic BornOppenheimer approximation in graphene," *Nat Mater*, vol. 6, pp. 198–201, Mar. 2007.

[102] H. Sirringhaus, P. J. Brown, R. H. Friend, M. M. Nielsen, K. Bechgaard, B. M. W. Langeveld-Voss, A. J. H. Spiering, R. a. J. Janssen, E. W. Meijer, P. Herwig, and D. M. de Leeuw, "Two-dimensional charge transport in self-organized, high-mobility conjugated polymers," *Nature*, vol. 401, pp. 685–688, Oct. 1999.

[103] N. Koch, A. Elschner, J. Schwartz, and A. Kahn, "Organic molecular films on gold versus conducting polymer: Influence of injection barrier height and morphology on current/voltage characteristics," *Applied Physics Letters*, vol. 82, pp. 2281–2283, Apr. 2003.

[104] J. A. Venables, G. D. T. Spiller, and M. Hanbucken, "Nucleation and growth of thin films," *Rep. Prog. Phys.*, vol. 47, p. 399, Apr. 1984.

[105] G. Witte and C. Wöll, "Growth of aromatic molecules on solid substrates for applications in organic electronics," *Journal of Materials Research*, vol. 19, pp. 1889–1916, July 2004.

[106] D. E. Hooks, T. Fritz, and M. D. Ward, "Epitaxy and Molecular Organization on Solid Substrates," *Adv. Mater.*, vol. 13, pp. 227–241, Feb. 2001.

[107] G. Hähner, "Near edge X-ray absorption fine structure spectroscopy as a tool to probe electronic and structural properties of thin organic films and liquids," *Chemical Society Reviews*, vol. 35, no. 12, p. 1244, 2006.

[108] A. Einstein, "ber einen die Erzeugung und Verwandlung des Lichtes betreffenden heuristischen Gesichtspunkt," *Ann. Phys.*, vol. 322, pp. 132–148, Jan. 1905.

[109] H. Hertz, "Ueber einen Einfluss des ultravioletten Lichtes auf die electrische Entladung," *Ann. Phys.*, vol. 267, pp. 983–1000, Jan. 1887.

[110] S. H"ufner, *Photoelectron Spectroscopy: Principles and Applications*. Springer Science & Business Media, Apr. 2003.

[111] P. J. Cumpson and M. P. Seah, "Elastic Scattering Corrections in AES and XPS. II. Estimating Attenuation Lengths and Conditions Required for their Valid Use in Overlayer/Substrate Experiments," *Surface and Interface Analysis*, vol. 25, no. 6, pp. 430–446, 1997.

[112] W. R. Salaneck, C. B. Duke, W. Eberhardt, E. W. Plummer, and H. J. Freund, "Temperature-Dependent Ultraviolet Photoemission Linewidths of Molecular Solids: Isopropyl Benzene," *Phys. Rev. Lett.*, vol. 45, pp. 280–283, July 1980.

[113] J. Braun, "The theory of angle-resolved ultraviolet photoemission and its applications to ordered materials," *Rep. Prog. Phys.*, vol. 59, p. 1267, Oct. 1996.

[114] G. Borstel, "Theoretical aspects of photoemission," *Applied Physics A*, vol. 38, no. 3, pp. 193–204, 1985.

[115] C. N. Berglund and W. E. Spicer, "Photoemission Studies of Copper and Silver: Theory," *Phys. Rev.*, vol. 136, pp. A1030–A1044, Nov. 1964.

[116] J. Küppers and G. Ertl, *Low energy electrons and surface chemistry*. VCH Weinheim, 1985.

[117] S. Hüfner, S. Schmidt, and F. Reinert, "Photoelectron spectroscopy : An overview," *Nuclear Instruments and Methods in Physics Research Section A: Accelerators, Spectrometers, Detectors and Associated Equipment*, vol. 547, pp. 8–23, July 2005.

[118] N. Koch, N. Ueno, and A. T. S. Wee, eds., *The Molecule-Metal Interface*. Wiley-VCH, 2014.

[119] J. Sthr, *NEXAFS Spectroscopy*. Springer Series in Surface Sciences, Springer, 1992.

[120] B. Bröker, O. T. Hofmann, G. M. Rangger, P. Frank, R.-P. Blum, R. Rieger, L. Venema, A. Vollmer, K. Müllen, J. P. Rabe, A. Winkler, P. Rudolf, E. Zojer, and N. Koch, "Density-Dependent Reorientation and Rehybridization of Chemisorbed Conjugated Molecules for Controlling Interface Electronic Structure," *Physical Review Letters*, vol. 104, June 2010.

[121] H. Glowatzki, B. Bröker, R.-P. Blum, O. T. Hofmann, A. Vollmer, R. Rieger, K. Müllen, E. Zojer, J. P. Rabe, and N. Koch, ""Soft" Metallic Contact to Isolated C60 Molecules," *Nano Lett.*, vol. 8, pp. 3825–3829, Nov. 2008.

[122] G. M. Rangger, O. T. Hofmann, L. Romaner, G. Heimel, B. Bröker, R.-P. Blum, R. L. Johnson, N. Koch, and E. Zojer, "F4tcnq on Cu, Ag, and Au as prototypical example for a strong organic acceptor on coinage metals,"

Phys. Rev. B, vol. 79, p. 165306, Apr. 2009.

[123] J.-S. Kim, S.-K. Lee, H.-J. Lee, and D.-Y. Noh, "A Charge-transfer Phenomenon between 2,3,5,6-Tetrafluoro-7,7,8,8-tetracyanop-quinodimethane (F4tcnq) and a Tetrathiafulvalene-based Self-assembled Monolayer Using an Indium-Tin Oxide Electrode," *Bulletin of the Korean Chemical Society*, vol. 31, pp. 1415–1418, May 2010.

[124] B. Lüssem, M. L. Tietze, H. Kleemann, C. Hobach, J. W. Bartha, A. Zakhidov, and K. Leo, "Doped organic transistors operating in the inversion and depletion regime," *Nat Commun*, vol. 4, Nov. 2013.

[125] M. L. Tietze, L. Burtone, M. Riede, B. Lüssem, and K. Leo, "Fermi level shift and doping efficiency in p-doped small molecule organic semiconductors: A photoelectron spectroscopy and theoretical study," *Phys. Rev. B*, vol. 86, p. 035320, July 2012.

[126] S. Guo, S. K. Mohapatra, A. Romanov, T. V. Timofeeva, K. I. Hardcastle, K. Yesudas, C. Risko, J.-L. Bredas, S. R. Marder, and S. Barlow, "n-Doping of Organic Electronic Materials Using Air-Stable Organometallics: A Mechanistic Study of Reduction by Dimeric Sandwich Compounds," *Chem. Eur. J.*, vol. 18, pp. 14760–14772, Nov. 2012.

[127] S. Guo, S. B. Kim, S. K. Mohapatra, Y. Qi, T. Sajoto, A. Kahn, S. R. Marder, and S. Barlow, "n-Doping of Organic Electronic Materials using Air-Stable Organometallics," *Advanced Materials*, vol. 24, pp. 699–703, Feb. 2012.

[128] S. A. Paniagua, J. Baltazar, H. Sojoudi, S. K. Mohapatra, S. Zhang, C. L. Henderson, S. Graham, S. Barlow, and S. R. Marder, "Production of heavily n- and p-doped CVD graphene with solution-processed redox-active metalorganic species," *Mater. Horiz.*, vol. 1, pp. 111–115, Nov. 2013.

[129] Y. Qi, S. K. Mohapatra, S. B. Kim, S. Barlow, S. R. Marder, and A. Kahn, "Solution doping of organic semiconductors using air-stable n-dopants," *Applied Physics Letters*, vol. 100, p. 083305, Feb. 2012.

[130] S. Olthof, S. Mehraeen, S. K. Mohapatra, S. Barlow, V. Coropceanu, J.-L. Bredas, S. R. Marder, and A. Kahn, "Ultralow Doping in Organic Semiconductors: Evidence of Trap Filling," *Phys. Rev. Lett.*, vol. 109, p. 176601, Oct. 2012.

[131] P. S. Szalay, J. R. Galan-Mascaros, R. Clerac, and K. R. Dunbar, "HAT(CN)6: a new building block for molecule-based magnetic materials," *Synthetic Metals*, vol. 122, pp. 535–542, Aug. 2001.

[132] S. Nannarone, F. Borgatti, A. DeLuisa, B. P. Doyle, G. C. Gazzadi, A. Giglia,

P. Finetti, N. Mahne, L. Pasquali, M. Pedio, G. Selvaggi, G. Naletto, M. G. Pelizzo, and G. Tondello, "The BEAR Beamline at Elettra," in *AIP Conference Proceedings*, vol. 705, pp. 450–453, AIP Publishing, May 2004.

[133] L. Pasquali, A. D. Luisa, and S. Nannarone, "The UHV Experimental Chamber For Optical Measurements (Reflectivity and Absorption) and Angle Resolved Photoemission of the BEAR Beamline at ELETTRA," in *AIP Conference Proceedings*, vol. 705, pp. 1142–1145, AIP Publishing, May 2004.

[134] L. N. Serkovic Loli, H. Hamoudi, J. E. Gayone, M. L. Martiarena, E. A. Sanchez, O. Grizzi, L. Pasquali, S. Nannarone, B. P. Doyle, C. Dablemont, and V. A. Esaulov, "Growth of N,N-Bis(1-ethylpropyl)perylene-3,4,9,10-tetracarboxdiimide Films on Ag (111)," *J. Phys. Chem. C*, vol. 113, pp. 17866–17875, Oct. 2009.

[135] P. Hohenberg and W. Kohn, "Inhomogeneous electron gas," *Phys Rev*, vol. 136, pp. B864 – B871, 1964.

[136] K. W. Clark, X.-G. Zhang, I. V. Vlassiouk, G. He, R. M. Feenstra, and A.-P. Li, "Spatially Resolved Mapping of Electrical Conductivity across Individual Domain (Grain) Boundaries in Graphene," *ACS Nano*, vol. 7, pp. 7956–7966, Sept. 2013.

[137] K. Aidas, C. Angeli, K. L. Bak, V. Bakken, R. Bast, L. Boman, O. Christiansen, R. Cimiraglia, S. Coriani, and P. Dahle, "The Dalton quantum chemistry program system," *Wiley Interdisciplinary Reviews: Computational Molecular Science*, 2013.

[138] J. P. Perdew, K. Burke, and M. Ernzerhof, "Generalized Gradient Approximation Made Simple," *Phys. Rev. Lett.*, vol. 77, pp. 3865–3868, Oct. 1996.

[139] B. Hammer, L. B. Hansen, and J. K. Noerskov, "Improved adsorption energetics within density-functional theory using revised Perdew-Burke-Ernzerhof functionals," *Phys. Rev. B*, vol. 59, pp. 7413–7421, Mar. 1999.

[140] G. Kresse and J. Furthmüller, "Efficient iterative schemes for ab initio total-energy calculations using a plane-wave basis set," *Phys. Rev. B*, vol. 54, pp. 11169–11186, Oct. 1996.

[141] G. Kresse and J. Furthmüller, "Efficiency of ab-initio total energy calculations for metals and semiconductors using a plane-wave basis set," *Computational Materials Science*, vol. 6, pp. 15–50, July 1996.

[142] G. Kresse and J. Hafner, "Ab initio molecular dynamics for liquid metals," *Phys. Rev. B*, vol. 47, pp. 558–561, Jan. 1993.

[143] S. Grimme, "Semiempirical GGA-type density functional constructed with

a long-range dispersion correction," *Journal of Computational Chemistry*, vol. 27, no. 15, pp. 1787–1799, 2006.

[144] A. Kokalj, "Computer graphics and graphical user interfaces as tools in simulations of matter at the atomic scale," *Computational Materials Science*, vol. 28, pp. 155–168, Oct. 2003.

[145] N. Severin, P. Lange, I. M. Sokolov, and J. P. Rabe, "Reversible dewetting of a molecularly thin fluid water film in a soft graphene-mica slit pore," *Nano Lett.*, vol. 12, pp. 774–779, Feb. 2012.

[146] O. Ochedowski, B. K. Bussmann, and M. Schleberger, "Graphene on Mica - Intercalated Water Trapped for Life," *Sci. Rep.*, vol. 4, Aug. 2014.

[147] A. Pirkle, J. Chan, A. Venugopal, D. Hinojos, C. W. Magnuson, S. McDonnell, L. Colombo, E. M. Vogel, R. S. Ruoff, and R. M. Wallace, "The effect of chemical residues on the physical and electrical properties of chemical vapor deposited graphene transferred to SiO2," *Applied Physics Letters*, vol. 99, no. 12, p. 122108, 2011.

[148] N. A. Vinogradov, K. A. Simonov, A. V. Generalov, A. S. Vinogradov, D. V. Vyalikh, C. Laubschat, N. Mrtensson, and A. B. Preobrajenski, "Controllable p-doping of graphene on Ir(111) by chlorination with FeCl3," *J. Phys.: Condens. Matter*, vol. 24, p. 314202, Aug. 2012.

[149] Y.-C. Lin, C.-C. Lu, C.-H. Yeh, C. Jin, K. Suenaga, and P.-W. Chiu, "Graphene Annealing: How Clean Can It Be?," *Nano Lett.*, vol. 12, pp. 414–419, Jan. 2012.

[150] J.-H. Chen, M. Ishigami, C. Jang, D. R. Hines, M. S. Fuhrer, and E. D. Williams, "Printed Graphene Circuits," *Advanced Materials*, vol. 19, no. 21, pp. 3623–3627, 2007.

[151] D. B. Farmer, R. Golizadeh-Mojarad, V. Perebeinos, Y.-M. Lin, G. S. Tulevski, J. C. Tsang, and P. Avouris, "Chemical Doping and ElectronHole Conduction Asymmetry in Graphene Devices," *Nano Lett.*, vol. 9, pp. 388–392, Jan. 2009.

[152] S. Doniach and M. Sunjic, "Many-electron singularity in X-ray photoemission and X-ray line spectra from metals," *J. Phys. C: Solid State Phys.*, vol. 3, p. 285, Feb. 1970.

[153] V. P. Zakaznova-Herzog, H. W. Nesbitt, G. M. Bancroft, J. S. Tse, X. Gao, and W. Skinner, "High-resolution valence-band XPS spectra of the nonconductors quartz and olivine," *Phys. Rev. B*, vol. 72, p. 205113, Nov. 2005.

[154] G. Beamson, D. T. Clark, and D. S.-L. Law, "Electrical conductivity dur-

ing XPS of heated PMMA: detection of core line and valence band tacticity effects," *Surface and Interface Analysis*, vol. 27, no. 2, pp. 76–86, 1999.

[155] S. Yamamoto, H. Bluhm, K. Andersson, G. Ketteler, H. Ogasawara, M. Salmeron, and A. Nilsson, "In situ x-ray photoelectron spectroscopy studies of water on metals and oxides at ambient conditions," *J. Phys.: Condens. Matter*, vol. 20, p. 184025, May 2008.

[156] Z. Luo, J. Shang, S. Lim, D. Li, Q. Xiong, Z. Shen, J. Lin, and T. Yu, "Modulating the electronic structures of graphene by controllable hydrogenation," *Applied Physics Letters*, vol. 97, no. 23, p. 233111, 2010.

[157] G. Giovannetti, P. Khomyakov, G. Brocks, V. Karpan, J. van den Brink, and P. Kelly, "Doping Graphene with Metal Contacts," *Physical Review Letters*, vol. 101, July 2008.

[158] K. K. Okudaira, S. Hasegawa, P. T. Sprunger, E. Morikawa, V. Saile, K. Seki, Y. Harada, and N. Ueno, "Photoemission study of pristine and photodegraded poly(methyl methacrylate)," *Journal of Applied Physics*, vol. 83, pp. 4292–4298, Apr. 1998.

[159] P. Frank, T. Djuric, M. Koini, I. Salzmann, R. Rieger, K. Mullen, R. Resel, N. Koch, and A. Winkler, "Layer Growth, Thermal Stability, and Desorption Behavior of Hexaaza-triphenylene-hexacarbonitrile on Ag(111)," *J. Phys. Chem. C*, vol. 114, pp. 6650–6657, Apr. 2010.

[160] S. Duhm, G. Heimel, I. Salzmann, H. Glowatzki, R. L. Johnson, A. Vollmer, J. P. Rabe, and N. Koch, "Orientation-dependent ionization energies and interface dipoles in ordered molecular assemblies," *Nat Mater*, vol. 7, pp. 326–332, Apr. 2008.

[161] L. Chen, L. Wang, Z. Shuai, and D. Beljonne, "Energy Level Alignment and Charge Carrier Mobility in Noncovalently Functionalized Graphene," *J. Phys. Chem. Lett.*, vol. 4, pp. 2158–2165, July 2013.

[162] A. J. Marsden, M.-C. Asensio, J. Avila, P. Dudin, A. Barinov, P. Moras, P. M. Sheverdyaeva, T. W. White, I. Maskery, G. Costantini, N. R. Wilson, and G. R. Bell, "Is graphene on copper doped?," *physica status solidi (RRL) Rapid Research Letters*, vol. 7, no. 9, pp. 643–646, 2013.

[163] H. M. S. B. Bröker, *Electronic and structural properties of interfaces between electron donor & acceptor molecules and conductive electrodes*. PhD thesis, Humboldt Universitt Berlin, 2010.

[164] X. Liu, A. Grüneis, D. Haberer, A. V. Fedorov, O. Vilkov, W. Strupinski, and T. Pichler, "Tunable Interface Properties between Pentacene and Graphene

on the SiC Substrate," *The Journal of Physical Chemistry C*, vol. 117, pp. 3969–3975, Feb. 2013.

[165] P. Amsalem, J. Niederhausen, A. Wilke, G. Heimel, R. Schlesinger, S. Winkler, A. Vollmer, J. P. Rabe, and N. Koch, "Role of charge transfer, dipole-dipole interactions, and electrostatics in Fermi-level pinning at a molecular heterojunction on a metal surface," *Phys. Rev. B*, vol. 87, p. 035440, Jan. 2013.

[166] H. Wang, P. Amsalem, G. Heimel, I. Salzmann, N. Koch, and M. Oehzelt, "Band-Bending in Organic Semiconductors: the Role of Alkali-Halide Interlayers," *Advanced Materials*, pp. n/a–n/a, 2013.

[167] Y. H. Kim, J. Lee, S. Hofmann, M. C. Gather, L. Müller-Meskamp, and K. Leo, "Achieving High Efficiency and Improved Stability in ITO-Free Transparent Organic Light-Emitting Diodes with Conductive Polymer Electrodes," *Advanced Functional Materials*, pp. n/a–n/a, 2013.

[168] S. Schubert, J. Meiss, L. Müller-Meskamp, and K. Leo, "Improvement of Transparent Metal Top Electrodes for Organic Solar Cells by Introducing a High Surface Energy Seed Layer," *Advanced Energy Materials*, vol. 3, no. 4, pp. 438–443, 2013.

[169] J. Meyer, P. R. Kidambi, B. C. Bayer, C. Weijtens, A. Kuhn, A. Centeno, A. Pesquera, A. Zurutuza, J. Robertson, and S. Hofmann, "Metal Oxide Induced Charge Transfer Doping and Band Alignment of Graphene Electrodes for Efficient Organic Light Emitting Diodes," *Sci. Rep.*, vol. 4, June 2014.

[170] I. Gierz, C. Riedl, U. Starke, C. R. Ast, and K. Kern, "Atomic Hole Doping of Graphene," *Nano Letters*, vol. 8, pp. 4603–4607, Dec. 2008.

[171] Z. Chen, I. Santoso, R. Wang, L. F. Xie, H. Y. Mao, H. Huang, Y. Z. Wang, X. Y. Gao, Z. K. Chen, D. Ma, A. T. S. Wee, and W. Chen, "Surface transfer hole doping of epitaxial graphene using MoO[sub 3] thin film," *Applied Physics Letters*, vol. 96, no. 21, p. 213104, 2010.

[172] G. Heimel, S. Duhm, I. Salzmann, A. Gerlach, A. Strozecka, J. Niederhausen, C. Bürker, T. Hosokai, I. Fernandez-Torrente, G. Schulze, S. Winkler, A. Wilke, R. Schlesinger, J. Frisch, B. Bröker, A. Vollmer, B. Detlefs, J. Pflaum, S. Kera, K. J. Franke, N. Ueno, J. I. Pascual, F. Schreiber, and N. Koch, "Charged and metallic molecular monolayers through surface-induced aromatic stabilization," *Nat Chem*, vol. 5, pp. 187–194, Mar. 2013.

[173] C. Coletti, C. Riedl, D. S. Lee, B. Krauss, L. Patthey, K. von Klitzing, J. H. Smet, and U. Starke, "Charge neutrality and band-gap tuning of epitaxial

graphene on SiC by molecular doping," *Phys. Rev. B*, vol. 81, p. 235401, June 2010.

[174] D. Maccariello, M. Garnica, M. A. Nio, C. Navo, P. Perna, S. Barja, A. L. Vzquez de Parga, and R. Miranda, "Spatially Resolved, Site-Dependent Charge Transfer and Induced Magnetic Moment in TCNQ Adsorbed on Graphene," *Chem. Mater.*, vol. 26, pp. 2883–2890, May 2014.

[175] L. Romaner, G. Heimel, J.-L. Bredas, A. Gerlach, F. Schreiber, R. L. Johnson, J. Zegenhagen, S. Duhm, N. Koch, and E. Zojer, "Impact of Bidirectional Charge Transfer and Molecular Distortions on the Electronic Structure of a Metal-Organic Interface," *Phys. Rev. Lett.*, vol. 99, p. 256801, Dec. 2007.

[176] T.-C. Tseng, C. Urban, Y. Wang, R. Otero, S. L. Tait, M. Alcam, D. cija, M. Trelka, J. M. Gallego, N. Lin, M. Konuma, U. Starke, A. Nefedov, A. Langner, C. Wll, M. n. Herranz, F. Martn, N. Martn, K. Kern, and R. Miranda, "Charge-transfer-induced structural rearrangements at both sides of organic/metal interfaces," *Nature Chemistry*, vol. 2, pp. 374–379, May 2010.

[177] C. Gong, G. Lee, B. Shan, E. M. Vogel, R. M. Wallace, and K. Cho, "First-principles study of metal/graphene interfaces," *Journal of Applied Physics*, vol. 108, no. 12, p. 123711, 2010.

[178] E. G. Perevalova, I. F. Urazowski, D. A. Lemenovskii, Y. L. Slovokhotov, and Y. T. Struchkov, "Synthesis and structure of dimeric metallocene derivatives of transition metals of groups IV and V. Crystal and molecular structures of (5:5-C10h8)(C5h5)2nb2(-H)(-OEt) and (5:5-C10h8)(C5h5)2ti2(-H)(-Cl)," *Journal of Organometallic Chemistry*, vol. 289, pp. 319–329, July 1985.

[179] W. Jaegermann and O. Henrion, "Surface redox reactions of cobaltocene adsorbed onto pyrolytic graphite (HOPG)," *Surface Science*, vol. 387, pp. 1073–1078, Oct. 1997.

[180] L. A. Torres-Gomez, G. Barreiro-Rodrguez, and F. Mendez-Ruiz, "Vapour pressures and enthalpies of sublimation of ferrocene, cobaltocene and nickelocene," *Thermochimica Acta*, vol. 124, pp. 179–183, Feb. 1988.

[181] S. K. Mohapatra, A. Fonari, C. Risko, K. Yesudas, K. Moudgil, J. H. Delcamp, T. V. Timofeeva, J.-L. Brdas, S. R. Marder, and S. Barlow, "Dimers of Nineteen-Electron Sandwich Compounds: Crystal and Electronic Structures, and Comparison of Reducing Strengths," *Chemistry - A European Journal*, vol. 20, pp. 15385–15394, Nov. 2014.

Publications

This list provides the publications that I have contributed during this work.

1. **C. Christodoulou**, A. Giannakopoulos, M. V. Nardi, G. Ligorio, M. Oehzelt, L. Chen, L. Pasquali, M. Timpel, A. Giglia, S. Nannarone, P. Norman, M. Linares, K. Parvez, K. Müllen, D. Beljonne, and N. Koch. Tuning the Work function of Graphene-on-Quartz with a High Weight Molecular Acceptor. *The Journal of Physical Chemistry C*, 118(9):4784-4790, 2014.

2. **C. Christodoulou**, A. Giannakopoulos, G. Ligorio, M. Oehzelt, M. Timpel, J. Niederhausen, A. Giglia, S. Nannarone, L. Pasquali, K. Parvez, K. Müllen, D. Beljonne, N. Koch, and M. V. Nardi. Tuning the electronic structure of graphene by molecular dopants: Impact of the substrate. *ACS Advanced Material Interfaces*, 7, 19134-19144, 2015.

3. Y. Ito, **C. Christodoulou**, M. V. Nardi, N. Koch, H. Sachdev and K. Müllen. Chemical Vapor Deposition of N-Doped Graphene and Carbon Films: The Role of Precursors and Gas Phase. *ACS Nano*, 8(4):3337-3346, 2014.

4. Y. Ito, **C. Christodoulou**, M. V. Nardi, N. Koch, H. Sachdev and K. Müllen. Carbon Formation From a New Transition Metal Dehalogenation Reaction: Synthesis, Characterisation and Magnetic Properties. *Journal of the American Chemical Society*, 137(24), 76787685, 2015.

5. Z. Y. Xia, G. Giambastiani, **C. Christodoulou**, M. V. Nardi, N. Koch, E. Treossi, V. Bellani, S. Pezzini, F. Corticelli, V. Morandi, A. Zanelli and V. Palermo. Synergic Exfoliation of Graphene with Organic

Molecules and Inorganic Ions for the Electrochemical Production of Flexible Electrodes. *ChemPlusChem*, 79(3):443-446, 2014.

6. G. Ligorio, M. V. Nardi, **C. Christodoulou**, I. Florea, N. C. Monteiro, O. Ersen, M. Brinkmann, and N. Koch. Charging and exciton-mediated descharging of metal nanoparticles in organic semiconductor matrices. *APL*, 104(16):163302, 2014.

7. G. Ligorio, M. V. Nardi, **C. Christodoulou** and N. Koch. Organic Semiconductor/Gold Interface Interactions: From Physisorption on Planar Surfaces to Chemical Reactions with Metal Nanoparticles. *ChemPhysChem*, 16(12):2602-2608, 2015.

8. R. Schlesinger, F. Bianchi, S. Blumstengel, **C. Christodoulou**, R. Ovsyannikov, B. Kobin, K. Moudgil, S. Barlow, S. Hecht, S. Marder, F. Henneberger, and N. Koch. Efficient light emission from inorganic/organic semiconductor hybrid structures by energy level tuning.
Nature Communications 6, 6754, 2015.

9. I. Salzmann, A. Moser, M. Oehzelt, T. Breuer, X. Feng, Z.Y. Juang, D. Nabok, R. G. D. Valle, S. Duhm, G. Heimel, A. Brillante, E. Venuti, I. Billoti, **C. Christodoulou**, J. Frisch, P. Puschnig, C. Draxl, G. Witte, K. Müllen, and N. Koch. Epitaxial growth of π-stacked perfluoropentacene on graphene-coated quartz. *ACS Nano*, 6(12):10874-10883, 2012

10. M. Timpel, M. V. Nardi, S. Krause, G. Ligorio, **C. Christodoulou**, L. Pasquali, A. Giglia, J. Frisch, B. Wegner, P. Moras, and N. Koch. Surface Modification of ZnO(0001)-Zn with Phosphonate-Based Self-Assembled Monolayers: Binding Modes, Orientation, and Work Function. *Chemistry of Materials*, 26(17):5042-5050, 2014.

11. R. Trattnig, L. Pevzner, M. Jäger, R. Schlesinger, M. V. Nardi, G. Ligorio, **C. Christodoulou**, N. Koch, M. Baumgarten, K. Müllen, and E. J. W. List-Kratochvil. Bright Blue Solution Processed Triple-Layer Polymer Light-Emitting Diodes Realized by Thermal Layer Stabilization and Orthogonal Solvents. *Advanced Functional Materials*, 23(39):4897-4905, 2013.

12. S. Nau, R. Trattnig, L. Pevzner, M. Jäger, R. Schlesinger, M. V. Nardi. G. Ligorio, **C. Christodoulou**, N. Schulte, S. Winkler, J. Frisch, A. Vollmer, M. Baumgarten, S. Sax, N. Koch, K. Müllen, E. J. W. List-Kratochvil. All solution processed blue multi-layer light emitting diodes realized by thermal layer stabilization and orthogonal solvent processing. *In SPIE Organic Photonics+Electronics*, International Society for Optics and Photonics, 2013.

A Appendix

NEXAFS normalisation and calibration procedure

For the NEXAFS data acquisition, the incident photon flux has an energy dependence due to non-uniform absorption and beamline optics (monochromator, grating, mirror, filters). This means that the incident photon flux on the sample, $I_{sample}(h\nu)$ should be divided by the incident flux in order to clear the effects from the optics.

A gold mesh can be used to measure the incident flux, since gold has no absorption edges in the C, N K-edge regions. In a measurement, the sample data together with the incident flux on the mesh ($I_{mesh}(h\nu)$) are measured simultaneously and the following division is performed:

$$R(h\nu) = \frac{I_{sample}(h\nu)}{I_{mesh}(h\nu)}$$ (A.1)

A complication is introduced if the mesh is contaminated by carbon or nitrogen residues. As the mesh is hard to be removed from the experimental chamber,an additional clean gold sample is used simultaneously with the mesh.
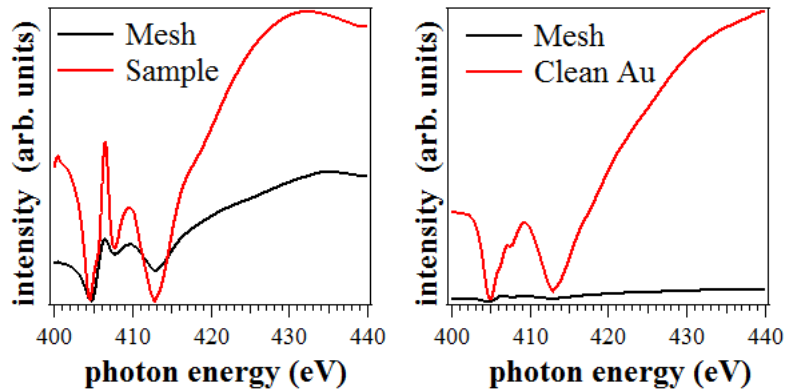

Figure A.1: Sample and clean Au data, together with their corresponding mesh data.

To clear of the effect of any residual carbon/nitrogen, the following

division has to be performed:

$$R'(h\nu) = \frac{\dfrac{I_{sample}(h\nu, t)}{I_{mesh}(h\nu, t)}}{\dfrac{I_{Au}(h\nu, t')}{I_{mesh}(h\nu, t')}} \qquad (A.2)$$

The eq. (A.2) contains t and t' as a parameter, since the two measurements were performed at different times, with probably different photon flux. But, as it is shown, after the division, this cancels out.

Before data normalisation, calibration of the photon energy has to be performed since the measurements were conducted at different times t and t'. This is done by selecting a prominent feature in the mesh data of the sample and the clean Au and align the spectra to that feature, as shown in Fig. A.2.
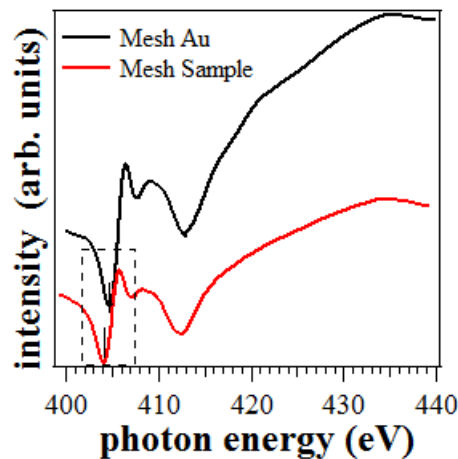

Figure A.2: Prominent feature (valley) in the mesh spectra of the Au and the sample, which can be used to calibrate the photon energy for the two data sets, before data normalisation.

XPS spectra of bulk F_6TCNNQ on SiO_2

The molecular acceptor F_6TCNNQ is a rather novel molecular acceptor not studied intensively using XPS spectroscopy. To check the stability of the molecule under X-ray irradiation and after sublimation of the molecule in UHV, a bulk molecular film (90 nm) of F_6TCNNQ was deposited on

SiO$_x$. The C 1s, N 1s and F 1s core level spectra are measured and fitted to identify the underlying emissions.
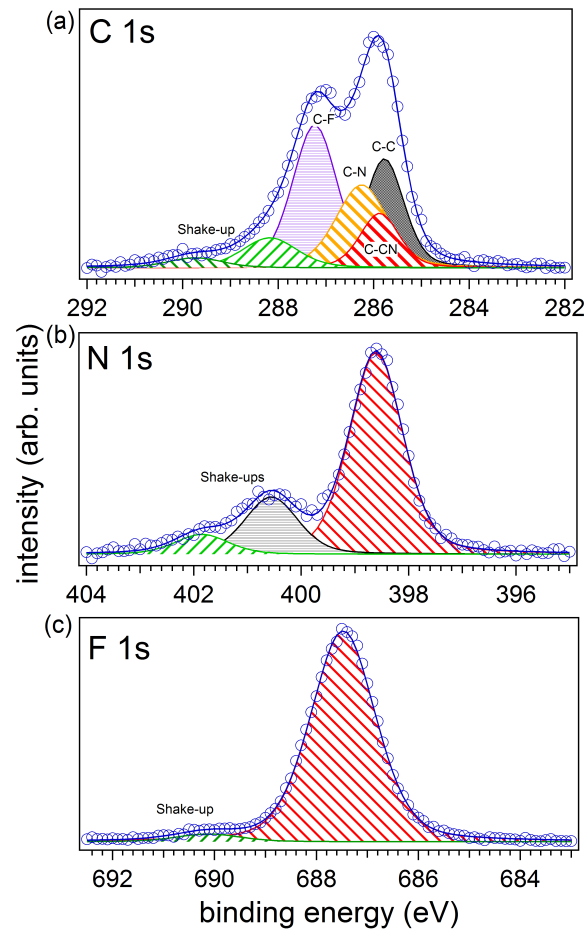

Figure A.3: a) C 1s b) N 1s and c) F 1s core level spectra of bulk F$_6$TCNNQ deposited on SiO$_2$.

Acknowledgements

I would like to thank Prof. Norbert Koch for giving me the great opportunity to join his group and start this experience and for funding me through the 7th Marie Curie ITN GENIUS program. Each interaction we had gave me an important lesson to think about.

I thank Prof. Jürgen P. Rabe for providing access to his experimental setups and being there for fruitful discussions and always a good word.

Dr. Marco V. Nardi provided useful guidance and masterfully taught me the experimental techniques at the synchrotron facilities that I have used throughout this work.

Many thanks to the collaborators that performed the simulations in this work, Dr. David Beljonne and Angelos Giannakopoulos and also Prof. Luca Pasquali.

At the BEAR endstation, Angelo Giglia and Prof. Luca Pasquali as well as Dr. Anje Vollmer, Dr. Ruslan Ovsyannikov, Dr. Mihaella Gorgoi at BESSY II provided constant support and advice during the beamtimes.

Special thanks to Prof. Klaus Müllen and Dr. Khaled Parvez for providing the graphene samples.

The secretary of our group, Mrs Henriette Strahl, helped me constantly with the bureaucratic issues and helped me keep them under control.

Jens Niederhausen was always there for fruitful and productive discussions, with a cup of coffee or a bottle of beer.

Giovanni Ligorio, one of my office mates and my conference mate, supported me throughout my thesis.

Dr. Johannes Frisch introduced me to the vacuum apparatus and provided support since I have started.

I want to give special thanks to Jens Niederhausen, Dr. Melanie Timpel, Dr. Henry Mendez, Dr. Kouki Akaike and Dr. Marco V. Nardi for proofreading this thesis.

Dr. Philip Lange, Dr. Nicolai Severin and Dr. Vitalij Scenev introduced

me to Atomic force microscopy and Raman Spectroscopy.

Dr. Hendrik Glowatzki and Jens Niederhausen supported me with scanning tunnelling microscopy measurements.

I want to thank Dr. Martin Oehzelt, Dr. Georg Heimel and Dr. Ingo Salzmann for fruitful discussions, help with the interpretation of data as well as help with the publication process.

I want to thank all my colleagues in the SMS group and all the people in the GENIUS project.

Finally, I want to thank my girlfriend Nefeli Ioannou for providing me continuous support.